Rashba-Type Spin-Orbit Coupling in the Surface Alloys on Ag(111) Probed by Spin- and Angle-Resolved Photoemission Spectroscopy

---

Dissertation

zur

Erlangung der naturwissenschaftlichen Doktorwürde
(Dr. sc. nat.)

vorgelegt der

Mathematisch-naturwissenschaftlichen Fakultät

der

Universität Zürich

von

Fabian Meier
von Zürich

Promotionskomitee

Prof. Dr. Jürg Osterwalder (Vorsitz und Leitung der Dissertation)
Dr. Jan Hugo Dil
Dr. Gustav Bihlmayer (Gutachter)

Zürich 2011

Abstract

In this thesis, the surface alloys formed by Bi, Pb and Sb on Ag(111), whose surface states show a Rashba-type spin splitting of an unprecedented size, are investigated. All systems feature a similar surface state band structure, consisting of two Kramers pairs, with distinct differences in the size of the spin splitting and the position of the Fermi level. The $(\sqrt{3} \times \sqrt{3})R30^\circ$ structure of these materials, which can be regarded as the origin of the size of the Rashba effect, was analyzed employing quantitative low-energy electron diffraction and reveals a large outward relaxation of the alloy atoms. The spin structure of the surface states was studied using spin- and angle-resolved photoemission spectroscopy employing a novel type of data analysis routine, which allows to access the spin polarization vectors of the individual bands: the two-step fitting routine. In this routine, first the measured intensities are fitted with an appropriate number of suitable peaks to quantify the contributions of the individual bands; then, the measured spin polarization curves are fitted by varying the polarization direction and its magnitude for each band. Using this approach it is found that the surface state bands are fully spin polarized, and that for some states, the spin polarization vectors rotate out of the surface plane. It is argued that this out-of-plane spin polarization component is a consequence of an in-plane structural inversion asymmetry.

The Rashba-type spin splitting is discussed in terms of an asymmetric surface state wave function, and it is shown that the enhancement of the size of the spin splitting is an interplay between the in-plane structural inversion asymmetry, the surface corrugation and the atomic spin-orbit coupling. The latter two differ for the different alloy atoms, and it is demonstrated that the mixture of the different alloy atoms enables a full and continuous tunability of both the size of the Rashba effect and the position of the Fermi level, yielding a fully tunable Rashba system. Moreover, it is shown that for appropriate mixing rations, the Fermi surface undergoes a topological transition with impact on both the Fermi surface spin textures and the transport of spin.

At last, it is argued that when the size of the spin splitting becomes comparable to the intrinsic momentum broadening of the quasiparticles, the spin polarization of the photoelectron has to be described by the coherent superposition of the overlapping quasiparticles, resulting in a large spin polarization component in the plane perpendicular to the quantization axis defined by the Rashba effect.

Zusammenfassung

Das Hauptthema dieser Dissertation sind die Oberflächenlegierungen Bi, Pb und Sb auf Ag(111). Das Besondere an diesen Oberflächenlegierungen ist, dass ihre Oberflächenzustände einen Rashba Effekt von bisher unerreichter Grösse zeigen. Die Bandstruktur dieser elektonischen Zustände besteht für alle diese Systeme aus zwei Kramerspaaren, die sich abhängig von der Legierung in der Grösse der Rashba Aufspaltung und der Position der Fermienergie unterscheiden. Die Struktur der Oberfläche, welche als Ursache für die Grösse des Rashbaeffektes angesehen werden kann, wurde mittels quantitativer niederenergetischer Elektronenbeugung untersucht. Sie weist eine $(\sqrt{3} \times \sqrt{3})R30°$ Rekonstruktion auf, in welcher die Legierungsatome stark aus der Oberfläche herausragen. Die Band- und Spinstruktur dieser Systeme wurde mit spin- und winkelaufgelöster Photoemissionsspektroskopie gemessen und mittels einer neuen Auswertungsroutine, der sog. 2-Stufen-Fit Routine, analysiert. Darin werden zuerst die spinintegrierten Intensitätsdaten mit der entsprechenden Anzahl an Bändern gefittet, um deren Beitrag zum gemessenen Spektrum zu quantifizieren. Danach werden durch Variation der Länge und Richtung der individuellen Spinpolarisationsvektoren die gemessenen Spinpolarisationen gefitted. Durch Benützen von diesem Ansatz wurde festgestellt, dass alle Bänder der Oberflächenzustände vollständig spinpolarisiert sind und dass die Spinpolarisation von bestimmten Zuständen eine Komponente entlang der Oberflächennormalen aufweist. Es wird argumentiert, dass diese Komponente eine Konsequenz der Inversions Asymmetrie in der Oberfläche ist.

Die Rashba-ähnliche Spinaufspaltung der Bänder wird im Zusammenhang einer Asymmetrie in der Wellenfunktion der Oberflächenzustände diskutiert und es wird gezeigt, dass die Grösse der Aufspaltung durch ein Zusammenspiel von drei Faktoren bestimmt wird: die strukturelle Inversionsasymmetrie in der Oberfläche, die Distanz der Legierungsatome zu den Ag Atomen der Oberfläche und die atomare Spin-Bahn-Kopplung. Die letzteren Zwei unterscheiden sich für die verschiedenen Legierungsatome und es wird gezeigt, dass durch Mischen der verschiedenen Legierungsatome eine vollständige Kontrolle sowohl der Grösse der Spinaufspaltung als auch der Position des Ferminiveaus erreicht werden kann. Zusätzlich wird gezeigt, dass für spezielle Mischungsverhältnisse der Legierungsatome die Topologie des Fermisees geändert wird, was sowohl die Spinstruktur der Fermifläche ändert als auch den Spintransport stark beeinflusst.

Zum Schluss wird diskutiert, dass die Photoelektronen durch eine kohärente Superposition der überlappenden Quasiteilchen beschrieben werden müssen, wenn die Grösse der Spinaufspaltung vergleichbar wird mit der Impulsverbreiterung der Bänder. Dies führt zu einer starken Spinpolarisationskomponente senkrecht zur Rashbaquantisierungsachse.

List of acronyms

1D/2D	one-/two-dimensional
2DEG	two-dimensional electron gas
ARPES	angle-resolved photoelectron spectroscopy
BIA	bulk inversion asymmetry
COPHEE	(the) complete photoemission experiment
DFT	density functional theory
DOS	density of states
EDC	energy distribution curve
fcc	face centered cubic (lattice)
hcp	hexagonal close-packed (lattice)
LEED	low-energy electron diffraction
MCD	magnetic circular dichroism
MDC	momentum distribution curve
ML	monolayer
QWS	quantum well state
SARPES	spin- and angle-resolved photoelectron spectroscopy
SBZ	surface Brillouin zone
SIA	structure inversion asymmetry
SIS	surface and interface spectroscopy
SOC	spin-orbit coupling
SPLEED	spin-polarized low energy electron diffraction
STM	scanning tunneling microscopy/microscope
SXRD	surface x-ray diffraction
TRIM	time reversal invariant momentum
UV	ultraviolet (radiation)
VLEED	very low energy electron diffraction

Contents

1 Introduction

In the prospect of a new information processing technology called spintronics, [1,2] which relies on the spin degrees of freedom of the electron rather than its charge, ways to manipulate and measure the spin of the electron have received growing attention in the past few years. The goal of spintronics is to understand the interaction between the electron spin and its solid-state environments and to use this information to make useful devices. Of special interest are mechanisms which allow to control the spin of the electron without the employment of external magnetic fields. In this context, time reversal invariant systems with broken translational symmetry, where the so-called Rashba effect [3] lifts the spin degeneracy, are of particular importance.

The surface naturally breaks the translational symmetry and allows for the existence of electronic states confined to the near surface region. [4, 5] In the absence of spin-orbit coupling (SOC), these so-called surface states are, for non-magnetic systems, spin-degenerate, as schematically depicted in Fig. 1 (a). For finite SOC however, the surface states in general become spin split, as exemplified in Fig. 1 (b). The size of this spin splitting depends on several factors as shown in sections 4 and 6 of this thesis. Due to their confinement to the surface region, the surface states are ideal candidates for the study of effects related to SOC in a structurally asymmetric environment, and allow for a direct measurement of their band and spin structure by means of spin- and angle-resolved photoemission spectroscopy.

First systematic studies of surface states employing spin-integrated ARPES were per-

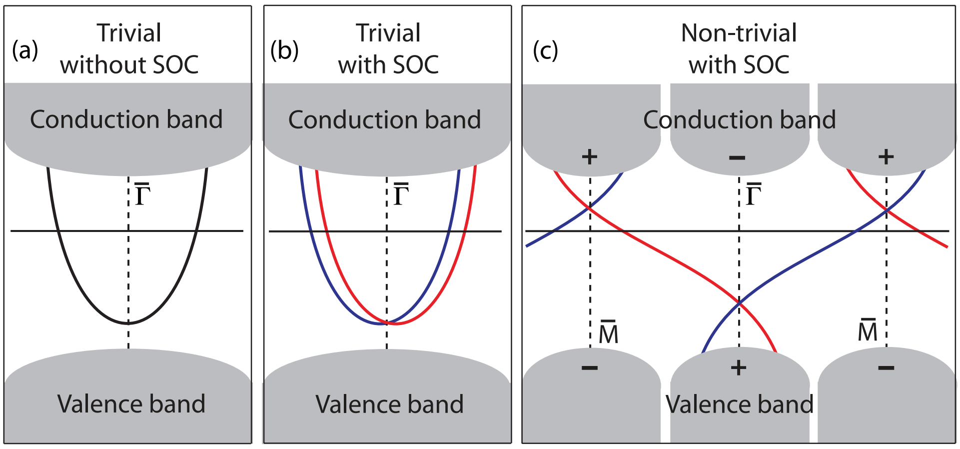

Figure 1: Schematic picture of (a) a spin-degenerate surface state, (b) a Rashba-type spin-split surface state and (c) a topologically non-trivial surface state. Red and blue indicate opposite spin polarization.

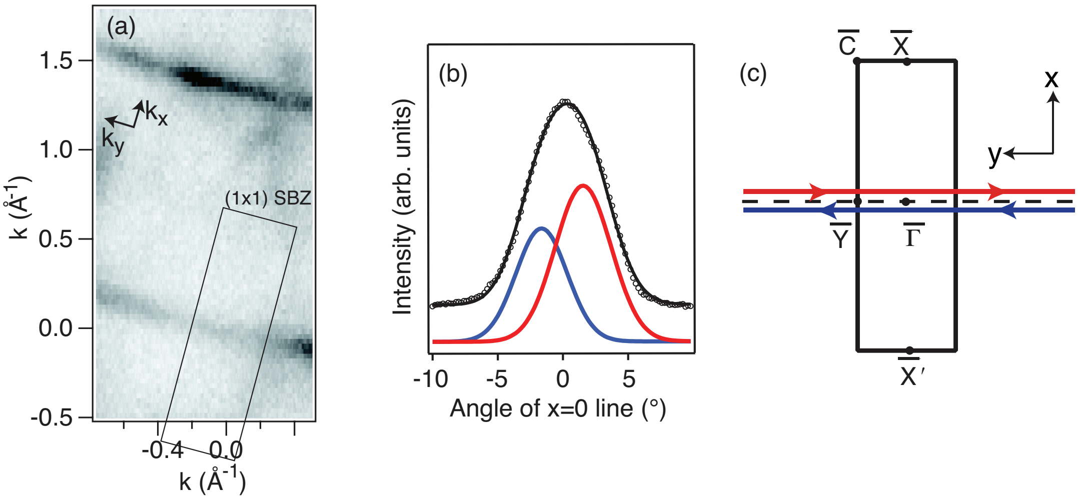

Figure 2: (a) Spin-integrated photoemission intensity of a Bi(114) surface at the Fermi energy, revealing the existence of a quasi-one-dimensional Fermi line, passing through the origin. Also indicated is the surface Brillouin zone for the truncated bulk surface. (b) Black open markers: spin-integrated photoemission intensity for an azimuthal angle scan through the surface Fermi line. Two Gaussian components (red and blue) are fitted to the data to represent the two spin-split components. (c) Schematic Fermi contour of Bi(114) resulting from spin- and angle-resolved photoemission spectroscopy measurements. (from Ref. [15])

formed on the (111) surfaces of Cu, Ag and Au, where the most remarkable feature was the observation of two Rashba-type spin-split parabolas in Au(111). [6, 7] The first direct observation of the spin-polarized nature of such Rashba-type spin-split bands using SARPES was obtained from the surface state of W(110). [8] Later on, the full spin structure of the Fermi surface of the Au(111) surface state could be mapped by using a three-dimensional spin polarimeter. [9] Much larger SOC induced spin splittings and more complicated Fermi surfaces were observed on the different surfaces of the semimetal Bi. [10–14] The most remarkable finding was obtained from Bi(114). [15] In this system, the surface state Fermi surface consists of two quasi-one-dimensional, fully spin-polarized bands, as shown in Fig. 2. The spin structure of the surface states is such that all electrons traveling to one side have spin up, while all electrons traveling to the other side have spin down. Therefore, the surface can be regarded as a one-dimensional topological metal. However, the momentum splitting at the Fermi level is too small to be resolved with spin-integrated ARPES and indicates the importance of the extra spin information which SAPRES can provide.

Topological insulators are a new phase of matter, in which the properties of the bulk band structure result in the formation of topologically non-trivial surface states as schemati-

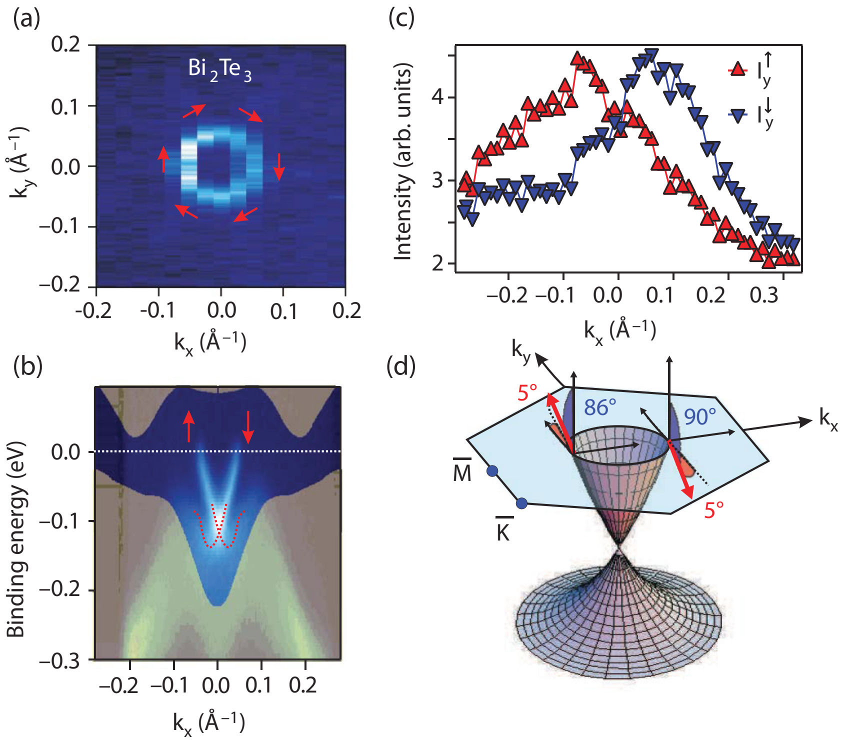

Figure 3: (a) ARPES intensity map at E_F of Bi$_2$Te$_3$(111). Red arrows denote the direction of spin projection around the Fermi surface. (b) ARPES dispersion of Bi$_2$Te$_3$ along k_x. The dotted lines are guides to the eye. The shaded regions in (b) are projections of the bulk bands onto the (111) surface. (c) Fitted values of the spin polarization vector $\boldsymbol{P}$. (d) Spin-resolved spectra obtained from the y component of the spin polarization data. (from Ref. [20])

cally depicted in Fig. 1 (c). [16–19] Topological insulators can also be regarded as bulk band insulators with a topologically protected metal as surface, and it is the spin structure of this topological metal which determines the interesting electronic properties. In spite of the broken translational symmetry perpendicular to the surface, the electronic surface states are forced to be degenerate for certain high-symmetry points, the so-called time reversal invariant momenta (TRIM), e.g. $\bar{\Gamma}$ and $\bar{M}$, as a consequence of time reversal symmetry and in-plane translational symmetry. In the absence of magnetic fields, this of course holds for an arbitrary surface state. However, in a topological insulator, the parity of the projected bulk bands is reversed between e.g. the $\bar{\Gamma}$ and the $\bar{M}$ point. Because the surface states connect bulk bands of the same parity and are forced to be degenerate at a TRIM, a cut between two TRIM is crossed by an odd number of fully spin-polarized surface states as shown in Fig. 1 (c).

Figs. 3 (a) and (b) show the experimental (spin-integrated) ARPES Fermi surface and dispersion of the (111) surface of the topological insulator Bi_2Te_3. The Fermi surface consists of a single circular contour and in that respect looks similar to the surface state Fermi surface of e.g. Cu(111). A first indication that the topology of Bi_2Te_3 is different from Cu can be obtained from Fig. 3 (b), where for $E_b > 0.1$ eV two pairs of bands can be seen and at E_F only one, indicating a scenario as depicted in Fig. 1 (c). However, only with the additional information of the spin polarization of the surface state bands, a direct and full determination of the topological parameters of the system is possible. [21] Therefore SARPES is an ideal technique for the study of topological insulators. Figs. 3 (c) shows the spin-resolved intensity data $I_y^{\uparrow}$ and $I_y^{\downarrow}$ for Bi_2Te_3 obtained from the spin polarization data P_y of a momentum distribution curve at $E_b = 20$ meV, which prove the topologically non-trivial structure.

While the surface state of Bi(114) has a unique spin quantization axis, Bi_2Te_3 has a momentum dependent spin quantization axis, as indicated by the red arrows in Fig. 1 (a). A dependency of the quantization axis on the momentum is typical for non-magnetic systems, in which the spin splitting is brought about by the spin-orbit interaction. In such a case, a sophisticated data analysis routine, such as the two-step fitting routine presented in chapter 2, is necessary in order to obtain precise information about the spin polarization vectors of the individual states. Fig. 3 (d) shows the spin polarization vectors obtained by applying the two-step fitting routine to the spin-resolved data. The spin polarization vectors are antiparallel, i.e. the states are spin polarized along the positive and negative y axis, which justifies the representation in terms of the spin-resolved intensities $I_y^{\uparrow}$ and $I_y^{\downarrow}$. However, for the surface alloys on Ag(111), the situation is more involved, and states can have different spin quantization axes within the same spectrum, which highlights the importance of the two-step fitting routine.

The surface alloys formed by Bi, Pb and Sb on Ag(111) are topologically trivial systems with Rashba-type spin-split surface states. Although the Ag(111) substrate short-circuits possible spin currents at the surface, these systems are perfect model systems for the study of the Rashba effect. The findings obtained from the study of the surface alloys on Ag(111), e.g. a giant Rashba-type spin splitting, an out-of-plane rotation of the spin polarization vector, a control of the size of the spin splitting and the chemical potential, can be applied to other systems. In fact, the discovery of the Rashba effect in the surface alloys on Ag(111) has lead to the study of the surface alloys on thin Ag films on Si(111) [22,23] and of the related surface alloys on Cu(111). [24] Moreover, it has lead to the discovery of a giant Rashba-type spin splitting on modified surfaces of Si(111). [25,26]

2 Spin- and angle-resolved photoemission spectroscopy

2.1 Angle-resolved photoemission spectroscopy

Angle-resolved photoemission spectroscopy (ARPES) has proven itself as a powerful tool for the investigation of the electronic structure of surfaces and near surface regions. [27] It is a photon-in electron-out process based on the photoelectric effect. [28] In a single electron picture, the photoemission process can be described by the interaction of the electromagnetic wave field $\boldsymbol{A}$ with an electron bound in the crystal potential. [29] The Hamiltonian of the system is then given by

$$H = H_0 + \frac{1}{2m}\left(-\frac{2e\hbar}{ic}\boldsymbol{A}\cdot\boldsymbol{\nabla} - \frac{e\hbar}{ic}\boldsymbol{\nabla}\cdot\boldsymbol{A} + \frac{e^2}{c^2}|\boldsymbol{A}|^2\right), \tag{1}$$

where $H_0 = -\hbar^2\Delta/2m + V$ is the Hamiltonian of the unperturbed part, with V the crystal potential. Both the second term $(e\hbar/ic)\boldsymbol{\nabla}\cdot\boldsymbol{A}$ and the third term $(e^2/c^2)|\boldsymbol{A}|^2$ in Eq. 1 are usually small and are therefore neglected in the following.

The transition probabilities ω_{fi} from the initial state i to the final state f are given by Fermi's Golden rule

$$\omega_{fi} \sim |\langle f\,|\boldsymbol{A}\cdot\boldsymbol{\nabla}|\,i\rangle|^2\,\delta(E_f - E_i - h\nu), \tag{2}$$

where $h\nu$ is the photon energy, E_f and E_i are the energy of the final and the initial state, respectively. The operator $\boldsymbol{\nabla}$ is related to the electron momentum through $\boldsymbol{p} = -i\hbar\boldsymbol{\nabla}$. As shown in section 6.5 for the surface alloys on Ag(111), the matrix element $t_{fi} = \langle f|\boldsymbol{A}\cdot\boldsymbol{\nabla}|i\rangle$ can show a significant dependency on the experimental parameters such as e.g. the photon energy.

In the photoemission experiment the energy, the momentum and the spin of the photoelectron can be measured depending on the capabilities of the experimental setup. Energy conservation yields the relation

$$E_b = h\nu - \Phi - E_{kin}, \tag{3}$$

where E_b, Φ and E_{kin} are the binding energy, work function and kinetic energy, respectively. Both the photon energy and the work function are known quantities and the kinetic energy is measured, which allows for the determination of the binding energy through Eq. 3. Neglecting the momentum of the photon, which is reasonable in the UV range, where $|\boldsymbol{k}_\gamma| \approx 0.01$ Å^{-1} for a photon of 20 eV, we have the momentum conservation $\boldsymbol{k}_f = \boldsymbol{k}_i + \boldsymbol{G}$, where $\boldsymbol{G}$ is a reciprocal lattice vector. The momentum $\boldsymbol{k}$ is usually defined relative to the sample surface with $\boldsymbol{k}_{||} = (k_x, k_y)$ the in-plane momentum and $k_\perp$ the momentum perpendicular to the surface. The latter is not a good quantum number for (quasi) two-dimensional (2D) electronic states such as the surface states considered in this thesis and will be neglected in the following. The in-plane momentum $\boldsymbol{k}_{||}$ of the electrons is conserved in the photoemission process [30] and follows the relation

$$|\boldsymbol{k}_{||}| = \frac{1}{\pi}\sqrt{2m_e E_{kin}}\sin\theta_S, \tag{4}$$

where m_e is the electron mass and θ_S is the emission polar angle as measured from the surface normal.

The above consideration relies on a one electron picture, i.e. single electrons in an external potential V. However, the solid and its surface are complicated N-electron systems, where the electrons interact with each other, with phonons and with defects. In that respect, the photoemission process produces not only a photoelectron in a free-electron like state but also simultaneously promotes the quantum mechanical N-electron state into the excited $(N-1)$-electron state. To deal with the interactions taking place in the solid, it is useful to introduce quasiparticles [31] for the photoelectron and the photoholes left behind.

The spectral properties as measured by photoemission from a system of interacting electrons (quasiparticles) deviate from those of a system of non-interacting electrons in several aspects [27] and are described through the spectral function

$$A(\boldsymbol{k}_{||}, E) = \frac{\pi^{-1}\mathrm{Im}(\Sigma)}{(E - E_i(\boldsymbol{k}_{||}) - \mathrm{Re}(\Sigma))^2 + (\mathrm{Im}(\Sigma))^2}, \tag{5}$$

where $\Sigma(\boldsymbol{k}_{||}, E)$ is the complex self-energy. The two most prominent differences are a renormalization of the energy of the quasiparticles relative to the non-interacting system and a finite quasiparticle lifetime. Both the energy renormalization and the lifetime are described through the self-energy $\Sigma(\boldsymbol{k}_{||}, E)$, where the energy renormalization is related to the real part of the self-energy and the lifetime to the imaginary part. In paramagnetic metals, the self-energy contains, among others, contributions from electron-electron, electron-phonon and electron-defect scattering, [32, 33]

$$\Sigma = \Sigma^{el-el} + \Sigma^{el-ph} + \Sigma^{el-df}. \tag{6}$$

Whereas electron-electron and electron-phonon scattering are inelastic processes, electron-defect scattering is an elastic process. Correspondingly, electron-defect scattering results in a momentum broadening, while electron-electron and electron-phonon scattering cause an energy broadening. Note that as a consequence of the dispersion the energy broadening contributes to the measured momentum broadening and vice versa. The linewidth Γ corresponds to the inverse lifetime via $\Gamma = \hbar/\tau$ and is proportional to the imaginary part of the quasiparticle self energy according to

$$\Gamma = 2\mathrm{Im}(\Sigma). \tag{7}$$

Considering Rashba systems or more specifically the surface alloys on Ag(111), three aspects concerning the self energy should be pointed out:
(*i*) The surface alloys show a large amount of defects in comparison to clean (111) noble metal surfaces, as found in scanning tunneling microscope measurements (STM) for Bi/Ag(111). [34] Correspondingly, there is a large contribution to the linewidth from Σ^{el-df}. Moreover, the linewidths are strongly increased in the mixed binary surface alloys $\mathrm{Bi}_x\mathrm{Pb}_{1-x}$/Ag(111) and $\mathrm{Bi}_x\mathrm{Sb}_{1-x}$/Ag(111) for $x \approx 0.5$ and in the ternary surface alloy for $\mathrm{Bi}_x\mathrm{Pb}_y\mathrm{Sb}_{1-x-y}$/Ag(111) for $x \approx y \approx 0.33$ as a consequence of increasing disorder. For the surface states of Au(111) and Cu(111) linewidths in the order of 20 meV were measured. [7,35] On the stepped Al(001) surface on the other hand 267 meV were measured, where 101 meV were attributed to electron-defect scattering. [36] In the surface alloys on Ag(111), common linewidths measured with high resolution ARPES are larger than 100 meV, and it is feasible to assume that about half of the linewidth broadening is caused by electron-defect scattering.
(*ii*) The density of states (DOS) deviates from the DOS of a conventional 2D electron gas and for some energies ($E_{\bar{\Gamma}} < E < E_0$) the topology of the constant energy surface is changed (see Eq. 34 and Fig. 14), which was predicted to strongly enhance the electron-phonon coupling. [37] Quantitative measurements on the Au(111) surface state could not confirm this prediction. [38] However, the region where $E_{\bar{\Gamma}} < E < E_0$ is small for Au(111), and for systems where this region is large, as it is the case in e.g. Bi/Ag(111), notable deviations were predicted.
(*iii*) The peculiar spin structure of Rashba systems reduces the phase space for the decay of excited states due to the conservation of the electron spin in scattering events (in the absence of magnetic impurities). Correspondingly the quasiparticle lifetimes are enhanced. This is indirectly observed in STM experiments on Bi(110), where quasiparticle interference effects are found to be significantly altered due to the spin structure of the surface states. [39] Similarly, it is shown by STM for topological insulators that the spin structure of their surface states prevents backscattering. [40,41]

2.2 Spin- and angle-resolved photoemission experiments

In a spin- and angle-resolved photoemission experiment one aims at measuring the spin polarization, i.e. the expectation values of the spin operators of an ensemble of electronic states, in addition to the binding energy and the momentum. To achieve this, a spin polarimeter is combined with an electron energy analyzer. An intuitive idea would be to add a Stern-Gerlach-type of spin separator to an ARPES setup. However, it was argued that such a spin separator does not work for electrons as a consequence of the uncertainty principle. [42,43] On the other hand, more recently both experiments and calculations indicate the feasibility of a Stern-Gerlach-type of spin separator for electrons. [44–46]

At present, the most prominent type of spin polarimeters are based on spin-dependent scattering of electrons, where currently three different classes of polarimeters exist. One class is based on Mott scattering [42, 47–49], while others are based on spin-polarized low energy electron diffraction (SPLEED), [50] and very low energy electron diffraction (VLEED) [51, 52], also called low energy exchange scattering [53]. SPLEED relies on the different scattered intensities of the (2, 0) and ($\bar{2}$, 0) diffraction spots of low energy electrons ($E_{kin} \approx 100\ eV$) of a W(110) surface, which allows for the determination of one spin polarization component. VLEED uses the intensity difference in the specular reflected electron beam of ferromagnetic thin films when magnetized in opposite directions.

A Mott polarimeter, as used for the experiments presented in this thesis, relies on the spin-dependent cross section of relativistic electrons backscattered off atomic nuclei, with kinetic energies typically in the range 25 kV $\lesssim E_{kin} \lesssim$ 100 kV. After the electrons are energy and momentum filtered in the analyzer, they are accelerated towards a target, typically a thin gold foil. At the gold foil, electrons with spin up (down) are preferentially scattered to the right (left) yielding an intensity difference in the corresponding detectors, from which an asymmetry can be calculated. The asymmetry is related to the polarization via the Sherman function S. [54] The Sherman function is defined as the asymmetry which would be measured for a fully polarized beam. Although the Sherman function is a constant for a given setup, it is called function because it depends on several parameters such as the kinetic energy of the scattering electrons and (the range of) the detection angles. The figure of merit, defined as

$$\varepsilon = (N/N_0)S^2, \tag{8}$$

is low for Mott detectors, typically in the range $\varepsilon \sim 10^{-4} - 10^{-3}$. In Eq. 8 (N/N_0) is the ratio between the detected and the total number of incoming electrons.

There are two types of Mott polarimeters as schematically shown in Fig. 4, the classical Mott polarimeter, [55, 56] in which the electrons are detected at high kinetic energies, and the retarding type Mott polarimeter, where electrons are decelerated before they are detected. [57] In the classical Mott polarimeter, one uses discriminator levels in order to cut off multiply scattered electrons, whereas in the retarding type Mott polarimeter they are filtered by an aperture.

While other detectors yield higher figures of merit, the advantage of the classical Mott polarimeter is its high stability, which allows for SARPES setups with ultrahigh resolution. [58] In that respect, the figure of merit is not the only measure for the quality of a SARPES setup.

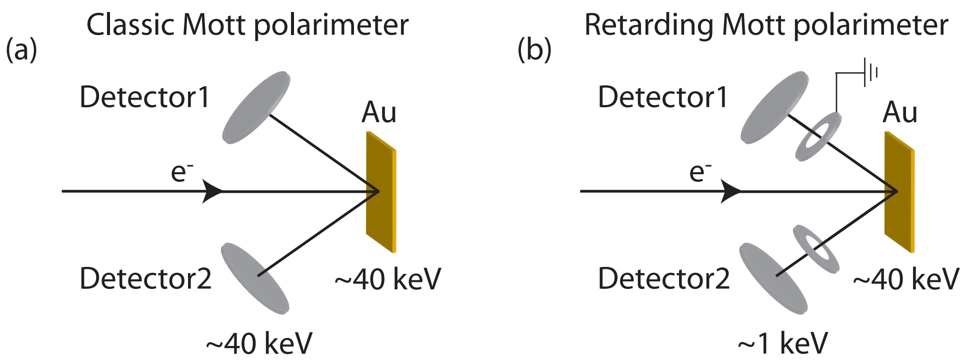

Figure 4: Schematic view of (a) a classical Mott polarimeter and (b) a retarding type Mott polarimeter. Relativistic electrons are directed at a gold foil and the backscattered electrons are counted by two opposite detectors. In the classical Mott polarimeter, the detectors are at the same voltage as the gold foil whereas in the retarding type Mott polarimeters the electrons are decelerated towards the detectors.

2.2.1 The COPHEE setup

The abbreviation COPHEE stands for the COmplete PHotoEmission Experiment. [59] This name is applicable because of the fact that the setup allows to measure all observables of the photoelectron, i.e. the kinetic energy E_{kin}, the momentum $\boldsymbol{k}$ and the spin polarization $\boldsymbol{P}$. COPHEE is positioned at the Surface and Interface Spectroscopy (SIS) beamline of the Swiss Light Source of the Paul Scherrer Institute. The use of the synchrotron radiation from the SIS beamline allows access to photon energies in the range of $10-800$ eV and variable light polarization.

The current manipulator is home built and has an axis for an azimuthal rotation and an axis for a polar rotation of the sample, [60] which in principle allows to access all $\boldsymbol{k}_{||}$ vectors within the limitation given by the photon energy (see Eq. 4). However, as a consequence of this design, a momentum distribution curve is always measured in the same geometry (see section 2.3). In order to overcome this limitation, the current manipulator will soon be replaced by a new one which in addition allows to tilt the sample, i.e. it additionally allows to rotate the sample around the horizontal axis lying in the sample plane.

The energy analyzer is an EA125 electrostatic hemispherical analyzer from Omicron. Electrons can be detected by three channeltrons as well as two Mott polarimeters. The Mott polarimeters are operated at 40 kV, and their Sherman functions equal $S = 0.085$ (see subsection 2.3.2). The figure of merit is $\varepsilon \sim 10^{-4}$. Given typical intensities as obtained from e.g. the Au(111) surface state, dwell times in the order of 100 sec yield statistical errors in the asymmetries $\Delta\tilde{A}_{\hat{\alpha}} \lesssim 2$ % (see Eq. 11). The energy and angular resolution when measured with the Mott polarimeters are typically set to 80 meV and ± 0.75°, respectively.

Through the employment of two Mott polarimeters, mounted with 90° between each other, and an electrostatic beam deflection system, which alternately deflects the beam in one of the polarimeters, it becomes possible to measure all components of the spin polarization vector. [59] It is the combination of this feature with a manipulator which allows to access different $\boldsymbol{k}_{||}$ vectors which sets the COPHEE setup apart from other spin-resolved setups. While magnetic systems have a well defined quantization axis, non-magnetic systems, where the spin splitting comes about due the combination of a broken space inversion asymmetry and the spin-orbit interaction, have a more complicated spin structure. This demands for experiments that are able to determine all components of the spin polarization vectors.

2.2.2 Spin polarization induced by the photoemission process

According to Eq. 2, the photons couple only directly to the momentum of the electrons, and correspondingly the measured spin polarization should in principle reflect the spin polarization of the initial states. Unfortunately, there are several processes which can cause a deviation between the measured spin polarization and the spin polarization of the initial states. [61]

First of all, states which are spin degenerate in the bulk can become spin polarized in the near surface region probed by photoemission. [62] The spin polarization in the vicinity of the surface is a consequence of the reflection of bulk Bloch states from the surface potential barrier and resembles the spin polarization of a Rashba system in the sense that it is zero for $\boldsymbol{k}_{||} = 0$ and in general finite for $\boldsymbol{k}_{||} \neq 0$. Moreover, like in a Rashba system the spin polarization is antisymmetric with respect to $\bar{\Gamma}$. As such, the measured spin polarization is the spin polarization of the probed initial states and a photoemission effect only in the sense that the photoemission has a finite probing depth.

Considering magnetic systems, the electron transport through the solid to the surface and into the vacuum can be spin dependent and even yield a spin-filtering effect. [63–65] In strong ferromagnets, where the majority band is completely filled and electron-hole pairs can only be created in the minority band, a spin-dependent reaction of the remaining electrons towards the excitation induced by the photoemission process can yield a reduction of the measured spin polarization. [66] However, in non-magnetic systems where the time reversal symmetry holds, the states are energetically degenerate and these effects are absent.

There are several mechanisms which can generate spin polarization from unpolarized states. As such, they do neither change the spin polarization of fully spin polarized states nor induce a spin splitting. The arguably most prominent effect is obtained when circular polarized light is used. [67–71] The spin polarization is created in the photoemission process from spin-orbit split initial states as a result of the selection rules for transitions produced by circularly polarized light, reflected by the matrix element t_{fi}. Illuminating a GaAs photocatode by a circularly polarized laser produces up to 43% spin polarization in the emitted electrons. [72] Photoemission with circularly polarized light from Cs atoms can, depending on the photon energy, even yield 100% spin polarization. [73]

At last, as a consequence of spin-orbit coupling, photoelectrons emitted from spin-degenerate bulk states can be spin polarized even when linearly polarized light or unpolarized light is employed. In such a case, the outcome depends strongly on the photon energy, symmetry of the solid and the particular surface as well as on the experimental geometry. [74–80] Similar to the case of circularly polarized light, the spin polarization of the photoelectrons is a consequence of spin-dependent matrix elements.

In resonant photoemission from magnetized Gd with circularly polarized light a spin-state interference was observed. [81] The interference occurs between the direct photoemission channel and the indirect excitation-autoionization channel, when the indirect channel is at resonance. The spin-state interference changes the direction but not the magnitude of the spin polarization. In fact, interference effects in the photocurrent can also occur in photoemission from Rashba systems as discussed in chapter 8. However, the interference mechanism is qualitatively different from the one discussed in Ref. [81].

Summarizing the effects mentioned above, it becomes clear that it is difficult not to measure spin polarization in a SARPES experiment.

2.3 Data analysis

In this section the analysis of SARPES data will be discussed, starting from the measured raw data. The discussion will involve a measurement of the surface states of Bi/Ag(111) for illustration. Bi/Ag(111) is a Rashba system and discussed in detail in sections 5 and 6. Here it is only of importance to note that in this system the surface states are (fully) spin polarized.

Before the process of data analysis is introduced, a precise description of the measurement and sample coordinate frame is necessary. Fig. 5 (a) shows the experimental setup and illustrates the difference between the sample coordinates $\alpha = x, y, z$ and the coordinates $\hat{\alpha} = \hat{x}, \hat{y}, \hat{z}$ defined by the Mott detectors.

There is an angle of 45° between the incoming light and the detected electrons, which defines the xz plane of the sample coordinate system. The x axis is defined by the intersection of this plane with the sample surface, the z axis is given by the sample normal and the y axis lies in the sample plane perpendicular to x. The z axis is the

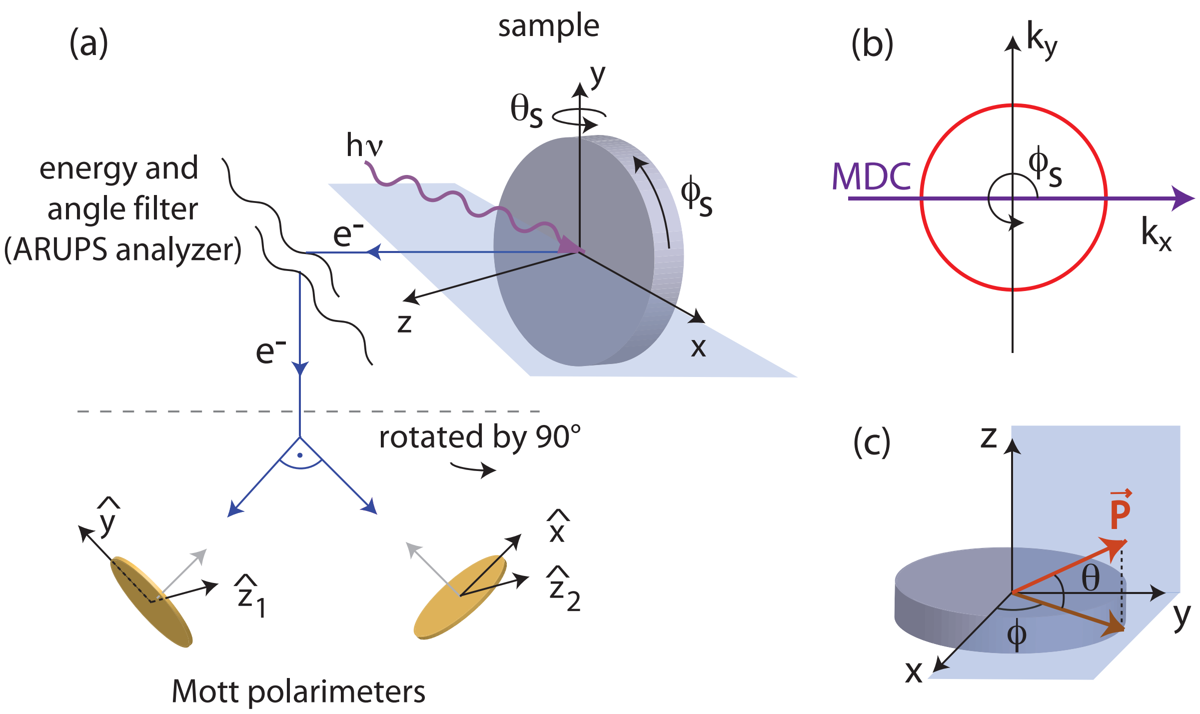

Figure 5: (a) Schematic illustration of the experimental setup, showing on the right hand side the sample geometry and on the left hand side the three-dimensional Mott polarimeter with two gold foils orthogonal to each other. The coordinate system given by the Mott polarimeters deviates from the sample coordinates through a rotation matrix R. (b) A momentum distribution curve cuts along k_x as illustrated by the thick violet line. (c) Illustration of the spin polarization vector in the sample coordinate system.

rotation axis of the azimuthal angle ϕ_S and the y axis is the rotation axis of the polar angle θ_S. While a polar rotation changes the sample normal (z axis) and the intersection of the plane spanned by the incoming light and the sample normal with the sample (x axis), the y axis is not affected. An azimuthal rotation does not rotate the coordinate system defined above, but is used to align the constant energy surface to the measurement plane. A momentum distribution curve (MDC) is measured by rotating the polar angle θ_S and correspondingly cuts along k_x as illustrated in Fig. 5 (b).

In the coordinate frame of the Mott detectors, each direction $\hat{\alpha}$ represents the normal to a scattering plane, defined by the electron incidence direction on the gold foil and two detectors for backscattered electrons. The $\hat{z}$ axis is parallel to the emission direction of the detected electrons. The $\hat{y}$ axis is rotated by 45° in the azimuthal direction with respect to the sample axis y. Similarly, the $\hat{x}$ axis is rotated by 45° in the azimuthal direction with respect to the sample axis x for $\theta_S = 0$. The relation between the sample coordinates and the coordinate system of the Mott detectors can be described through a rotation matrix R,

$$\begin{pmatrix} x \\ y \\ z \end{pmatrix} = R \begin{pmatrix} \hat{x} \\ \hat{y} \\ \hat{z} \end{pmatrix} = \begin{pmatrix} \cos\theta_S/\sqrt{2} & -\cos\theta_S/\sqrt{2} & \sin\theta_S \\ 1/\sqrt{2} & 1/\sqrt{2} & 0 \\ -\sin\theta_S/\sqrt{2} & \sin\theta_S/\sqrt{2} & \cos\theta_S \end{pmatrix} \begin{pmatrix} \hat{x} \\ \hat{y} \\ \hat{z} \end{pmatrix}. \tag{9}$$

The rotation matrix R is an orthogonal transformation, i.e. $R^T = R^{-1}$. Note that the transformation matrix defined in Eq. 9 differs from the one given in Ref. [59] because throughout this thesis the sample coordinate frame refers to the measurement direction and thus $\phi_S = 0$.

A spin-resolved measurement performed at COPHEE yields the spectra $\tilde{I}^i_{M\hat{\alpha}}$ as shown in Fig. 6 (a) for a momentum distribution curve (MDC) of Bi/Ag(111), where $i = 1, 2$ corresponds to the two opposite detectors covering direction $\hat{\alpha}$. From the intensity data $\tilde{I}^i_{M\hat{\alpha}}$ the asymmetry data $\tilde{A}_{M\hat{\alpha}}$ are calculated by using

$$\tilde{A}_{M\hat{\alpha}} = \frac{\tilde{I}^1_{M\hat{\alpha}} - \tilde{I}^2_{M\hat{\alpha}}}{\tilde{I}_{M\hat{\alpha}}}, \tag{10}$$

where $\tilde{I}_{M\hat{\alpha}} = \tilde{I}^1_{M\hat{\alpha}} + \tilde{I}^2_{M\hat{\alpha}}$. The states located at $k_x \approx \pm 0.11$ Å^{-1} and $k_x \approx -0.25$ Å^{-1} are approximately spin polarized along the y axis. Due to the 45° rotation of the axes $\hat{x}$ and $\hat{y}$ of the Mott coordinate system with respect to the sample axes x and y at $k_x = 0$, $\tilde{A}_{M\hat{x}}$ and $\tilde{A}_{M\hat{y}}$ are very similar. The state located at $k_x \approx -0.36$ Å^{-1} is only visible as a shoulder and features an out-of-plane spin polarization component as reflected in the increase of the asymmetry data $\tilde{A}_{M\hat{z}}$ on the left side. Each data point has a statistical error $\Delta\tilde{A}_{M\hat{\alpha}}$ due to the electron counting given by

$$\Delta\tilde{A}_{M\hat{\alpha}} = (\tilde{I}^1_{M\hat{\alpha}} + \tilde{I}^2_{M\hat{\alpha}})^{-1/2}. \tag{11}$$

The asymmetry data $\tilde{A}_{M\hat{\alpha}}$ however comprise instrumental asymmetries, which arise from asymmetries in both the detection efficiencies of the individual detectors and the detector setup including the electron optics. In principle, these instrumental asymmetries can be removed by adjusting the discriminator levels of the detectors. [82] Though in practice, an entire removal of the instrumental asymmetries is difficult. In magnetic systems the instrumental asymmetries can be removed by considering cross asymmetries, i.e. the asymmetry difference $\tilde{A}^C_{M\hat{\alpha}} = \tilde{A}^+_{M\hat{\alpha}} - \tilde{A}^-_{M\hat{\alpha}}$, where the + and the − correspond to the opposite magnetization directions. In non-magnetic systems, sensitivity factors $s^i_{\hat{\alpha}}$ are used to calibrate opposite detectors and the asymmetries are calculated as

$$A_{M\hat{\alpha}} = \frac{s^1_{\hat{\alpha}}\tilde{I}^1_{M\hat{\alpha}} - s^2_{\hat{\alpha}}\tilde{I}^2_{M\hat{\alpha}}}{s^1_{\hat{\alpha}}\tilde{I}^2_{M\hat{\alpha}} + s^2_{\hat{\alpha}}\tilde{I}^2_{M\hat{\alpha}}} = \frac{I^1_{M\hat{\alpha}} - I^2_{M\hat{\alpha}}}{I_{M\hat{\alpha}}}, \tag{12}$$

where $I^i_{M\hat{\alpha}} = s^i_{\hat{\alpha}}\tilde{I}^i_{M\hat{\alpha}}$ and $I_{M\hat{\alpha}} = I^1_{M\hat{\alpha}} + I^2_{M\hat{\alpha}}$. The sensitivity factors $s^i_{\hat{\alpha}}$ can in principle be experimentally determined by measuring a non spin-polarized electron beam. However,

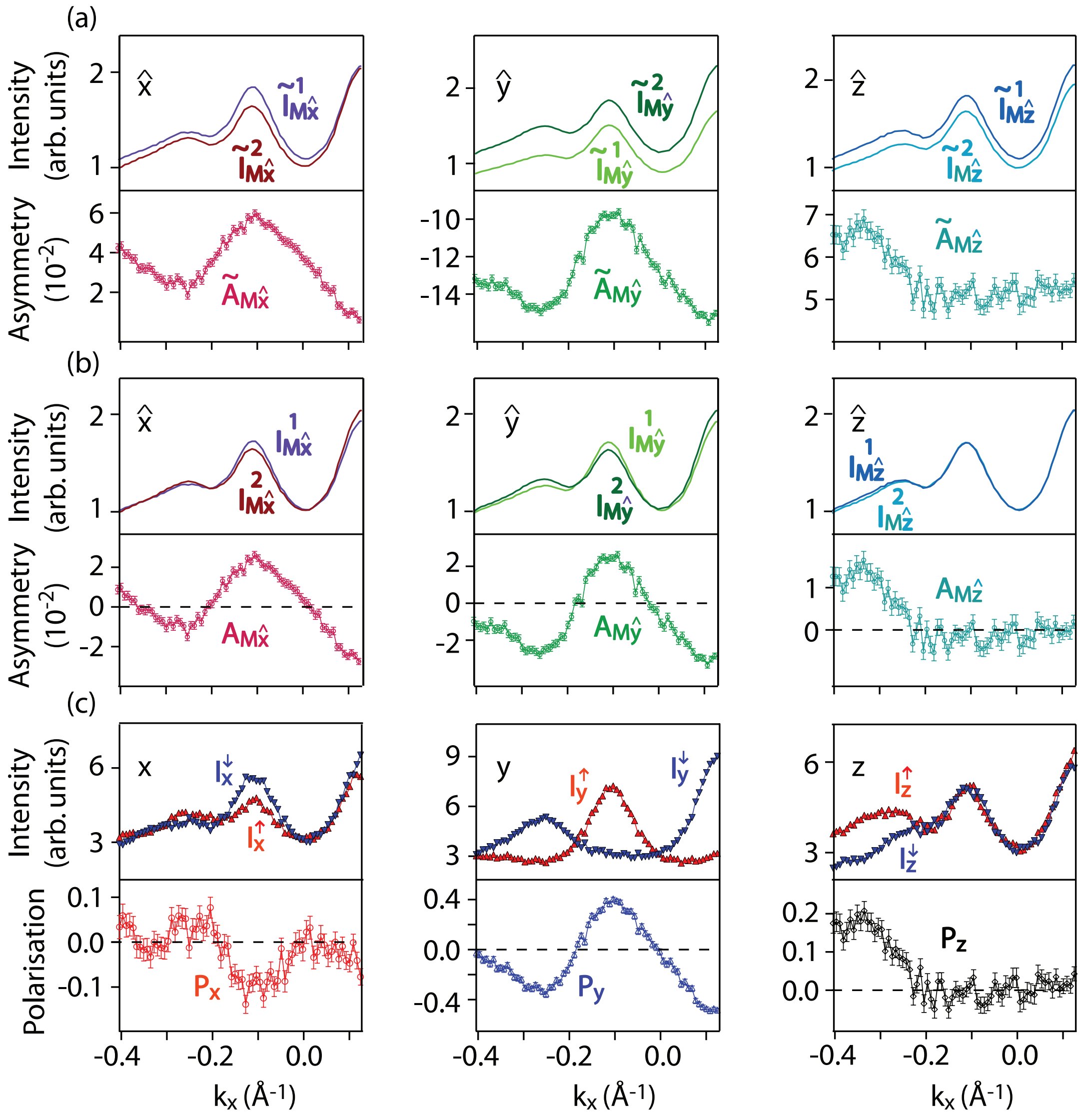

Figure 6: Data analysis of a spin-resolved MDC of Bi/Ag(111). (a) Intensity data $\tilde{I}^i_{M\hat{\alpha}}$ (top panels) as measured on the individual channels in the Mott coordinate frame ($\hat{\alpha} = \hat{x}, \hat{y}, \hat{z}$) and the corresponding asymmetry data $\tilde{A}_{M\hat{\alpha}}$. (b) Intensity data $I^i_{M\hat{\alpha}}$ and asymmetry data $A_{M\hat{\alpha}}$ after alignment with the sensitivity factors. (c) Spin-resolved intensities $I^\uparrow_\alpha$, $I^\downarrow_\alpha$ and corresponding spin polarization data P_α in the sample coordinate frame ($\alpha = x, y, z$).

this is delicate and time consuming and in general empirical sensitivity factors are used. The calibrated intensity data and the corresponding asymmetries of Bi/Ag(111) are shown in Fig. 6 (b). Due to the low efficiency of the Mott detectors, as captured by the small value $S = 0.085$ of the Sherman function, the bands show significant intensities $I^i_{M\hat{\alpha}}$ on all detectors although they are fully spin polarized. The relative intensity differences are small, which leads to asymmetry data $A_{M\hat{\alpha}}$ in the order of a few percent. The spin polarization data $P_{M\hat{\alpha}}$ in the coordinate system of the Mott detectors are obtained by dividing the asymmetry data by the Sherman function,

$$P_{M\hat{\alpha}} = \frac{A_{M\hat{\alpha}}}{S}. \tag{13}$$

The spin polarization data $\boldsymbol{P}$ in the sample coordinates are then obtained by applying the rotation matrix R to the spin polarization data $\boldsymbol{P}_M$,

$$\begin{pmatrix} P_x \\ P_y \\ P_z \end{pmatrix} = R \begin{pmatrix} P_{M\hat{x}} \\ P_{M\hat{y}} \\ P_{M\hat{z}} \end{pmatrix}. \tag{14}$$

Since the rotation matrix is orthogonal it preserves the magnitude of the spin polarization, i.e. $|R\boldsymbol{P_M}| = |\boldsymbol{P}|$. The spin polarization $\boldsymbol{P}$ is often represented in polar coordinates with the angles θ and ϕ as defined in Fig. 5 (c),

$$\boldsymbol{P} = c\ (\cos\theta\cos\phi, \cos\theta\sin\phi, \sin\theta), \tag{15}$$

where c is the magnitude of the spin polarization. The error bars in the spin polarization data can be approximated by $\Delta P_\alpha = \Delta\tilde{A}_{M\hat{\alpha}}/S$, which holds if for all i and $\hat{\alpha}$ the sensitivity factors are close to one, $s^i_{\hat{\alpha}} \approx 1$. The spin-resolved intensities $I^\uparrow_\alpha$ and $I^\downarrow_\alpha$ as projected on the axis α can be calculated as

$$I^\uparrow_\alpha = \frac{1}{2}I(1+P_\alpha) \qquad I^\downarrow_\alpha = \frac{1}{2}(1-P_\alpha), \tag{16}$$

where $I = I_{M\hat{\alpha}} = I^\uparrow_\alpha + I^\downarrow_\alpha$, and correspondingly

$$P_\alpha = \frac{I^\uparrow_\alpha - I^\downarrow_\alpha}{I}. \tag{17}$$

Note that using this convention we have $\sum_\alpha I^\uparrow_\alpha + I^\downarrow_\alpha = 3I$. Fig. 6 (c) shows the spin polarization data P_α and the spin-resolved intensities $I^{\uparrow,\downarrow}_\alpha$ for Bi/Ag(111).

Fig. 7 shows a synthesized set of SARPES data of an artificial MDC. The spectrum shown in Fig. 7 (a) features one peak sitting on a background. The peak is chosen to be spin polarized along the positive z axis, i.e. $\boldsymbol{P} = (0,0,1)$, and the background is unpolarized. Correspondingly, as shown in Fig. 7 (a), the spin polarization data P_x and P_y equal zero and P_z shows a peak. The error bars are small when the intensity I is large. The spin-resolved intensities $I^{\uparrow,\downarrow}_\alpha$ corresponding to the data of Fig. 7 (a) are given in Fig. 7 (b). The physical meaning of these intensities are the following: as there is no spin polarization component along the x and y directions, both up and down spins have equal weight in the related projections of the photoelectron current. On the other hand, the photoelectron peak is fully polarized along the z direction, resulting in a peak in the $I^\uparrow_z$ spectrum only, while the unpolarized background is equally distributed over the two projections.

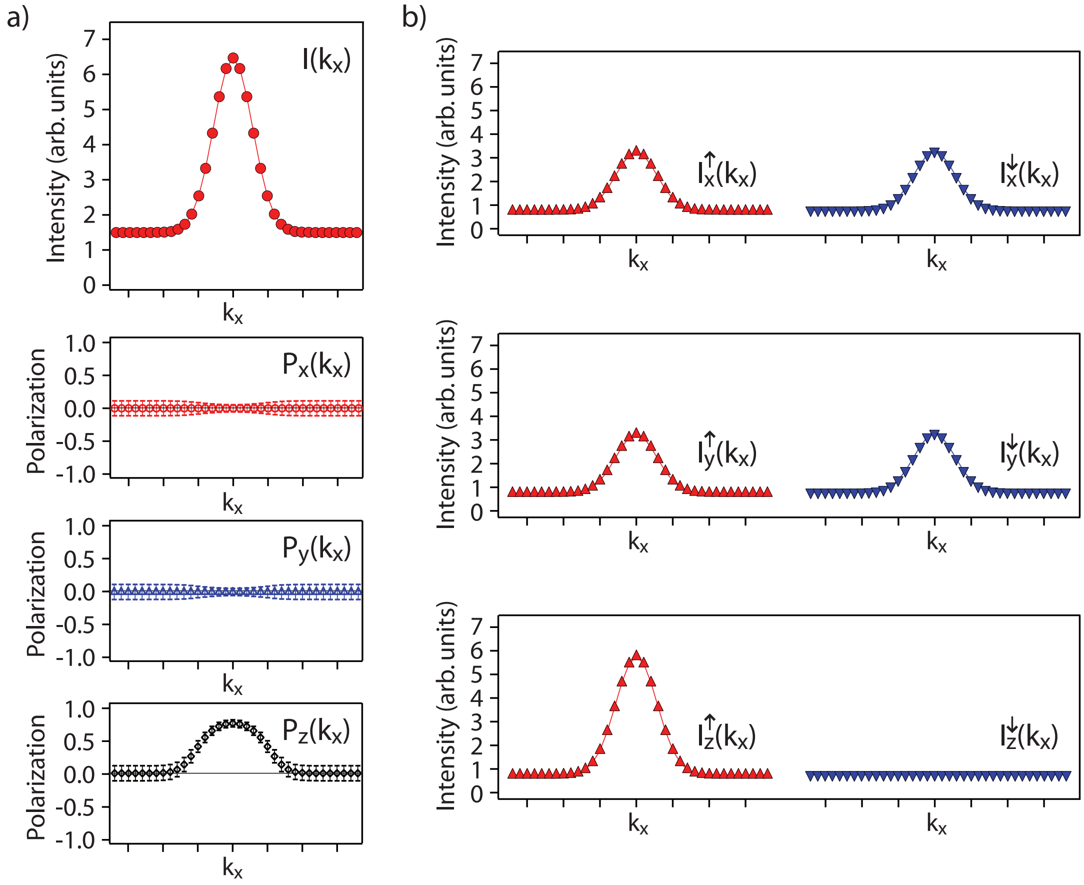

Figure 7: Illustration of the relation between the data $I(k_x)$ and $P_\alpha(k_x)$ shown in (a) and the spin-resolved intensities $I_\alpha^{\uparrow,\downarrow}$ as shown in (b) for a peak with $\boldsymbol{P} = (0, 0, 1)$.

2.3.1 Two-step fitting routine

In SARPES experiments on magnetic systems, a geometry can often be chosen such that the sample magnetization direction is aligned with the analysis direction $\hat{\alpha}$ of one of the Mott detector pairs. The recovery of spin-resolved spectra for spin up and spin down with respect to this axis is then straightforward based on Eqs. 16. However, in systems with strong spin-orbit interaction, it has recently become clear that situations with non-collinear spins may arise within the same spectrum, exemplified by the case of surface states on surface alloys of Bi and Pb on Ag(111), where some states are polarized mainly in the surface plane while others show considerable out-of-plane polarization (see sections 6.1 and 6.2). The recovery of the spin polarization vector of each state then requires a vectorial approach also in the analysis of the SARPES data, such as the two-step fitting routine presented in the following.

In this two-step fitting routine, one first analyzes the spin-integrated intensity data $I(E, \boldsymbol{k}_{||})$, by using well-established curve fitting routines with either Gaussian, Lorentzian or more complex peak shapes. Let us for the sake of clarity assume that we are dealing with MDC data scanning along k_x. The goal of this first step is to separate, for each data point, as accurately as possible the contributions from the individual bands and the background to the overall photoemission current, as is illustrated in Fig. 8(a). The result of the fit is then written as

$$I(k_x) = \sum_{i=1}^{n} I^i(k_x) + B(k_x), \tag{18}$$

where $I^i(k_x)$ represent the individual peaks and $B(k_x)$ the background, which in the case of MDCs can often be a constant or a simple linear function. The number of fitting parameters in this first step is then typically $3n + 1$, corresponding to a value for the position, width and intensity for each of the n peaks plus a constant background.

In preparation of the second step, which is the fitting of the spin polarization spectra, a spin polarization vector P_i is assigned to each peak as

$$\boldsymbol{P}^i = c_i \; (\cos\theta_i \cos\phi_i, \cos\theta_i \sin\phi_i, \sin\theta_i). \tag{19}$$

The two angles θ_i and ϕ_i, as well as the length of the polarization vector c_i, corresponding to the direction and the degree of polarization for each peak, will now be the fitting parameters. Their number is thus $3n$. From the total intensities and the spin polarization components, one can now generate the spin-resolved spectra along the three coordinate axes according to Eqs. 16 (see also Fig. 7 (b)). Note that for arbitrary directions of the spin polarization vector, each peak contributes to all six spin-resolved spectra as

$$\begin{aligned}
I_x^{i,\uparrow}(k_x) &= I^i(k_x)(1 + P_x^i)/2 = I^i(k_x)(1 + c_i \cos\theta_i \cos\phi_i)/2, \\
I_x^{i,\downarrow}(k_x) &= I^i(k_x)(1 - P_x^i)/2 = I^i(k_x)(1 - c_i \cos\theta_i \cos\phi_i)/2, \\
I_y^{i,\uparrow}(k_x) &= I^i(k_x)(1 + P_y^i)/2 = I^i(k_x)(1 + c_i \cos\theta_i \sin\phi_i)/2, \\
I_y^{i,\downarrow}(k_x) &= I^i(k_x)(1 - P_y^i)/2 = I^i(k_x)(1 - c_i \cos\theta_i \sin\phi_i)/2, \\
I_z^{i,\uparrow}(k_x) &= I^i(k_x)(1 + P_z^i)/2 = I^i(k_x)(1 + c_i \sin\theta_i)/2, \\
I_z^{i,\downarrow}(k_x) &= I^i(k_x)(1 - P_z^i)/2 = I^i(k_x)(1 - c_i \sin\theta_i)/2,
\end{aligned} \tag{20}$$

and the total spin-resolved spectra, e.g. along the y direction, are thus obtained as

$$\begin{aligned}
I_y^{\uparrow}(k_x) &= B(k_x)/2 + \sum_{i=1}^{n} I^i(k_x)(1 + \cos\theta_i \sin\phi_i)/2, \\
I_y^{\downarrow}(k_x) &= B(k_x)/2 + \sum_{i=1}^{n} I^i(k_x)(1 - \cos\theta_i \sin\phi_i)/2.
\end{aligned} \tag{21}$$

Here, the background is assumed to be unpolarized and therefore distributed evenly over the two spin-resolved spectra for each component α, as indicated in Fig. 7. The result of

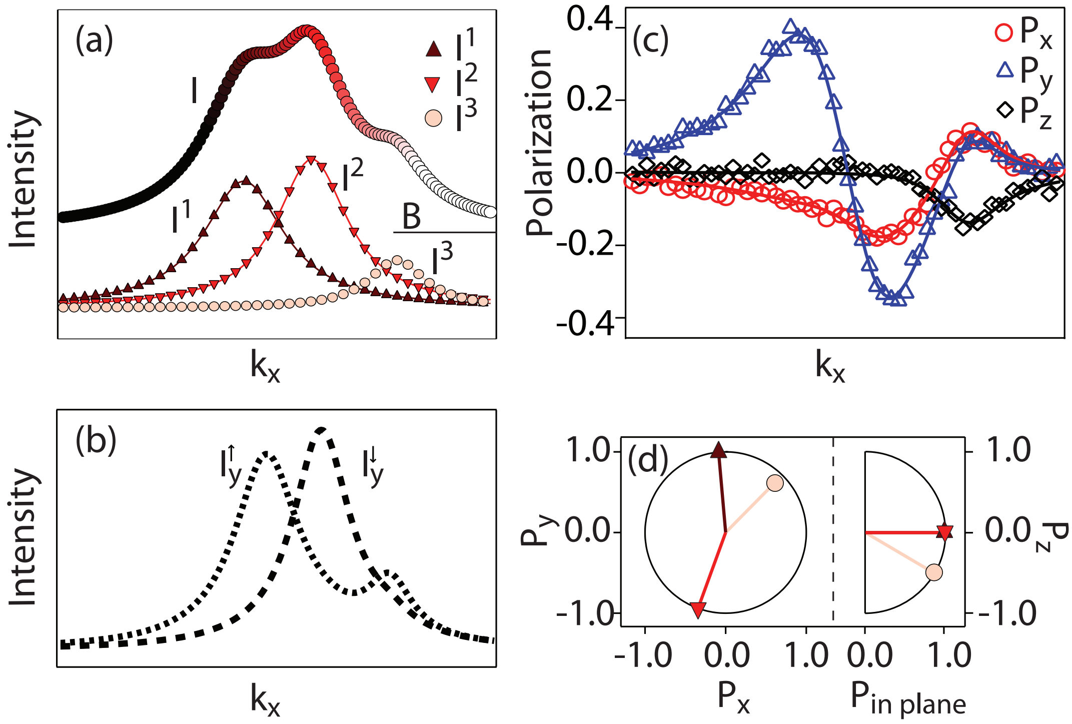

Figure 8: Illustration of the vectorial spin analysis with synthesized data. (a) Spin-integrated intensities for a MDC along k_x, showing also the peaks and the background extracted from the intensity fit. (b) Spin-resolved spectra for the y component, based on the spin polarization vectors for the individual peaks shown in (d). (c) Spin polarization spectra (symbols) for all three spin components, which were obtained from curves like those given in (b) by using Eq. 17. The lines show the spin polarization curves obtained by using the two-step fitting routine. (d) In-plane (left) and out-of-plane (right) components of the spin polarization vectors of the different peaks as obtained from the spin polarization fit. The symbols correspond to those in (a).

this procedure is shown in Fig. 8 (b), for polarization vectors as indicated in Fig. 8 (d). It can be noted that peak $I^1(k_x)$ is assigned a spin polarization vector $P^1 \approx (0, 1, 0)$ and therefore shows up only in the $I_y^{\uparrow}(k_x)$ spectrum, while P^2 points almost in the opposite direction and $I^2(k_x)$ correspondingly shows up predominantly in the $I_y^{\downarrow}(k_x)$ spectrum. From these six spin-resolved spectra, it is straightforward to calculate point by point the spin polarization spectra along k_x by applying Eq. 17. The resulting curves are shown in Fig. 8 (c), here already for the best fit to the previously synthesized spin polarization data using the same vectors $\boldsymbol{P}^i$. In the case of real SARPES data, the second step consists thus in varying these polarization vectors, defining $3n$ parameters, until the best fit to the three experimental spin polarization curves $P_\alpha(k_x)$ has been reached. Overall, this two-step routine may appear to be fitting with an enormous number of parameters. However,

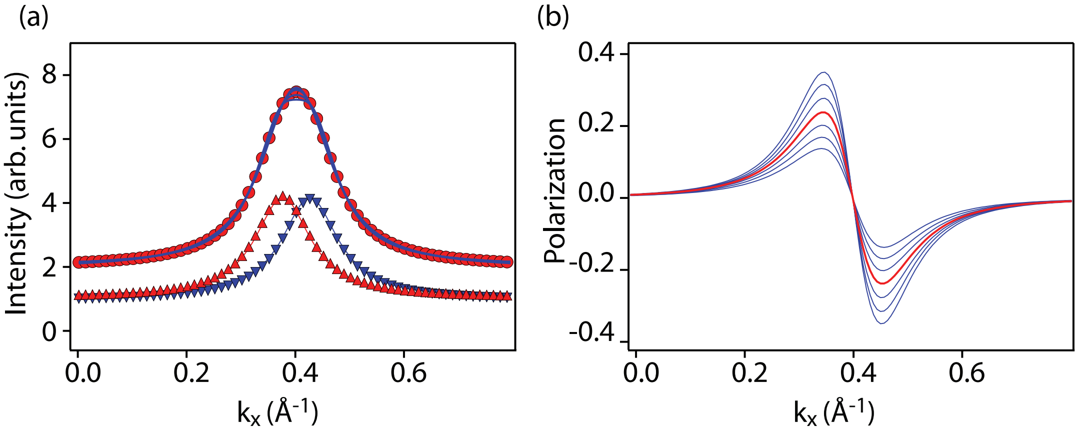

Figure 9: Synthesized SARPES MDC curves illustrating the sensitivity of such data for quantifying spin splittings. (a) Two fully and oppositely spin-polarized peaks (up and down triangles), separated by $\Delta k_x = 0.05$ Å^{-1}, add up to the spin-integrated intensity data (circles). The solid (blue) lines represent best fits to the latter when the splitting is varied in steps of 0.006 Å^{-1} symmetrically around the initial value while the widths and the intensities are optimized. Except for a small region near the peak maximum, all curves fall on top of each other. (b) Variation of the spin polarization curves for the same spin splittings as in the fits in (a). The center (red) curve corresponds to the original splitting.

the two steps are carried out completely independently, with the first step corresponding to common practice in the analysis of ARPES data, and with the second step providing enormous constraints to the angles and magnitudes of the spin polarization vectors by fitting concurrently three independent SARPES curves. The benefits of this procedure will be illustrated in the following sections.

The assumption of a non-polarized structureless background may not apply to all situations, e.g. when studying magnetic systems, or when dealing with surface resonances where spin-orbit scattering in the final state might introduce spin polarization in the underlying bulk continuum. In principle, the two-step fitting routine can also deal with such situations, the pay-off being an increased number of fitting parameters required to describe the structure and polarization of the background. In the spin-orbit split surface states considered in this thesis, there was no need to include such effects in order to produce excellent fits with sensible spin polarization vectors for all bands.

The method can also be useful in a different way. There are situations where the SARPES data indicate a spin splitting of two bands by the typical up-and-down deflection of the spin polarization curve for one vector component, whereas the spin-integrated data do not allow to resolve two peaks. The spin can be used as a tag for identifying the individual contributions of the two split peaks. In Fig. 9, the sensitivity of this procedure is analyzed, again by using synthesized data. The spin-integrated intensity data shown in (a) are produced by summing the two spin-resolved spectra given in Fig. 9 (a), representing two fully polarized peaks of opposite spin which are separated by $\Delta k_x = 0.05$ Å^{-1}. The result is a single peak with no indication of a splitting. On the other hand, the resulting polarization curve, calculated by using Eq. 17 and plotted as a red line in Fig. 9 (b), shows a marked up-and-down deflection with an amplitude of about 0.25. The splitting of the two peaks was then varied in steps of 0.006 Å^{-1} symmetrically around the initial value of Δk_x while their intensities and widths were optimized for the best fit to the original peak. All the fitted curves are contained within the marker size of the latter, and it would thus be impossible to quantify the correct splitting from these data alone. However, the amplitude of the spin polarization curve is very sensitive to these small changes, with higher amplitudes for larger splittings. The effect is so pronounced because, while the peaks move apart, they also have to reduce their width in order to fit the original spin-integrated peak, thus reducing the overlap even further. For quantum well states in ultrathin Pb films on Si(111) (see subsection 4.1.1 and Ref. [83]), this method has been successfully applied to measure Rashba-type spin splittings in EDCs as low as 10 meV.

2.3.2 Determination of the Sherman function

The two-step fitting routine directly accesses the spin polarization vectors associated with the individual peaks in the spectra and can thus serve as a reliable tool to determine the values intrinsic to the system at hand. However, the absolute values of spin polarization of the measured states are inversely proportional to the Sherman function S (see below), which should be known precisely. The experimental determination of S however is a highly complex issue. [48, 84] Here we illustrate the effect that a slight miscalibration of the Sherman function has on the spin-resolved spectra, with the SARPES data from Pb/Ag(111) shown in section 6.2 as an example. Further, we suggest two simple and straightforward procedures for obtaining reliable values of S. The more precise procedure is based on the two-step fitting routine and relies, in the presented case, on the measured states to be fully spin polarized. However, it can easily be extended to systems, where the states are not fully polarized, but the degree of polarization of the states contributing to the spectrum is known.

For the 3D Mott polarimeter of COPHEE, the Sherman function was calibrated to be $S = 0.085$ for each of the four detector pairs, based on measurements and two-step fitting analyses on a variety of surface states that are spin split by the Rashba-Bychkov effect. With this value for S, these surface states are all consistently found to be fully spin polarized ($c_i = 1.0$). It seems unlikely that nature has conspired to reduce the spin polarization on all these different systems by the same factor, and we therefore use this value with confidence. The relatively low value arises because the instrument uses large solid angle detectors in order to maximize the figure of merit, [85] because it is operated at a comparably low 40 keV acceleration voltage for the extended measuring periods needed for SARPES and due to the quality of the gold foil.

The interdependency between the values c_i and the Sherman function can be evaluated by the relation

$$A_\alpha(k_x) = S \cdot P_\alpha(k_x) = S \cdot (I_\alpha^\uparrow(k_x) - I_\alpha^\downarrow(k_x))/I_\alpha(k_x) = S \cdot \sum_{i=1}^{n} I^i(k_x) c_i \hat{P}_\alpha^i / I_\alpha(k_x) \qquad (22)$$

staying with the notation used in the previous sections and considering the MDC data measured along k_x. Here, we have introduced polarization unit vectors $\hat{P}_\alpha^i$. If all states i have the same degree of polarization, say $c_i =: c_0$, then the relation between the degree of polarization and the Sherman function becomes

$$A_\alpha(k_x) I_\alpha(k_x) = S \cdot P_\alpha(k_x) I_\alpha(k_x) = S \cdot c_0 \cdot \sum_{i=1}^{n} I^i(k_x) \hat{P}_\alpha^i \qquad (23)$$

Since both, the asymmetries $A_\alpha(k_x)$ and the spin-integrated intensities $I(k_x)$, represent measured quantities, the left-hand side of Eq. 23 remains unaffected by the analysis, and increasing the value of the Sherman function thus produces lower degrees of spin polarization c_0 in the data analysis. If the c_i values differ for different peaks in the same spectrum, the dominant peaks will see their coefficient c_i vary roughly inversely proportional to the assumed value of S.

In Rashba systems like Pb/Ag(111), the spin quantization axis depends on the electron momentum. However, for the MDCs passing along the $\bar{\Gamma}\bar{M}$ line, the quantization axis has been found to be the same for the two spin-split states closest to $\bar{\Gamma} = 0$, where it is along the y axis. For the outer spin-split states, the spin polarization vector shows an additional out-of-plane component (see subsection 6.2). Considering the inner set of bands, this allows for a meaningful representation of the data in terms of spin-resolved intensity spectra $I_y^\uparrow(k_x)$ and $I_y^\downarrow(k_x)$ with respect to the quantization axis y. In general the spin-resolved intensities loose their physical meaning once they refer to an axis off the quantization axis. In Fig. 10, the spin-resolved intensities are shown, calculated from real SARPES data using Eqs. 16 and $P_\alpha = A_\alpha/S$, and assuming different Sherman functions. Of course, this kind of representation is no longer justified for the outer two states, which feature strong out-of-plane components, and we will thus only discuss features related to the inner set of spin-split bands. In the center of Fig. 10, the curves obtained for $S = 0.085$ are shown. A momentum shift of 0.05 Å^{-1} between the two spin components

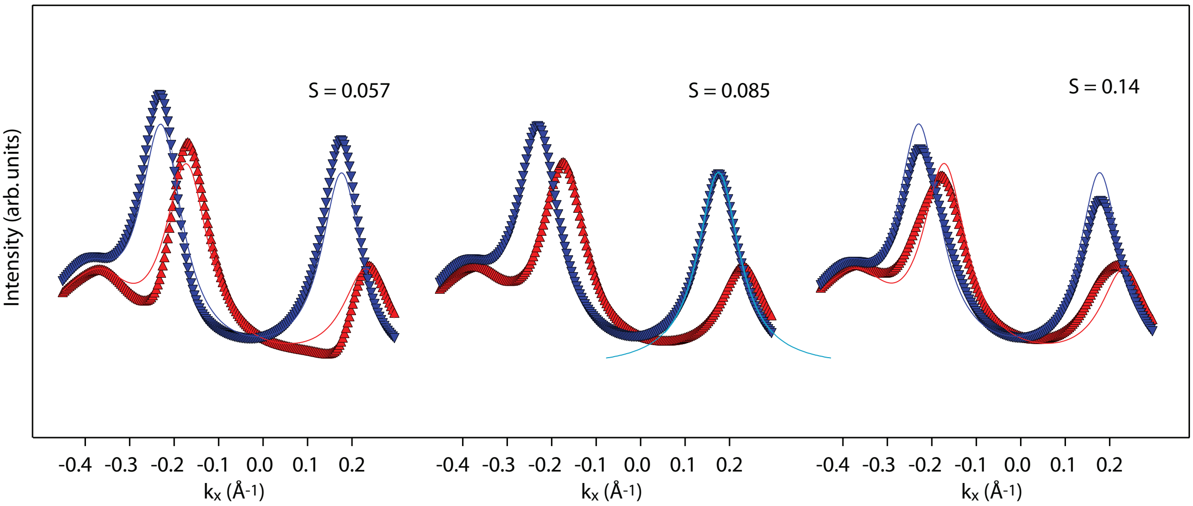

Figure 10: Spin-resolved intensities $I_y^{\uparrow}(k_x)$ (red) and $I_y^{\downarrow}(k_x)$ (blue) evaluated for different Sherman functions S calculated from the experimental asymmetry spectrum $A_y(k_x)$ (data of Fig. 33). The Sherman function of the instrument has been determined as $S = 0.085$. The thin solid lines underlying the curves for $S = 0.057$ and 0.14 give the intensities for $S = 0.085$ as a reference. The thin solid line under the curve for $S = 0.085$ shows one of the symmetric Voigt functions [86] used for the intensity fit.

is observed between the inner two bands. The four peaks exhibit highly symmetric line shapes that can be well fitted with Voigt functions, as is indicated for the first peak at $k_x > 0$. When the same data is analyzed with a reduced Sherman function of 0.057, the peaks become asymmetric, with steeper slopes in the regions of peak overlap, and the spin splitting is slightly increased. Intensities in one spin channel can be pulled down considerably with respect to the $S = 0.085$ reference curve in regions where the other spin channel has high intensities. The opposite scenario is found when $S = 0.14$ is used in the data analysis. The spin-resolved peaks have additional intensities in regions of overlap and become strongly asymmetric. With respect to $S = 0.085$, the spin splitting is slightly reduced in this case.

These effects can be brought out more clearly in synthesized spectra, modeling a simpler situation with only two peaks of opposite spin polarization sitting on a constant background (Fig. 11). A lowering of the Sherman function leads to unphysical negative intensities in the regions of peak overlap, while too high a value produces asymmetric peak broadening. Fig. 11 indicates the kind of statistical accuracy that one needs in order to determine the true Sherman function with a precision of 5%. Considering the values of S given in Fig. 10, this procedure is in general not very precise for real data. Nevertheless, this analysis indicates that the spin-resolved spectra, and in particular the spin splittings, are relatively robust with respect to relatively large variations in the

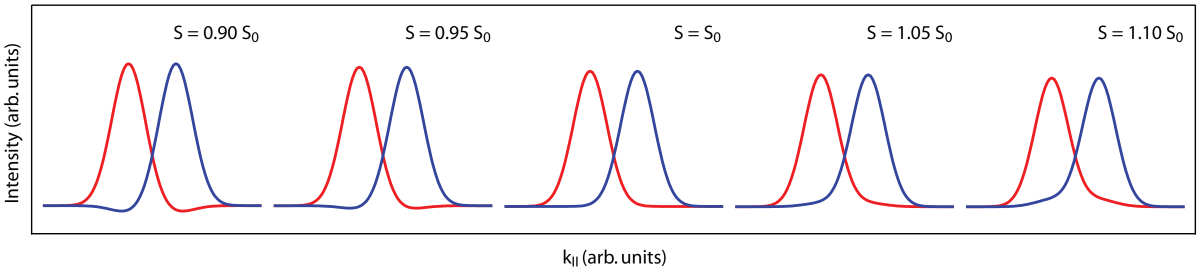

Figure 11: Spin-resolved intensities $I_y^{\uparrow}(k_x)$ and $I_y^{\downarrow}(k_x)$ calculated from the same synthesized intensity and asymmetry spectra but using different Sherman functions S as indicated. The original spectra represent two completely and oppositely spin-polarized peaks on a constant, unpolarized background, assuming a Sherman function $S = S_0 = 0.085$ for generating the asymmetry spectrum.

Sherman function.

The method described so far is entirely model independent, but is limited by the modest statistical accuracy that is usually obtained in SARPES data due to the poor detector efficiencies. The situation can be improved by using the two-step fitting routine, because the statistical error in the fitted spin polarization vectors, and hence in the spin-resolved spectra, is significantly smaller than the statistical error in the raw SARPES data because the two-step fitting routine addresses an ensemble of data points. Moreover, the fit parameters c_i represent an independent check for the correctness of the Sherman function: according to Eq. 23 the values of c_i vary inversely proportional to the value of S. Since the degree of spin polarization can not exceed 100% ($c_i = 1.0$), the fitting can provide an absolute lower limit for the Sherman function. In other words, the asymmetry amplitude measured in the raw data requires a minimum Sherman function for it to be physical. If one believes in theoretical predictions that spin-split bands in clean 2D Rashba systems, like the surface states on Au(111) or Pb/Ag(111), are 100% spin polarized, [80, 87] or if one knows the degree of spin polarization c_i of certain bands, one obtains a direct measure for the Sherman function. This is how the value of $S = 0.085 \pm 0.003$ is determined for the Mott polarimeters of COPHEE and used in the analysis of the data presented in this thesis.

Of course, the reliability of the procedure for the determination of the Sherman function presented above depends crucially on the quality of the curve fitting in the first step. A similar method was applied recently for the absolute calibration of a spin polarimeter behind a time-of-flight spectrometer for laser-excited SARPES, using Au(111) as a reference sample. [88]

3 The Rashba effect

Many physical systems can be classified by means of symmetry. In this respect, the bulk of a solid and its surface belong to different classes, and the surface of a solid is more than just the truncation of the bulk. At the surface, the translational symmetry is broken, which also brakes the space inversion symmetry, and a large variety of phenomena can occur which are symmetry forbidden in the bulk. An example of such a physical phenomenon is the so-called Rashba effect, which was initially formulated by Bychkov and Rashba for a 2D electron gas at the interfaces of semiconductor heterostructures. [3] A comprehensive discussion of spin-orbit coupling in 2D electron and hole systems in general can be found in Ref. [89].

In this chapter the Rashba-Bychkov model (henceforth Rashba model) will be introduced. While this model was initially developed for semiconductor quantum wells the term Rashba effect is by now commonly used for other systems with broken translational symmetry such as surface states, which are in the focus of this thesis. The Rashba model yields a good qualitative agreement for both 2D electron gases in semiconductor heterostructures and surface states, as exemplified for an $\mathrm{In}_x\mathrm{Ga}_{1-x}\mathrm{As}/\mathrm{In}_y\mathrm{Al}_{1-y}\mathrm{As}$ heterostructure [90] and for the surface state of Au(111), where the typical spin-split band structure could be observed for the first time for a surface state. [6] At last, the spin field-effect transistor will be introduced. In chapter 4 the quantitative failure of the Rashba model will be discussed, which lies in the disregard of the atomic nature of a solid state system, and the necessary refinements will be introduced.

3.1 The Rashba-Bychkov model

In band theory, it is commonly assumed that the space inversion symmetry and the time reversal symmetry are fulfilled. Considering an electron with momentum $\boldsymbol{k}$ and spin $\boldsymbol{s}$ ($\uparrow$ or $\downarrow$), the space inversion operator K changes the sign of the momentum but leaves the spin unaffected. For a space inversion symmetric system, the Hamiltonian H is invariant under the space inversion operator K, i.e. $[H, K] = HK - KH = 0$. This means that when space inversion symmetry holds the energy of the electron is the same regardless whether it moves in one direction with momentum $\boldsymbol{k}$ or in the opposite direction with momentum $-\boldsymbol{k}$ as represented by the equation $E(\boldsymbol{k}, \uparrow) = E(-\boldsymbol{k}, \uparrow)$. A time reversal operator T on the other hand both changes the sign of the momentum and flips the spin. For a time reversal symmetric system we have $[H, T] = 0$ and correspondingly the Kramers degeneracy $E(\boldsymbol{k}, \uparrow) = E(-\boldsymbol{k}, \downarrow)$. In any system where both the space inversion symmetry and the time reversal symmetry are fulfilled, the electronic states are spin degenerate, $E(\boldsymbol{k}, \uparrow) = E(\boldsymbol{k}, \downarrow)$. If however the potential through which the charge

carriers move is inversion asymmetric, the spin-orbit coupling lifts the spin degeneracy. This is the case in systems with structure inversion asymmetry (SIA) of the confinement potential and in systems with bulk inversion asymmetry (BIA). For states confined in a potential with SIA, e.g. interface or surface states, the spin splitting is caused by the Rashba effect, [91] while in systems with BIA, e.g. a zinc-blende structure, the spin splitting is caused by the Dresselhaus effect. [92]
Considering a 2D nearly free electron or hole gas with effective mass m^*, the Rashba Hamiltonian can be written as

$$H = H_0 + H_R, \tag{24}$$

where H_0 represents the kinetic energy according to

$$H_0 = \sigma_0 \left(E_{\bar{\Gamma}} + \frac{\hbar^2}{2m^*}\nabla^2 \right), \tag{25}$$

while the Rashba term is given by

$$H_R = -\alpha_R \left(i\sigma_y \frac{\partial}{\partial x} - i\sigma_x \frac{\partial}{\partial y} \right). \tag{26}$$

The coupling constant α_R is a material dependent parameter which reflects the strength of the Rashba effect and $E_{\bar{\Gamma}}$ is the energy at the $\bar{\Gamma}$ point where $\boldsymbol{k} = 0$. The unit 2×2 matrix is denoted by σ_0, while σ_x and σ_y are standard Pauli matrices in the basis where the quantization axis is along the z axis,

$$\sigma_x = \begin{pmatrix} 0 & 1 \\ 1 & 0 \end{pmatrix} \qquad \sigma_y = \begin{pmatrix} 0 & -i \\ i & 0 \end{pmatrix} \qquad \sigma_z = \begin{pmatrix} 1 & 0 \\ 0 & -1 \end{pmatrix}. \tag{27}$$

It is important to note that for the Hamiltonian defined in Eqs. (24-26) we have $[H, T] = 0$. Correspondingly the Kramers degeneracy $E(\boldsymbol{k}, \uparrow) = E(-\boldsymbol{k}, \downarrow)$ still holds and in equilibrium both Rashba and Dresselhaus systems carry no net magnetic moment.
The Rashba term defined in Eq. (26) is a result of the spin-orbit coupling Hamiltonian

$$H_{SOI} = -\frac{i\hbar^2}{2m^2}(\boldsymbol{\nabla} V \times \boldsymbol{\nabla}\ ) \cdot \boldsymbol{\sigma}. \tag{28}$$

H_R can be derived from H_{SOI} under the assumption that the only finite value of the the potential gradient $\boldsymbol{\nabla} V$ is along the positive z direction. In Eq. (28) $\boldsymbol{\sigma}$ is the vector of Pauli matrices. From the combination of Eq. (26) and Eq. (28) it is obvious that the Rashba constant α_R captures the size and the sign of the potential gradient. However, if only the potential gradient perpendicular to the surface is taken into account, the predicted spin splittings are orders of magnitude too small. As will be explained in chapter 4, both the electric fields of the nuclei and structural factors enter the Rashba constant.

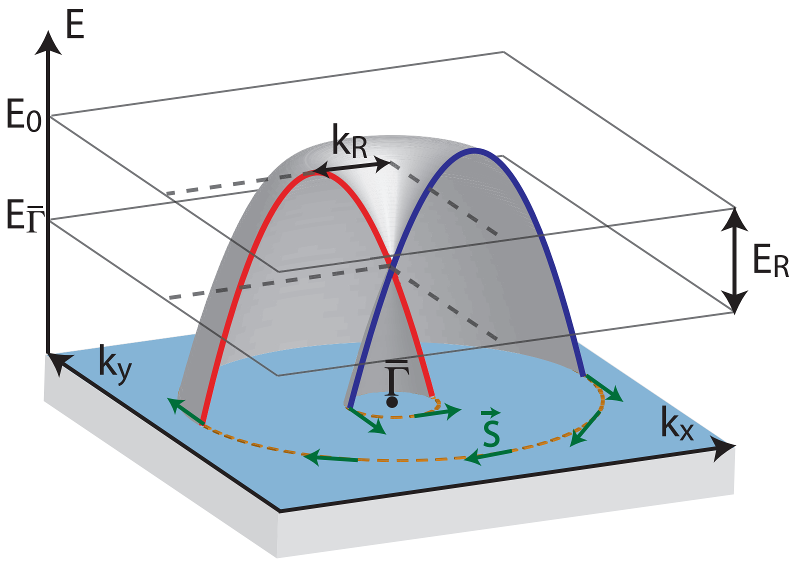

Figure 12: Schematic picture of the Rashba effect for a two-dimensional hole gas around $\bar{\Gamma}$ and illustration of the relevant parameters. The green arrows are the spin expectation values of the eigenspinors for $\alpha_R > 0$.

The eigenenergies of the Hamiltonian H given in Eq. (24) yield upper (+) and lower (-) Rashba branches according to

$$E_{\pm}(\boldsymbol{k}_{||}) = E_{\bar{\Gamma}} + \frac{\hbar^2|\boldsymbol{k}_{||}|^2}{2m^*} \pm \alpha_R|\boldsymbol{k}_{||}|, \tag{29}$$

with the corresponding eigenspinors

$$\left\langle \boldsymbol{k}_{||}, \pm \right| = \left(e^{i(\varphi \mp \pi/2)} \quad , \quad 1 \right) / \sqrt{2}, \tag{30}$$

where $\varphi = \arctan(k_y/k_x)$. It should be noted that the subscripts $\pm$ in Eq. (29) correspond to the case where $\alpha_R > 0$ and have to be interchanged for $\alpha_R < 0$. In Eq. (30) the in-plane momentum $\boldsymbol{k}_{||} = (k_x, k_y)$ has been used instead of $\boldsymbol{k}$ due to the 2D nature of a Rashba system. The energy difference between the upper and the lower Rashba branches are $\boldsymbol{k}_{||}$ dependent, $E_+(\boldsymbol{k}_{||}) - E_-(\boldsymbol{k}_{||}) = 2\alpha_R|\boldsymbol{k}_{||}|$.

The spin polarization vectors $\boldsymbol{S}_{\pm}(\boldsymbol{k}_{||})$ are defined as the expectation values of the eigenspinors $\left\langle \boldsymbol{k}_{||}, \pm \right|$ and can be calculated as

$$\boldsymbol{S}_{\pm}(\boldsymbol{k}_{||}) = \left\langle \boldsymbol{k}_{||}, \pm \right| \boldsymbol{S} \left| \boldsymbol{k}_{||}, \pm \right\rangle = \frac{\hbar}{2} \begin{pmatrix} \pm\sin\varphi \\ \mp\cos\varphi \\ 0 \end{pmatrix}, \tag{31}$$

where $\boldsymbol{S} = \hbar/2 \cdot \boldsymbol{\sigma}$ is the spin operator for spin-1/2 particles. Since the spin polarization vectors given in Eq. (31) are in-plane perpendicular to the momentum $\boldsymbol{k}_{||}$ and correspondingly depend on the angle φ, there is no global spin quantization axis for a Rashba

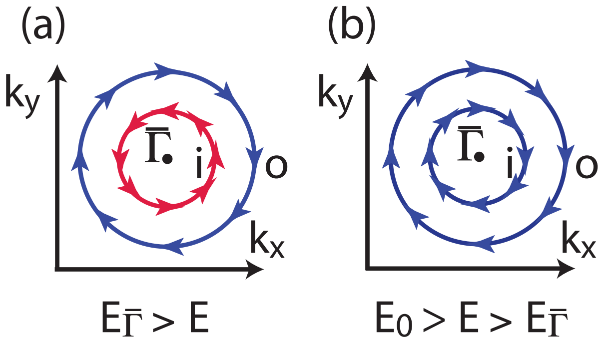

Figure 13: Schematic picture of the constant energy spin textures of a two-dimensional hole gas for $\alpha_R > 0$ and (a) $E < E_{\bar{\Gamma}}$ as well as (b) $E_0 > E > E_{\bar{\Gamma}}$. The arrows represent the spin polarization vectors.

system. Hence the branches $E_{\pm}(\boldsymbol{k}_{||})$ are not called spin-up and spin-down branches in general.

The dispersion and the spin structure of a Rashba system are shown in Fig. 12 for the case of a 2D hole gas. A cut through the dispersion along a radial direction passing through the $\bar{\Gamma}$ point shows two spin-split bands, depicted in blue and red. These spin-split bands are often referred to as a Kramers pair in the context of Rashba-like systems. They are offset from the $\bar{\Gamma}$ point by $\pm k_R$, the Rashba momentum, which is related to the Rashba constant as follows

$$|\alpha_R| = \frac{\hbar^2 k_R}{|m^*|}. \tag{32}$$

At a fixed energy E the momentum splitting between the two parabolas shown as red and blue in Fig. 12 is constant and equals $2k_R$.

The Rashba energy E_R is defined as the difference between E_0, the energy of the band apex, and $E_{\bar{\Gamma}}$, the energy of the crossing point,

$$E_R = E_0 - E_{\bar{\Gamma}} = \frac{\hbar^2 k_R^2}{2|m^*|}. \tag{33}$$

The spin structure is such that the spin polarization vectors are in-plane and rotate tangentially around the constant energy contours as shown in Fig. 12, where the arrows represent the spin polarization vectors. For a hole gas with a positive coupling constant $\alpha_R > 0$ and $E < E_{\bar{\Gamma}}$ the spin polarization vectors rotate clockwise along the outer (o) constant energy contour and counterclockwise along the inner (i) constant energy contour as shown in Fig. 13 (a). For a constant energy plane at $E_0 > E > E_{\bar{\Gamma}}$ and $\alpha_R > 0$ the spin polarization vectors rotate clockwise along both contours (Fig. 13 (b)). It should be noted that in the case of either a negative coupling constant α_R or a positive effective mass m^* the sense of rotation is reversed compared to Fig. 13. In this thesis, the

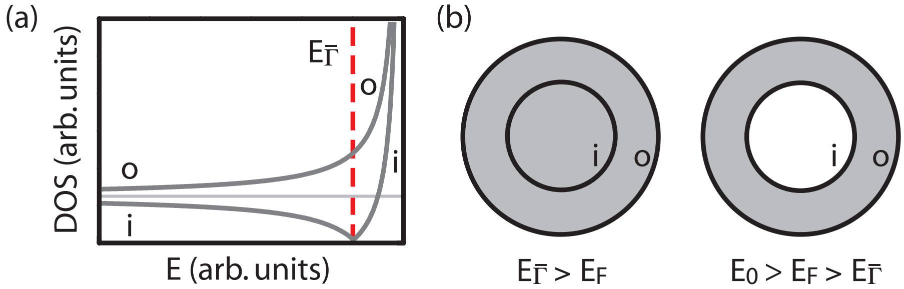

Figure 14: (a) Density of states for the outer (o) and the inner (i) constant energy contours. (b) Schematic picture of the Fermi sea for (left) $E < E_{\bar{\Gamma}}$ and $E_0 > E > E_{\bar{\Gamma}}$ (right).

term negative chirality is used for the situation depicted in Fig. 13 and positive chirality for the reversed case. Whereas the absolute value of α_R can in principle be determined with spin-integrated ARPES, the sign is only accessible with spin-resolved measurements. Although there is no global spin quantization axis, all states cut by a straight line through $\bar{\Gamma}$ under the angle φ have either parallel or antiparallel spin polarization vectors. Hence the notion spin up and spin down is commonly used in reference to such a cut. Despite the presence of fully spin-polarized states, the integration over the entire Fermi sea yields zero as a consequence of the Kramers degeneracy.

A remarkable feature of a Rashba gas can be found in its density of states (DOS), shown in Fig. 14 (a). For a standard 2D electron or hole gas the DOS is given by the constant $2 \cdot \nu_{2D} = 2 \cdot |m^*|/(2\pi\hbar^2)$, where the factor of 2 accounts for the spin degeneracy. In contrast to this, the DOS of a 2D Rashba (hole) gas is given by

$$\nu_{o,i}(E) = \Theta(E_0 - E)\nu_{2D} \left| 1 \pm \sqrt{\frac{E_0 - E_{\bar{\Gamma}}}{E_0 - E}} \right|, \tag{34}$$

where Θ is the Heaviside function (see Appendix A for detailed calculations of the DOS). The $+$ refers to the outer contour o and the $-$ to the inner contour i. The sum $\nu_o(E) + \nu_i(E)$ reduces to the constant DOS $2 \cdot \nu_{2D} = |m^*|/(\pi\hbar^2)$ of a 2D electron or hole gas with parabolic dispersion when $E < E_{\bar{\Gamma}}$, has a singular derivative for $E = E_{\bar{\Gamma}}$, while it displays a 1D Van Hove-type singularity $\nu(E) \sim (E_0 - E)^{-1/2}$ in the limit $E \rightarrow E_0$. This singularity can for some systems be measured by scanning tunneling spectroscopy (STM) and delivers an alternative pathway for the determination of the Rashba energy E_R. [34] The unusual DOS given in Eq. 34 has lead to a number of proposals of intriguing effects related to the DOS, among them changes in the electron-phonon coupling [37] or more generally the renormalization of the Fermi liquid parameters. [93] The arguably most prominent proposal is the enhancement of the superconducting transition temperature in the regime $E_0 > E_F > E_{\bar{\Gamma}}$. [94]

The origin of the divergence of the DOS in the vicinity of E_0 can also be found by examination of the Fermi sea. When the Fermi level approaches the band apex the group velocity goes to zero but the Fermi surface does not collapse to one point, in contrast to a spin-degenerate hole gas. Fig. 14 (b) shows the schematic hole Fermi seas for the regions $E_{\bar{\Gamma}} > E_F$ and $E_0 > E_F > E_{\bar{\Gamma}}$. In the region where $E_{\bar{\Gamma}} > E_F$ the Fermi sea consists of a fully filled circular disk, while in the region $E_0 > E_F > E_{\bar{\Gamma}}$ it is given by the 2D version of a torus, hence there is a topological change of the Fermi sea which occurs at $E_F = E_{\bar{\Gamma}}$. Note that this topological change is not related to the topology as defined for topological insulators.

3.2 Examples: Au(111) and $\mathbf{In}_x\mathbf{Ga}_{1-x}\mathbf{As}/\mathbf{In}_y\mathbf{Al}_{1-y}\mathbf{As}$

The Rashba model predicts two parabolas shifted in momentum space by twice the Rashba momentum k_R with respect to each other. For states located at the surface, ARPES allows to map the band structure, which is not possible for states located a few 100 nm inside a crystal, as it is the case for 2D electron gases (2DEG) in semiconductor heterostructures. As a consequence, the peculiar band structure of a Rashba system is conveniently studied for surface states and was first observed for the surface state of Au(111). [6] Although the experiments described in Ref. [6] did not engage spin resolution, the two parabolas shifted by $\Delta k = 0.023$ Å^{-1} were correctly addressed as Rashba-type spin-split bands. However, as already mentioned in section 3.1 and discussed in Ref. [6], the Rashba model fails to capture the large size of the spin splitting when the only contribution to the Rashba constant α_R is the electric field perpendicular to the surface.

The experimental Fermi surface and the dispersion of the surface state measured with (spin-integrated) ARPES are shown in Fig. 15 (a) and (b), respectively. The arrows in Fig. 15 (a) indicate the spin structure expected according to Eq. 31. The Fermi surface, which consists of two concentric circles, and the dispersion are in agreement with Eq. 29 for $\alpha_R = 0.33$ eVÅ. Figs. 15 (c)-(e) show SARPES data obtained at $E_b = 170$ meV, where (c) shows the total intensity I, (d) the in-plane spin polarization projected on the tangential direction and (e) the out-of-plane spin polarization component. The spin structure has a positive chirality, i.e. $\alpha_R > 0$. The deviations from the spin structure expected according to Eq. 31 in both the radial (not shown) and the out-of-plane direction are within the experimental errors, and hence for the spin structure of Au(111) a perfect agreement with the Rashba model is obtained. Recent SARPES experiments on vicinal Au surfaces [95] indicate that the spin structure is robust against structural defects in the form of step edges. The size of the spin splitting was found to be the same as for Au(111) as long as the surface states are located on the (111) terraces, and it is increased when

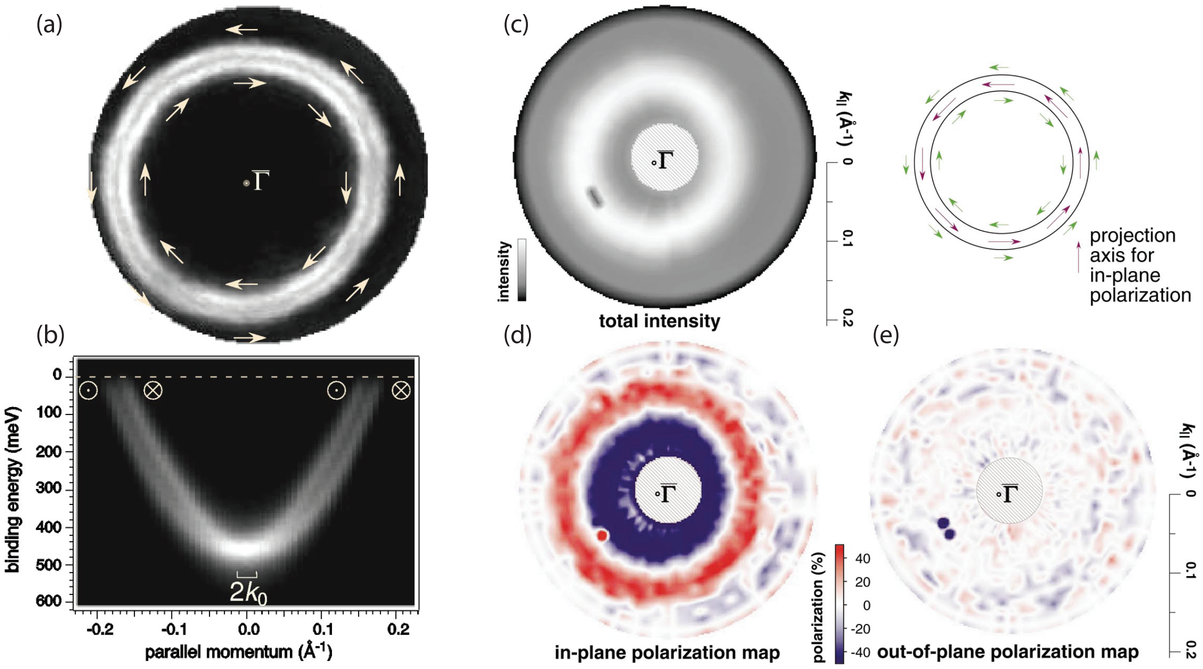

Figure 15: (a) Fermi surface map and (b) dispersion map as measured with spin-integrated ARPES. (c)-(e) Measured spin-resolved momentum distribution map for $E_b = 170$ meV. (c) Total intensity map and sketch of the Fermi surface and the predicted spin structure. Purple arrows indicate projection axes for in-plane polarization. (d) and (e) show the polarization maps in a color-scale representation, (d) for the in-plane component and (e) for the out-of-plane component of the polarization vector. The in-plane polarization (d) is a projection on the tangents to the circular Fermi surface. Red (blue) indicates a counterclockwise (clockwise) spin orientation. (adapted from Ref. [9])

the terrace width is decreased such that the wave function is delocalized over several terraces. This finding can be understood when considering the structural contribution to the Rashba model as discussed in section 4.2.

The Rashba effect for 2DEG in semiconductor heterostructures has a smaller size as compared to the effect for the surface states on heavy metal crystals. Considering In$_x$Ga$_{1-x}$As/In$_y$Al$_{1-y}$As, the Rashba parameter α_R is in the order of 10^{-2} eV Å. [96] It should be noted that although In$_x$Ga$_{1-x}$As/In$_y$Al$_{1-y}$As crystallizes in the zinc-blende structure and correspondingly features a finite Dresselhaus effect, the dominant mechanism inducing the spin splitting is the Rashba effect. As ARPES is not applicable for states located further away from the surface, the size of the spin splittings have to be determined by other methods. A frequently used method relies on the Shubnikov-de Haas oscillations, where the zero-field splitting, i.e. the Rashba-type spin splitting at the Fermi level, is estimated by extrapolation of the high magnetic field data to

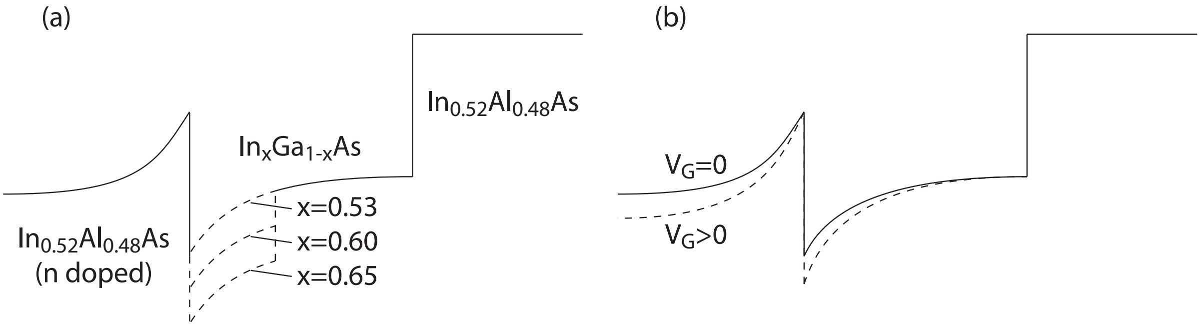

Figure 16: (a) Schematic band diagrams of the $\mathrm{In}_x\mathrm{Ga}_{1-x}\mathrm{As}/\mathrm{In}_y\mathrm{Al}_{1-y}\mathrm{As}$ heterostructures for $x = 0.53$, 0.60 and 0.65. (b) Change in the band diagram when a gate voltage V_G is applied.

$B = 0$. [90,97] Another method is time-resolved Kerr rotation, where the spin precession frequency of drifting electrons is measured, from which the Rashba parameters can be determined. [98]

Fig. 16 (a) shows the schematic band diagram of the $\mathrm{In}_x\mathrm{Ga}_{1-x}\mathrm{As}/\mathrm{In}_{0.52}\mathrm{Al}_{0.48}\mathrm{As}$ heterostructures ($x = 0.53$, 0.60 and 0.65) measured in Ref. [97], where the 2D electron gas is located in the region of the left interface of the $\mathrm{In}_x\mathrm{Ga}_{1-x}\mathrm{As}$ quantum well (in the region of the dotted lines). The energy scale for the Rashba-type spin splitting was measured via Shubnikov-de Haas oscillations and found to depend on x, i.e. 1.5 meV for $x = 0.53$, 2.5 meV for $x = 0.60$ and 2.4 meV for $x = 0.65$.

In Fig. 16 (b) the effect of a positive external gate voltage, applied on the left side, on the band diagram is illustrated. Due to the gate voltage, the slope in the region of the left interface is modified and the 2D electron gas experiences a larger potential gradient perpendicular to the interface. According to Eq. 28 this allows to control the size of the Rashba-type spin splitting via the term $\boldsymbol{\nabla} V$. Indeed, the size of the Rashba-type spin splitting is sensitive to this modification of the potential gradient across the interface as shown in Ref. [90] for $\mathrm{In}_{0.53}\mathrm{Ga}_{0.47}\mathrm{As}/\mathrm{In}_{0.52}\mathrm{Al}_{48}\mathrm{As}$ by means of Shubnikov-de Haas oscillations. The measured Rashba constant is found to depend linearly on the gate voltage, where e.g. $\alpha_R \approx 0.07$ eV Å was measured for $V_G = 0$ V and 0.08 eV Å for $V_G = -1$ V. Similar results were obtained in GaAs/AlGaAs quantum well states with time-resolved Kerr rotation. [98] However, the increased Rashba-type spin splitting as a function of the gate voltage can rather be understood as a consequence of the increased asymmetry in the envelope function of the 2DEG due to the increased asymmetry in the confinement potential than due to the increased electric field itself.

3.3 Spin rotation and the spin field-effect transistor

In 1990, Datta and Das published the proposal of the electronic analog of the electro-optic modulator, [96] which is by now referred to as the spin field-effect transistor. It relies on the peculiar band and spin structure of a Rashba system to achieve a controlled spin rotation along the electrons path.

In order to understand the spin field-effect transistor it is necessary to consider the mathematical description of the electron spin. The quantum mechanical operators associated with spin observables are given by $\boldsymbol{S} = \hbar/2 \cdot \boldsymbol{\sigma}$. In the case of spin-1/2 particles, $\boldsymbol{\sigma}$ is the vector of Pauli matrices. For simplicity, we use throughout this section the basis in which the quantization axis is along the y direction, where

$$\sigma_x = \begin{pmatrix} 0 & -i \\ i & 0 \end{pmatrix} \qquad \sigma_y = \begin{pmatrix} 1 & 0 \\ 0 & -1 \end{pmatrix} \qquad \sigma_z = \begin{pmatrix} 0 & 1 \\ 1 & 0 \end{pmatrix}. \tag{35}$$

Each Pauli matrix σ_i has the eigenvalues ±1 and the corresponding eigenspinors are given by

$$\langle x^{\uparrow,\downarrow}| = \frac{1}{\sqrt{2}} \begin{pmatrix} 1 \\ \pm i \end{pmatrix} \quad \langle y^{\uparrow}| = \begin{pmatrix} 1 \\ 0 \end{pmatrix} \quad \langle y^{\downarrow}| = \begin{pmatrix} 0 \\ 1 \end{pmatrix} \quad \langle z^{\uparrow,\downarrow}| = \frac{1}{\sqrt{2}} \begin{pmatrix} 1 \\ \pm 1 \end{pmatrix}. \tag{36}$$

Considering Eqs. 36 it is of importance to note that the coherent superposition of a spin-up and a spin-down spinor leads to a spin state with a spin polarization vector normal to the spin polarization of the initial spinors. It is this principle which is exploited in the proposal of the spin field-effect transistor. Moreover, similar effects can even be observed in SARPES experiments as shown in chapter 8.

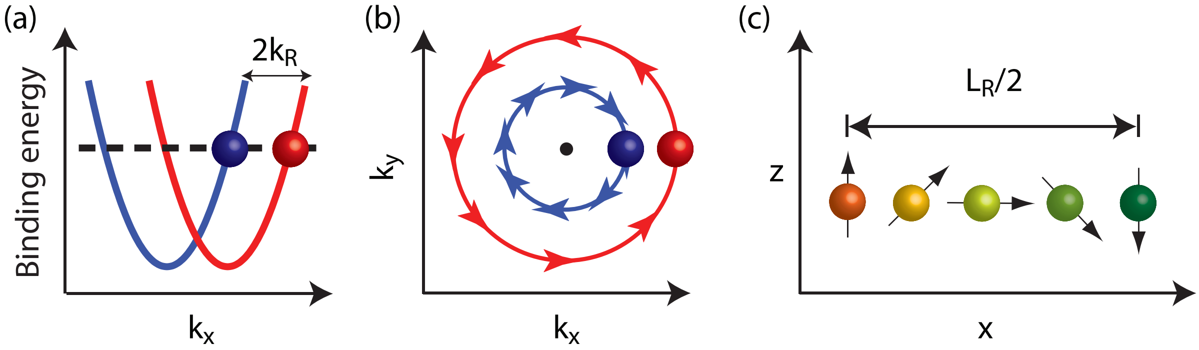

Figure 17: (a) Schematic dispersion and (b) Fermi surface spin textures of a 2D Rashba electron gas. The dotted line in (a) indicates the position of the Fermi level. (c) Spin rotation in the xz plane along the electrons path through a Rashba system.

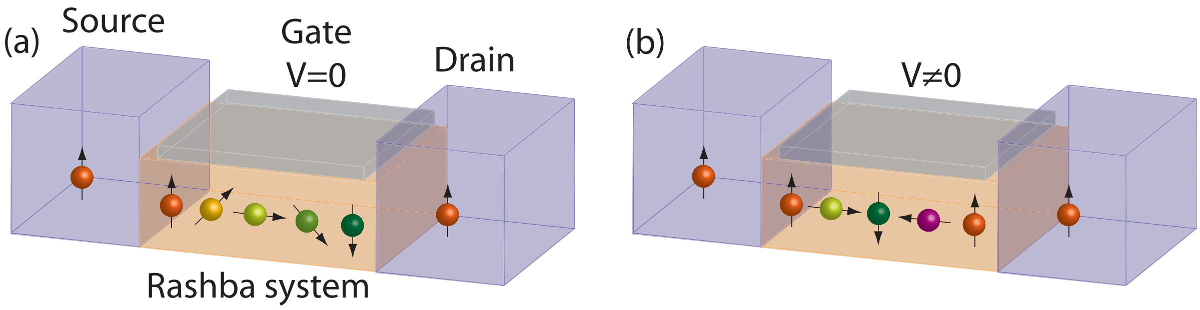

Figure 18: Schematic picture of the spin field-effect transistor in its (a) insulating and (b) conducting state.

An electron with its spin along e.g. the positive z axis can be represented by two spinors with spins along the y axis, i.e. $\left\langle z^{\uparrow}\right| = 1/\sqrt{2}\cdot\left(\left\langle y^{\uparrow}\right| + \left\langle y^{\downarrow}\right|\right)$, while an electron with spin along the negative z axis can be written as $\left\langle z^{\downarrow}\right| = 1/\sqrt{2}\cdot\left(\left\langle y^{\uparrow}\right| - \left\langle y^{\downarrow}\right|\right) = 1/\sqrt{2}\cdot\left(\left\langle y^{\uparrow}\right| + e^{i\pi}\left\langle y^{\downarrow}\right|\right)$. Similarly, a spin along x can be written as $\left\langle x^{\uparrow(\downarrow)}\right| = 1/\sqrt{2}\cdot\left(\left\langle y^{\uparrow}\right| + e^{i(3)\pi/2}\left\langle y^{\downarrow}\right|\right)$. Hence the sum $\left\langle y^{\uparrow}\right| + e^{i\varphi}\left\langle y^{\downarrow}\right|$ yields a spinor with its spin polarization in the xz plane, and the phase φ equals the angle measured from the positive x axis.

Let us now consider an electron at E_F moving along the positive x axis with its spinor along the positive z axis. In a Rashba system as schematically depicted in Fig. 17 (a) and Fig. 17 (b), such an electron is represented by the coherent superposition of states with positive momentum k_x and spinors along the positive and negative y axis as illustrated by the blue and red balls. Due to the momentum difference $2k_R$, a relative phase difference $\Delta\varphi = 2k_R L$ is accumulated between these two states as the electron moves a distance L along the x axis. In view of the discussion above, this relative phase difference causes a rotation of the spin in the xz plane as illustrated in Fig. 17 (c). A full rotation is achieved after the distance $L_R = \pi/k_R$. Correspondingly, the size of the momentum splitting determines the rotational length scale, where a larger splitting yields a smaller L_R. Due to the inverse behavior of L_R and k_R large Rashba-type spin splittings at the Fermi level are desirable since this can reduce the size of possible devices. For e.g. the $\mathrm{In}_x\mathrm{Ga}_{1-x}\mathrm{As}$ quantum well the momentum splitting k_R yields length scales L_R in the order of 1 μm.

Above it was shown how the peculiar band and spin structure of a Rashba system can cause spin rotation. A schematic picture of a spin field-effect transistor is given in Fig. 18. The source injects spin-polarized electrons, the Rashba systems manipulates the spin of the electrons and the drain preferentially accepts electrons of a certain spin. A gate voltage allows to change the size of the spin splitting and to switch between the insulating state (Fig. 18 (a)) and the conducting state (Fig. 18 (b)). Such a gate control of the Rashba-type spin orbit-coupling has been demonstrated in semiconductor heterostructures as discussed in section 3.2. However, in order to realize a spin field-effect transistor which functions at room temperature, several delicate issues regarding spin injection, manipulation and detection have to be resolved, [1, 2] whose description is beyond the scope of this section.

4 Microscopic picture of the Rashba effect

The Rashba-Bychkov model introduced in Chapter 3 describes many systems qualitatively remarkably well. The only material dependent parameters which enter the Rashba model and correspondingly the Rashba constant α_R are the value of the potential gradient perpendicular to the surface and the effective mass m^*. In this context, a simple intuitive picture describing the Rashba effect has been suggested. [99] It is based on the idea that the spin of the electrons, which move with a velocity $\boldsymbol{v}_{||} = \hbar\boldsymbol{k}_{||}/m^*$ within the interface (surface) plane perpendicular to the electric field $\boldsymbol{E}_\perp$ caused by the surface potential gradient $\boldsymbol{\nabla} V_\perp$, couples to the magnetic field $\boldsymbol{B}_{||}$ caused by the Lorentz transformation of the electric field $\boldsymbol{E}_\perp$ in the electrons rest frame. Considering typical values of $\boldsymbol{E}_\perp$ and $\boldsymbol{v}_{||}$, the obtained spin splitting is several orders of magnitude to small. [6,89,100] Now, how can the Rashba-type spin splitting be visualized more accurately? In the following two sections, it will be shown that the size of the Rashba constant α_R and hence the size of the spin splitting is an interplay between three physical properties: (*i*) the surface potential gradient, (*ii*) the electric field in the vicinity of the nuclei and (*iii*) the crystal structure.

4.1 The Rashba effect at the atomic level

An important ingredient which is missing in the standard Rashba model is the atomic nature of the solid, as pointed out by Petersen and Hedegard. [100] In their publication it was shown that both contributions from the surface potential gradient and from the atomic spin-orbit interaction enter the strength of the Rashba parameter. This can be understood directly if the surface state is described in the envelope function approximation, where the wave function is written as the product of an envelope function and a lattice periodic Bloch function. In this simple picture, the envelope functions "feels" the macroscopic environment (e.g. the potential gradient perpendicular to the surface) and the Bloch function "feels" the atomic fields. [89] The electric field $\boldsymbol{E}_\perp = \boldsymbol{\nabla} V_\perp$ perpendicular to the surface is needed to break the symmetry and gives a measure of the asymmetry, which is then weighted with the atomic spin-orbit interaction. In general both a larger $\boldsymbol{E}_\perp$ and a larger atomic number Z will lead to a stronger Rashba-type spin splitting. [100,101]

In semiconductor heterostructures the electric field perpendicular to the Rashba system can be changed by the application of so-called gate voltages as shown in section 3.2. It was shown by Nitta et al. [90] that this indeed allows to control the size of the Rashba-type spin splitting in semiconductor heterostructures. For surface states on the other hand, the electric field perpendicular to the surface is essentially determined by the work

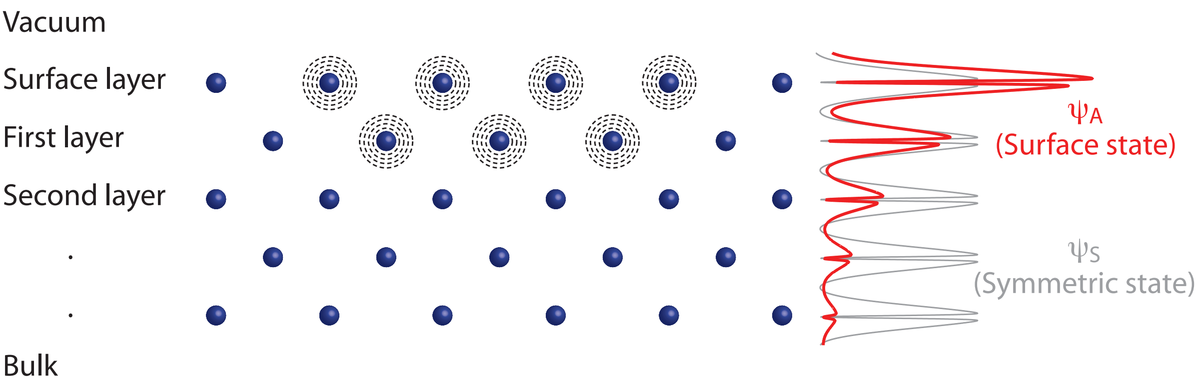

Figure 19: Qualitative sketch for the Rashba model given in Ref. [101]. The blue dots represent the atoms, the dotted circular lines are the lines of constant atomic fields. The grey wave function represents a bulk state and the red one a surface state. The presence of the surface lifts the symmetry of the wave function and the related potential gradient creates a phase shift.

function and the Fermi wave length, hence no significant differences in the electric field perpendicular to the surface can be expected for the surface states considered in this thesis. [100, 102] Correspondingly, there is more to the Rashba-type spin splitting than just the surface (interface) potential gradient.

In Fig. 19 we schematically present a model, as developed by Bihlmayer et al. [101], which both qualitatively and quantitatively manages to explain the Rashba-type spin splitting found in surface states (as well as semiconductor heterostructures). The main result of this model is that the Rashba-type spin splitting is essentially determined by the asymmetry of wave functions in the vicinity of the nuclei. As such, the model accounts for the crystal structure. In the region close to the individual nuclei, the spin-orbit coupling Hamiltonian given in Eq. 28 can be modified to

$$H_{SOI} = -\frac{i\hbar^2}{2m^2}\frac{1}{r}\frac{\partial V}{\partial r}(\boldsymbol{r} \times \boldsymbol{\nabla}\ ) \cdot \boldsymbol{\sigma}, \tag{37}$$

where $r = |\boldsymbol{r}|$ and V is the spherically symmetric potential of the nucleus. Only the $l = 0$ term of the expansion is taken into account, which is justified in the vicinity of the nuclei, where the potential is almost radially symmetric, and V=0 is assumed for $r > R$. From Eq. 37 it is evident that the strength of the spin splitting depends on the atomic number Z, since the potential V of the nucleus scales with Z. This dependency explains the general trend that the Rashba-type spin splitting is larger in systems with heavy atoms, as exemplified in Table 1 for Ag(111), Au(111) and Bi(111).

For a symmetric (antisymmetric) wave function $\psi_S(\boldsymbol{r})$ with respect to the nuclei, as schematically illustrated by the grey line in Fig. 19, H_{SOI} induces no spin splitting due

System	Z	k_0 (Å^{-1})	E_R (meV)	α_R (eVÅ)	Ref.
Ag(111)	47	0.0007	0.005	0.013	[103, 104]
Au(111)	79	0.012	2.1	0.33	[6, 104]
Bi(111)	83	0.05	14	0.56	[12]

Table 1: Characteristic parameters for the spin-split surface states of Ag(111), Au(111) and Bi(111). All parameters increase with increasing atomic number Z.

to symmetry. This is because when $\psi_S(\boldsymbol{r}) = \pm\psi_S(-\boldsymbol{r})$, then $\tilde{\psi}_S(\boldsymbol{r}) := H_{SOI}\psi_S(\boldsymbol{r}) = \mp\tilde{\psi}_S(-\boldsymbol{r})$. Hence $\psi_S^*\tilde{\psi}_S(\boldsymbol{r}) = -\psi_S^*\tilde{\psi}_S(-\boldsymbol{r})$ and correspondingly the integral $\langle\psi_S|H_{SOI}|\psi_S\rangle = \int_{|\boldsymbol{r}|<R} d\boldsymbol{r}\ \psi_S^*\tilde{\psi}_S = 0$. This means that for a hypothetical surface state with e.g. purely s, p or d character, there is no Rashba-type spin splitting.

However, if the wave function is asymmetric with respect to the nuclei the interaction with H_{SOI} in general yields a finite value. For a surface state the symmetry of the wave function is lifted due to the asymmetric potential introduced by the surface. The corresponding asymmetric wave function ψ_A is confined to the surface region and decays exponentially towards the vacuum and the bulk as schematically shown by the red line in Fig. 19. The surface state wave function ψ_A can be approximated as a product of an envelope function describing the exponential decay away from the surface and a Bloch function. The role of the asymmetric potential induced by the surface, or more specifically of the surface potential gradient in Eq. 28, is the creation of an asymmetric envelope function, where in general a larger asymmetry in the potential will yield a larger asymmetry in the envelope function. Correspondingly the multiplication of the envelope function with the Bloch part creates a wave function which is asymmetric in the region of the nuclei. It is precisely this asymmetry with respect to the nuclei which causes a finite Rashba effect. In this respect, the entire surface state wave function contributes to the Rashba effect. Considering the Au(111) surface state, it was actually shown that more than 40 percent of the size of the Rashba effect are caused in the subsurface layers, where the screening of the surface potential gradient should be efficient. [101] This clearly indicates that it is the asymmetry of the wave function which causes the Rashba effect rather than the surface potential gradient itself. More precisely, it is the derivative of the envelope function which determines both the size and the sign of the Rashba effect. Regarding the orbital character, the asymmetry is represented by the mixture of different orbitals, e.g. p- and d-type orbitals.

4.1.1 Example: Rashba-type spin splitting of quantum well states in ultra-thin Pb films

The Rashba-type spin splitting of quantum well states (QWS) in ultrathin metal films on Si(111)($\sqrt{3}\times\sqrt{3}$)$R30°$:Pb gives a nice example of the Rashba effect on the microscopic scale and is here used to illustrate the model introduced above. [83,105] The QWS which form in these metal films are confined in an asymmetric potential since on one side it is constituted by the interface between the metal and the substrate while on the other side it is constituted by the metal-vacuum interface. This is in contrast to a surface state for which the only asymmetry is due to the surface. Parallel to the interfaces the QWS show a free electron-like dispersion as shown in Fig. 20 (a).

If the confinement potential is symmetric, then the absolute value of the wave function of the QWS will look like in Fig. 21 (a) (here shown for the case where the quantum number is $n = 1$). The wave function is symmetric with respect to the center of the confinement potential for an arbitrary quantum number n. However, the wave function is asymmetric with respect to most Pb layers and correspondingly most layers have a finite contribution to the Rashba effect even in the symmetric case. But since the wave function is symmetric with respect to the center of the confinement potential the contributions from the

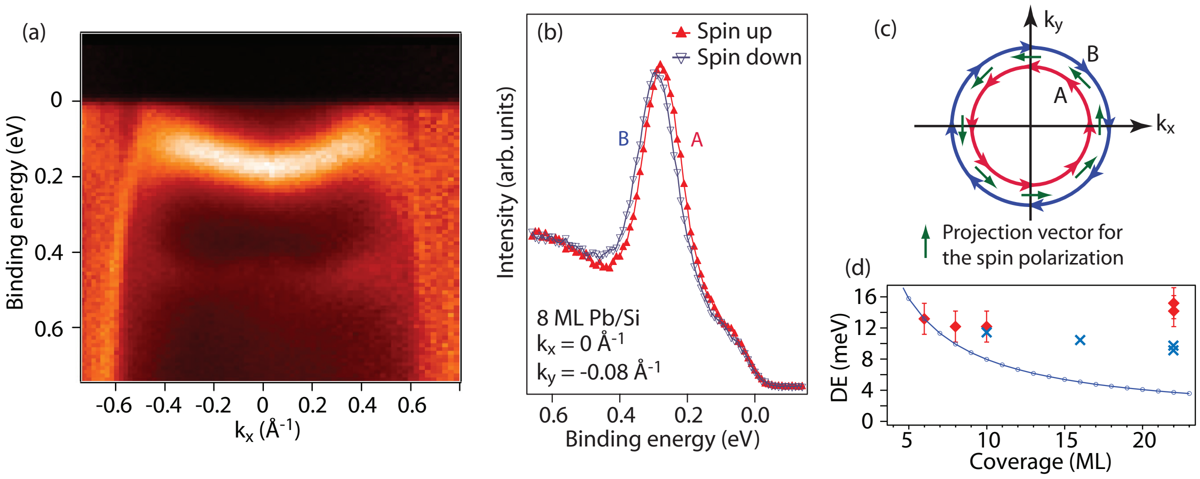

Figure 20: (a) Measured spin-integrated ARPES data for a 10 ML thick Pb film on Si(111)($\sqrt{3}\times\sqrt{3}$)$R30°$:Pb. (b) Spin-resolved intensity distribution curves. (c) Schematic representation of a constant energy surface where the arrows of band A and B refer to the direction of the spin polarization axis. (d) Measured (red diamonds) and calculated (blue crosses) spin splitting as a function of coverage at $k_y = 0.08$ Å^{-1} and $k_x = 0$, the blue circles show the intuitively expected 1/thickness dependency.

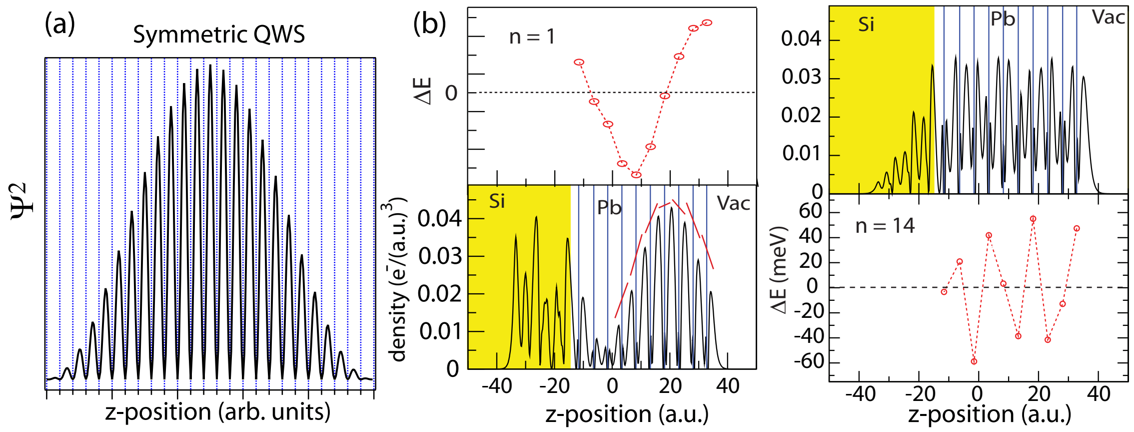

Figure 21: (a) Wave function distribution for a symmetric quantum well state with quantum number $n = 1$. (b) Wave function distribution calculated for $n = 1$ and 14 QWS in Pb on Si(111)($\sqrt{3} \times \sqrt{3}$)$R30°$:Pb at $k = 0.1\bar{\Gamma}\bar{K}$ and the local Rashba effect at each layer. The blue lines indicate the position of the atomic planes. (from Ref. [105])

different layers add up to zero, because for every finite contribution there is the opposite contribution on the other side of the center of the confinement potential. Hence there is no net Rashba-type spin splitting for a QWS confined in a symmetric potential. This situation changes when the confinement potential is non-symmetric. Due to the finite and asymmetric confinement potential, the QWS formed in the Pb film penetrates to different extents into the vacuum and the Si(111) substrate and correspondingly experiences different phase shifts at the two interfaces. As a consequence of this different penetration into the boundaries, the symmetry of the QWS wave function with respect to the center of the confinement potential is lifted and the sum of the contributions from the different Pb layers will in general yield a finite value. As a result, there will be a finite Rashba-type spin splitting.

The above considerations are illustrated in Fig. 21 (b) for a QWS with quantum number $n = 1$ (left side) and $n = 14$ (right side), where the QWS wave function and the local contribution from each layer are shown. The local contribution from one specific layer to the Rashba effect is calculated by turning the spin-orbit coupling off at all other layers. Since the spin-orbit coupling influences the shape of the wave function, this local contribution is most likely not very precise. Hence the sum of the contributions obtained in this manner does not yield the same Rashba effect as found when considering the full system. Nevertheless, both the asymmetric wave function and oscillations in the local contribution to the Rashba effect become obvious. By comparing the derivative of the envelope function for $n = 1$ (red lines in the lower panel) with the contribution from each layer, it is obvious that both the sign and the magnitude are determined by the derivative of the envelope function in the region of the layers, as discussed above.

The experimental observation of the spin splitting by SARPES is shown in Fig. 20 (b). The Rashba constant for a 10 ML thick film was found to be $|\alpha_R| = 0.04$ eV Å and the momentum offset is given by $k_R = 0.035$ Å^{-1}. [83] The spin splitting at $\boldsymbol{k}_{||} \approx 0.1$ Å^{-1} is in the order of 10-20 meV for an arbitrary layer thickness.

The small size of the spin splitting found in the QWS for Pb on $(\sqrt{3} \times \sqrt{3})R30°$:Pb, compared to the spin splitting found in the surface states on heavy metals can be explained by considering Fig. 19 and Fig. 21. For a surface state, the gradient of the envelope function has the same sign at each layer and correspondingly all contributions add up, which is in contrast to the QWS, where the local contributions partially cancel. Moreover, for a surface state most electrons are located close to the surface, where the derivative of the surface state envelope function is large. In the QWS, exactly the opposite is the case and whenever the absolute value of the QWS wave function is large, the derivative of the envelope function is small. These significant differences between the Rashba effect for a surface state and a QWS are essentially a result of competing effects at the two interfaces. It should here again be noted that although the interfaces in that sense determine the Rashba effect, it occurs throughout the whole Pb layer (and to some extent in the substrate). The origin of the Rashba effect in a QWS makes it possible that the spin splitting shows no significant dependency on the number of Pb layers (and correspondingly on the quantum number n), as shown in Fig. 20 (c).

At last it should be pointed out that in the specific case of QWSs in Pb on $(\sqrt{3} \times \sqrt{3})R30°$:Pb the spin chirality is negative, i.e. the spin chirality is reversed compared to e.g. the surface state of Au(111), which implies $\alpha_R < 0$. This is an indication that the net shift is towards the Si interface. In other words the QWS wave function accumulates a larger phase shift at the Pb/Si interface compared to the Pb/vacuum interface. In this context, it seems feasible to tune both the size of the spin splitting and the spin chirality of QWSs by altering the properties of the interfaces.

4.2 Influence of the crystal structure on the Rashba-type spin-orbit splitting

In section 4.1 a qualitative model which explains the Rashba effect in terms of an asymmetric envelope function was introduced. In this section it will be shown that the atomic structure in the surface and near surface region is another important ingredient to the Rashba-type spin splitting. While in subsection 6 it will be shown that the surface structure is of key importance for the surface alloys on Ag(111), here the importance of the crystal structure for the case of Sb(111) will be illustrated as already discussed in

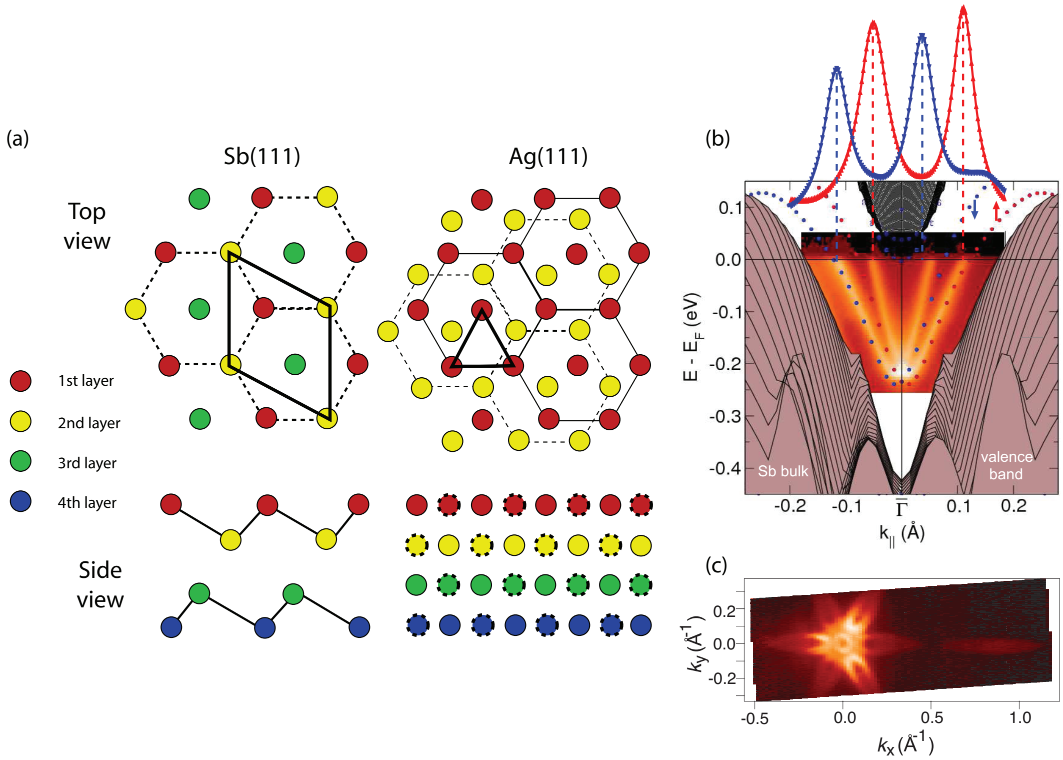

Figure 22: (a) Truncated crystal structure of rhombohedral Sb(111) and cubic Ag(111). The different colours indicate different layers and the different borders for Ag(111) indicate different locations in the perpendicular direction within this layer. The atom distances of Sb and Ag are not to scale. (b) Spin-integrated ARPES band map of Sb(111) along the $\bar{\Gamma}\bar{M}$ direction, and spin-resolved MDC of Sb(111) at the Fermi energy projected perpendicular to the measurement direction. The shaded area and dotted lines are obtained from DFT calculations and represent the Sb(111) bulk and surface states, respectively. (c) Fermi surface map of Sb(111). (adapted from Refs. [21] and [105])

Ref. [105].

Sb crystallizes like Bi in a rhombohedral structure typical for the group V semimetals. The structure of the first four layers of Sb(111) is shown in Fig. 22 (a) and compared to Ag(111), which crystallizes in a *fcc* structure. The atomic number of Sb is $Z = 51$, which is close to the atomic number of Ag ($Z = 47$), but well below the one of Au ($Z = 79$). Up to date, no spin splitting could be observed experimentally for the Ag(111) surface state due to its small size. Calculations estimating the size of the spin splitting of the Ag(111) surface state yield a momentum splitting $k_R = 0.0007$ Å^{-1}. [106] Considering the atomic number of Sb and Ag and that there is no reason for a significant difference in the surface potential gradient, one would assume that the spin splitting of Sb(111) should be very small as well. Fig. 22 (b) shows that this is not the case. The red and

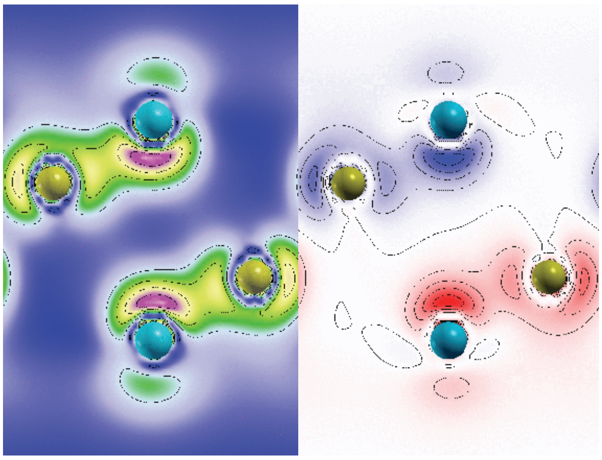

Figure 23: Charge density (left) and spin density (right) plots of the surface-like state of the stacked double bilayer system Bi-Sb-Sb-Bi for $\boldsymbol{k}_{||} = 0.08\ \bar{\Gamma}\bar{M}$. The Sb atoms are shown in light blue and the Bi atoms in yellow. In the spin density plot, red and blue indicate positive and negative values, respectively. (from Ref. [107])

blue curves are the spin-resolved MDC data which prove the Rashba-type nature of the Sb(111) surface state. [21]

The momentum splitting which can be deduced from the shift of the band apex away from the $\bar{\Gamma}$ point is $k_R = 0.015$ Å^{-1}. As can be seen from Fig. 22 (b), the dispersion of the Sb(111) surface state is not perfectly parabolic and the momentum splitting at the Fermi level is increased to $\Delta k \approx 0.073$ Å^{-1}. For larger $\boldsymbol{k}_{||}$ values the dispersion of the Sb(111) surface state is actually highly anisotropic and reveals a topologically non-trivial structure as represented in the Fermi surface shown in Fig. 22 (c). [21] The value k_R for the surface state of Sb(111) is more than 20 times larger than the one for the surface state of Ag(111), and it even exceeds the value found for the Au(111) surface state, where $k_R = 0.012$ Å^{-1}. [6]

The top views of Sb(111) and Ag(111) given in Fig. 22 (a) show a similar hexagonal structure for both systems, while the side views reveal the dramatic difference between the Sb(111) and the Ag(111) crystal. Considering the side view of Sb(111), two aspects are of particular importance. One is the fact that Sb(111) shows a bilayer-type structure with alternating interlayer spacing. The other is that the atom positions of the layer i are asymmetric with respect to the layer $i + 1$ and correspondingly there is no mirror symmetry for the side view of Sb(111) presented in Fig. 22 (a). As a consequence, the wave function of the surface state in Sb(111) is highly asymmetric around the nuclei, which leads to a larger Rashba-type spin splitting according to the model introduced in section 4.1. The asymmetric charge distribution of the surface state around the atoms is illustrated in Ref. [107] for different Bi-Sb alloys, which also crystallize in a

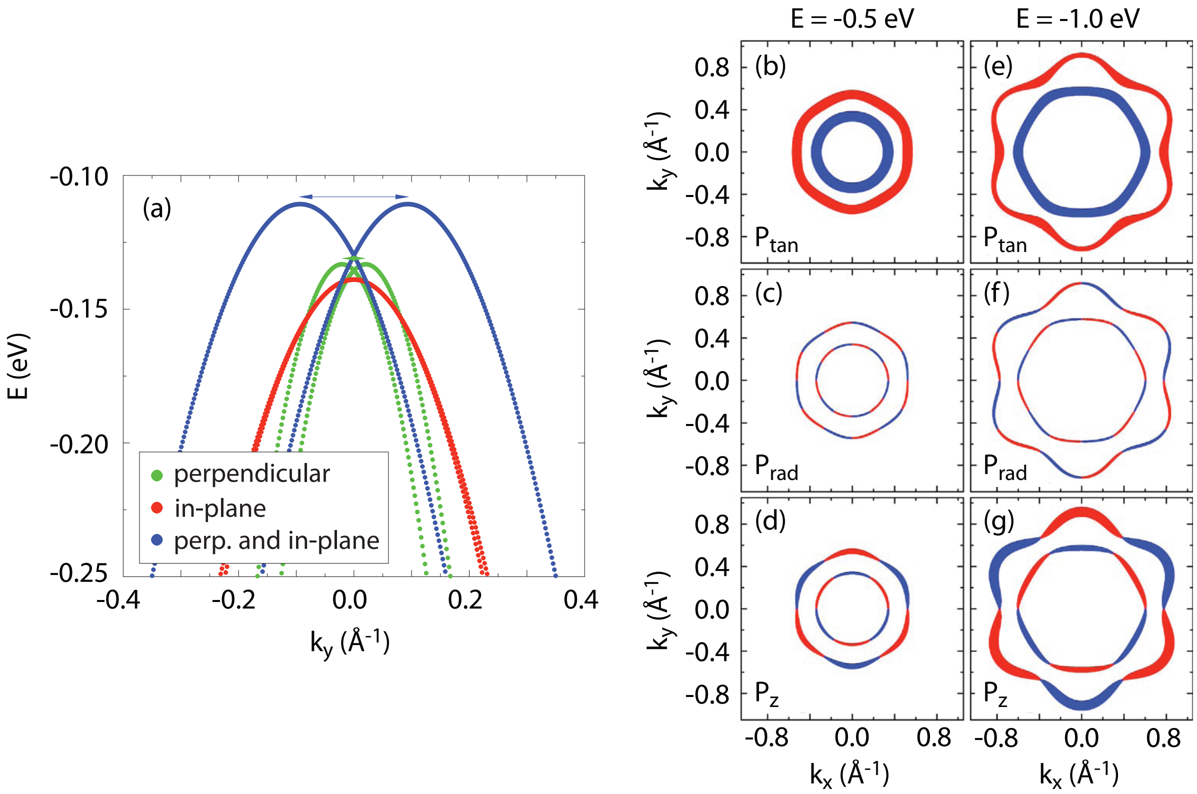

Figure 24: (a) Effect of both in-plane and perpendicular structural inversion asymmetries on the dispersion in a two-dimensional electron gas, where k_y is perpendicular to a mirror plane. The colors indicate the spin-orbit contributions: green is for perpendicular SIAs only, red is for in-plane SIA only, and blue is for perpendicular and in-plane SIAs. The horizontal arrows near the respective band maxima mark the spin-orbit splitting $2k_R$. (b)-(g) Spin-resolved momentum distributions of an anisotropic two-dimensional electron gas at $E = -0.5$ eV (left column) and $E = -1.0$ eV (right column). The symbol sizes indicate the moduli of spin-polarization components P_{tan} [top row, panels (b) and (e)], P_{rad} [center row, panels (c) and (f)], and P_z [bottom row, panels (d) and (g)]. They are comparable within this figure. Blue and red symbols are for negative and positive values, respectively. (adapted from Ref. [108])

rhombohedral structure. Fig. 23 shows the charge and spin density for the case of the stacked double bilayer system Bi-Sb-Sb-Bi at $\boldsymbol{k}_{||} = 0.08\ \bar{\Gamma}\bar{M}$, calculated using density functional theory (DFT). The charge density is maximal at approximately the center of each bilayer, yielding a highly asymmetric distribution with respect to the individual atoms. The spin density plot reveals the highly spin-polarized nature of the states.

The example of the comparably large Rashba-type spin splitting observed for the surface state of Sb(111) clearly shows that the size of the spin splitting is strongly influenced by the crystal structure. Of particular importance are the in-plane symmetries of the crystal structure, as pointed out by Premper et al. [108]. In their publication, they discuss the influence of an in-plane structure inversion asymmetry on the spin-orbit splitting of a 2D electron gas (2DEG). The breaking of the in-plane SIA results in an anisotropic in-plane component of the potential gradient. The results of calculations considering a 2DEG with in-plane SIA are shown in Fig. 24 (a), where a hexagonal lattice with point group $3m$ accounting for the in-plane SIA was assumed. The green curve corresponds to the case where the only SIA is perpendicular to the surface, where a notable spin splitting can be seen. In the case of solely an in-plane SIA, the size of the spin splitting is small (red curve). If however the SIA is considered both perpendicular to the surface plane and within the surface plane, the spin splitting is significantly enlarged (blue curve in Fig. 24 (a)). The effect of the in-plane SIA can also be understood in terms of the wave function. While a SIA perpendicular to the surface causes an asymmetry with respect to the nuclei in the direction perpendicular to the surface, the in-plane SIA additionally creates an asymmetry with respect to the nuclei in the surface plane.

As shown in Fig. 24 (b)-(g), the in-plane asymmetry has profound consequences for the direction of the spin polarization vectors and the shape of the constant energy contours, which deviate from a circular shape due to the anisotropic potential. For an isotropic 2DEG, the spin polarization vector is in-plane and perpendicular to the momentum $\boldsymbol{k}_{||}$. For a anisotropic 2DEG however, the spin polarization shows a finite radial component P_{rad} and a finite out-of-plane component P_z for most momenta $\boldsymbol{k}_{||}$. The absolute value of these two components increase with increasing $k_{||} = |\boldsymbol{k}_{||}|$, or equivalently increasing binding energy, due to the larger influence of the crystal lattice towards the SBZ boundaries. This is shown in Fig. 24 (b)-(d) and Fig. 24 (e)-(g) for the $E = -0.5$ eV and $E = -1.0$ eV, respectively. From Fig. 24 (c) and (f) it seems that the in-plane part of the spin polarization vector is tangential to the constant energy contour and in that sense orthogonal to the group velocity rather than orthogonal to the momentum. The finite out-of-plane spin polarization component due to asymmetric in-plane potential gradients can easily be understood even within Eq. 28, where the spin polarization is perpendicular to the momentum and the potential gradient. Correspondingly an in-plane potential gradient yields a finite P_z component.

5 Crystal structure of the (Bi/Pb/Sb)/Ag(111) surface alloys

The family of surface alloys Bi/Ag(111)($\sqrt{3}\times\sqrt{3}$)$R30°$, Pb/Ag(111)($\sqrt{3}\times\sqrt{3}$)$R30°$ and Sb/Ag(111)($\sqrt{3}\times\sqrt{3}$)$R30°$, henceforth (Bi/Pb/Sb)/Ag(111) respectively, have received a lot of attention since the discovery of the giant Rashba-type spin splitting in Bi/Ag(111). [102] Moreover, in this family of surface alloys, the mixture of the different alloy atoms Bi, Pb and Sb even allows for a full tunability of both the Fermi level and the spin splitting, opening up fascinating possibilities for the investigation of spin-orbit coupling related effects and device applications. [109] In this chapter the structural properties of these surface alloys will be introduced, while the mechanisms responsible for the giant spin splitting and the adjustability of both the Fermi level and the spin splitting will be discussed in chapters 6 and 7. Parts of the current chapter have been published in Ref. [110].

5.1 Sample preparation

The sample preparation of the surface alloys was carried out *in situ* under ultrahigh vacuum conditions ($p < 10^{-9}$). The Ag(111) crystal was cleaned by multiple cycles of Ar^+ sputtering and annealing. Each cycle consisted of 20 min sputtering at an acceleration voltage $V = 0.5$ kV, and for the annealing the temperature was subsequently increased to $T \approx 300°$ C, where it was kept for ten minutes. The cleanliness of the Ag(111) crystal was confirmed by the observation of the L-Gap surface state by ARPES. For the pure surface alloys Bi/Ag(111), Pb/Ag(111) and Sb/Ag(111), a third of a monolayer of the respective material was deposited from either a calibrated electron beam evaporator (acceleration voltage V usually between $600 - 800$ V) or a calibrated Knudsen cell, with the sample held at 100° C, followed by a post-annealing to 250° C. The post-annealing considerably increases the sharpness of the LEED spots and the surface state band structure formed by the surface alloys. The samples prepared with the electron beam evaporator were of better quality compared to those prepared with the Knudsen cell, presumably due to the lower pressure during evaporation when using the electron beam evaporator. For the preparation of the mixed binary surface alloys $\mathrm{Bi}_x\mathrm{Pb}_{1-x}$/Ag(111) and $\mathrm{Bi}_x\mathrm{Sb}_{1-x}$/Ag(111), the respective materials were simultaneously deposited from the electron beam evaporator with the sample held at $T \approx 200°$ C, with the total amount corresponding to 1/3 of a monolayer. For the ternary surface alloy $\mathrm{Bi}_x\mathrm{Pb}_y\mathrm{Sb}_{1-x-y}$/Ag(111), Sb was evaporated first with the sample at 200° C, then Bi and Pb were simultaneously deposited. The sample quality was confirmed by low energy electron diffraction (LEED) and ARPES. The evaporation rate was around one monolayer in ten minutes. Surprisingly, the surface state band structure remains almost invisible until the coverage reaches 1/3 of a monolayer. For slightly higher coverages, a broadening of the surface state band structure could be observed, but no additional bands.

5.2 Structure determination by quantitative LEED analysis

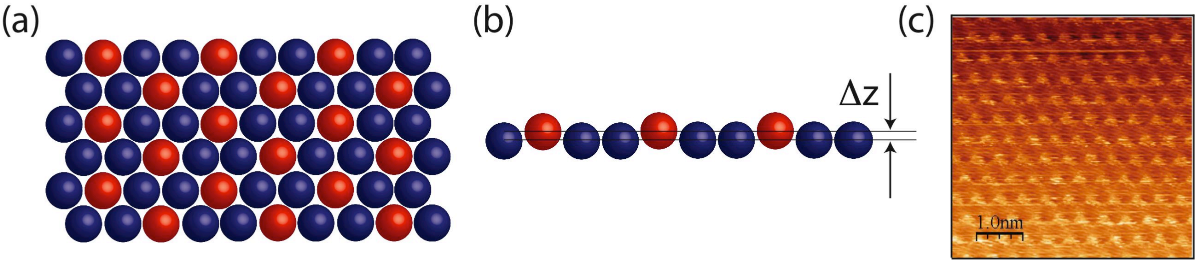

Figure 25: (a) Top view and (b) side view of the $(\sqrt{3} \times \sqrt{3})R30°$ structure formed by the surface alloys on Ag(111). The alloy atoms are shown in red and the Ag atoms in blue. Δz is the outward relaxation of the alloy atoms, defined as the vertical distance between the alloy atoms and the Ag atoms in the topmost layer. (c) Scanning tunneling microscope image of Bi/Ag(111) where the Bi atoms are resolved.

In Fig. 25 the real space structure of the surface alloys on Ag(111) is shown in a top view (Fig. 25 (a)) and a side view (Fig. 25 (b)). The alloy atoms, in our case Bi, Pb and Sb, are shown in red while the Ag atoms are colored in blue. The deposition of 1/3 of a monolayer of these alloy atoms leads to a well ordered $(\sqrt{3} \times \sqrt{3})R30°$ reconstruction of the Ag(111) surface. In that respect, the term alloy may be confusing, because it usually refers to disordered systems. Due to the size mismatch of the alloy atoms and the Ag atoms, the alloy atoms show an outward relaxation Δz, which is defined as the distance along the surface normal between the alloy atoms and the Ag atoms in the topmost layer. Taking the Ag substrate into account, the surface alloys have a threefold rotational symmetry. Consequently, the system is in-plane inversion asymmetric. Both the outward relaxation Δz and the in-plane SIA have a profound consequence for the size of the Rashba-type spin splitting of the surface alloys, as will be experimentally shown in chapter 6. Fig. 25 (c) shows a topographic scan of the long-range ordered hexagonal Bi/Ag(111) surface alloy taken by STM, where the Bi alloy atoms are resolved. The lattice constant is 5 Å.

Fig. 26 (a) shows the surface Brillouin zones (SBZs) for the Ag(111) substrate (blue) and the surface alloy X/Ag(111) (red), where X = Bi/Pb/Sb. The Brillouin zones of the substrate and the superlattice are rotated by 30° with respect to each other. The momenta $\bar{\Gamma}$, $\bar{M}$ and $\bar{K}$ are points of high symmetry. The dashed lines represent

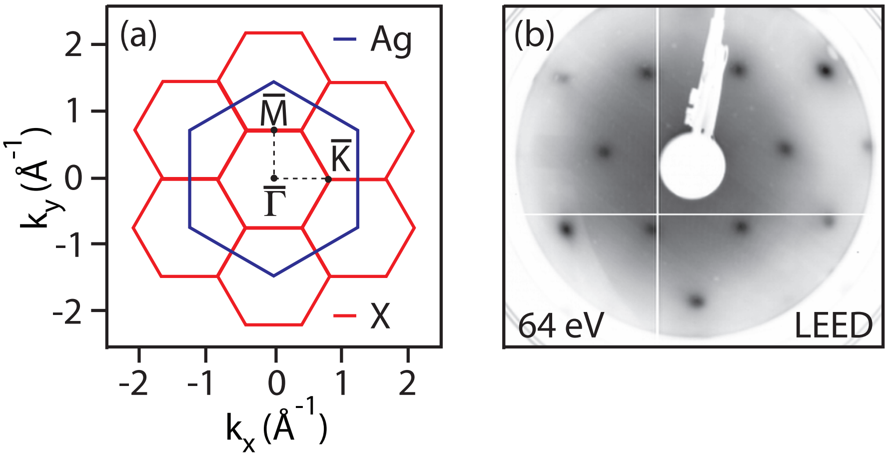

Figure 26: (a) Hexagonal surface Brillouin zones of the Ag(111) substrate (blue) and the superlattice (red) due to the surface alloying by X = Bi/Pb/Sb. (b) LEED image for Pb/Ag(111) taken at an electron energy of 64 eV. The horizontal and vertical white lines are an artifact of the camera.

the high symmetry directions $\bar{\Gamma}\bar{M}$ and $\bar{\Gamma}\bar{K}$. The structure is mirror symmetric with respect to $\bar{\Gamma}\bar{M}$. This mirror symmetry has to hold for both the band structure and the spin structure. The $\bar{\Gamma}$ and the $\bar{M}$ points are so-called time reversal invariant momenta (TRIM). At a TRIM $\boldsymbol{k}_T$, the combination of translational symmetry by a reciprocal lattice vector $\boldsymbol{G}$ and time reversal symmetry implies

$$E(\boldsymbol{k}_T, \downarrow) = E(-\boldsymbol{k}_T, \uparrow) = E(-\boldsymbol{k}_T + \boldsymbol{G}, \uparrow) = E(\boldsymbol{k}_T, \uparrow). \tag{38}$$

This means that electronic states located at a TRIM are forced to be degenerate by symmetry which is in contrast to other high symmetry points. The degeneracy at the TRIMs is of particular importance for a new phase of matter, the topological insulators. [17, 19–21, 111]

In order to determine the outward relaxation Δz of the alloy atoms, we have carried out quantitative low energy electron diffraction measurements [112], also called IV-LEED, measurements for the three pure surface alloys Bi/Ag(111), Pb/Ag(111) and Sb/Ag(111), as well as for the mixed surface alloy Bi$_x$Sb$_{1-x}$/Ag(111). An example of a typical LEED pattern showing the $(\sqrt{3}\times\sqrt{3})R30°$ reconstruction is given in Fig. 26 (b) for Pb/Ag(111) and an electron energy of 64 eV. In IV-LEED, the integrated intensity of a particular LEED spot (i.e. the electron current I_{el} of that spot) is measured as a function of the kinetic energy of the incoming electron beam. The curves obtained in this manner can then be compared to simulations in order to determine the surface structure, where the Pendry factor R_P gives a measure for the agreement between experiment and theory. [113] In general one speaks of good agreement between theory and experiment if $R_p < 0.25$.

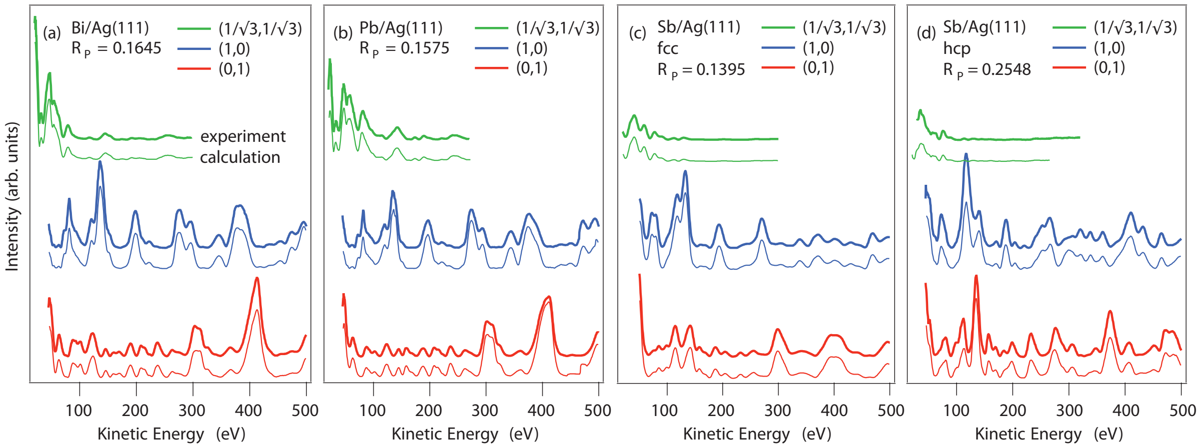

Figure 27: IV-LEED data (thick lines) for the $(\sqrt{3} \times \sqrt{3})R30°$ phases of (a) Bi, (b) Pb, (c) and (d) Sb on Ag(111). The thin lines are the corresponding calculated IV-LEED spectra. Sb/Ag(111) can be formed in both *fcc* and *hcp* phases, while Bi/Ag(111) and Pb/Ag(111) are always formed in a *fcc* phase. (adapted from Ref. [110])

The error bars of the parameters used in the IV-LEED simulations can be estimated using the double reliability factor RR as described in Ref. [113].

In Fig. 27 the integrated intensity of the three equivalent $(0,1)$ and $(1,0)$ as well as of the six equivalent $(1/\sqrt{3}, 1/\sqrt{3})$ spots are shown as a function of electron energy for the three surface alloys Bi/Ag(111), Pb/Ag(111) and Sb/Ag(111). The experimental data (thick lines in Fig. 27) are averaged over the three (six) equivalent spots and smoothed. The IV-LEED spectra for Bi/Ag(111) and Pb/Ag(111) shown in Fig. 27 (a) and (b), respectively, are qualitatively similar and only differ in detail. Hence the experimental curves indicate that both systems form the same $(\sqrt{3} \times \sqrt{3})R30°$ phase. A comparison to the calculated spectra (thin lines in Fig. 27) reveals that both Bi and Pb on Ag(111) form an un-faulted face centered cubic (*fcc*) substitutional alloy. Calculations using a faulted hexagonal close packed (*hcp*) structure show much larger (about a factor of two) reliability factors R_P. In contrast to Bi/Ag(111) and Pb/Ag(111), for Sb/Ag(111) two phases which differ in the top layer stacking are known from literature. [114, 115] One phase grows in regular *fcc* stacking and the other phase in *hcp* stacking. The IV-LEED data for the two different phases of Sb/Ag(111) are shown in Fig. 27 (c) and (d). The R_P factor of the *hcp* phase for Sb/Ag(111) is slightly larger, which is attributed to some *fcc* domains being present at the surface, while for the *fcc* phases of the three surface alloys the agreement between theory and experiment is very good.

During the IV-LEED experiments presented here it was found that it is possible to reproducibly create the two phases of Sb/Ag(111). This is in contrast to earlier reports, where it was speculated that the *hcp* top layer stacking is a consequence of subsurface

	$\mathbf{\Delta z}$ **(Å)**	$\mathbf{d_{12}}$ **(Å)**	$\mathbf{d_{23}}$ **(Å)**	$\mathbf{d_{34}}$ **(Å)**	**Ref**
Bi/Ag(111)	0.65 ± 0.10	2.32 ± 0.02	2.33 ± 0.03	2.34 ± 0.04	[110]
Substitutional	0.35 (theory)				[102]
	0.85 (theory)				[87]
Pb/Ag(111)	0.46 ± 0.06	2.35 ± 0.02	2.33 ± 0.03	2.34 ± 0.04	[110]
Substitutional	0.48 ± 0.02 (SXRD)				[116]
	0.8 ± 0.1 (STM)				[116]
	0.68 (theory)				[116]
	0.42 (theory)				[109]
	0.97 (theory)				[87]
Sb/Ag(111)	0.11 ± 0.05	2.43 ± 0.05	2.34 ± 0.05	2.35 ± 0.06	[110]
hcp substitutional	0.03 ± 0.07 (SXRD)	2.50 ± 0.03			[117]
	0.02 (theory)	2.47	2.34		[114]
	0.07 ± 0.04 (IV-LEED)	2.46 ± 0.03	2.34 ± 0.04	2.42 ± 0.07	[118]
Sb/Ag(111)	0.10 ± 0.02	2.44 ± 0.02	2.33 ± 0.02	2.33 ± 0.03	[110]
Substitutional	0.24 (theory)				[119]
Bi/Cu(111)	1.02 ± 0.02 (SXRD)	2.11 ± 0.01	2.00 ± 0.01		[120]
Substitutional	1.06 (theory)				[24]
Sb/Cu(111)	0.47 ± 0.16 (MEIS)	2.05 ± 0.09			[121]
hcp substitutional	0.6 ± 0.03 (SXRD)	1.98 ± 0.02			[117]
	0.47 (theory)	2.09	2.07		[114]

Table 2: Geometrical parameters of the different surface alloys on Ag(111) and Cu(111) substrates. The outward relaxation Δz is the distance between the alloy atom and the plane of the surface layer. The distances $\mathbf{d_{12}}$, $\mathbf{d_{23}}$, and $\mathbf{d_{34}}$ are the distances between the first (= surface) and second layer, the second and third layer, as well as the third and fourth layer, respectively. The bulk interlayer distances are 2.36 Å for Ag(111) and 2.09 Å for Cu(111). (adapted from Ref. [110])

stacking faults from previous preparations caused by Sb atom diffusion into the bulk. [114] Our explanation for this finding is as follows. If an ion beam evaporator is used, then the atom beam is partially ionized by the electrons from the filament, and the ionized atoms are accelerated by a positive voltage at the crucible towards the grounded sample. If now this voltage is large, then the Sb ions have a higher kinetic energy and correspondingly a stronger impact at the Ag(111) surface. It was found that for voltages larger than +370 V, the *hcp* stacking is formed, while for voltages below +370 V as well as for thermal atoms evaporated from a Knudsen cell, the *fcc* stacking is formed. It is conceivable that a higher kinetic energy of the Sb ions can cause ion implantation into the

Ag substrate which induce the subsurface stacking faults that favor the $(\sqrt{3} \times \sqrt{3})R30^\circ$ phase with *hcp* stacking.

The structural parameters resulting from the fit of the theoretical data to the experimental IV-LEED data for the pure surface alloys on Ag(111) are summarized in Table 2 and compared to the results obtained by other experimental methods, i.e. surface x-ray diffraction (SXRD), medium energy ion scattering and scanning tunneling spectroscopy (STM) as well as by theory. In addition, the corrugation of the $(\sqrt{3} \times \sqrt{3})R30^\circ$ phases of Bi and Sb on Cu(111) are given. Δz denotes the outward relaxation of the alloy atoms, while $\mathbf{d_{12}}$, $\mathbf{d_{23}}$ and $\mathbf{d_{34}}$ are the differences between different layers, where 1 corresponds to the first (surface) layer of Ag atoms, 2 to the second layer and 3 to the third layer.

As can be expected from the size of the different alloy atoms, Bi shows the largest outward relaxation $\Delta z = 0.65 \pm 0.10$ Å, while the surface of the Pb/Ag(111) surface alloy still shows a notable corrugation ($\Delta z = 0.46 \pm 0.02$ Å). The surface of the Sb/Ag(111) surface alloy shows a much smaller corrugation, which is $\Delta z = 0.10 \pm 0.02$ Å in the *fcc* structure and $\Delta z = 0.11 \pm 0.05$ Å in the *hcp* structure. Our results for Pb and Sb on Ag(111) are in very good agreement with those obtained by IV-LEED and SXRD given in the literature, [116–118] while those obtained by STM and theory deviate within a factor of two. [87, 109, 116] For Bi/Ag(111), the corrugation obtained by IV-LEED lies in between the two theoretical predictions. [87, 102] Considering the surface alloys Bi and Sb on Cu(111), the outward relaxation of the alloy atoms is significantly larger compared to the respective atoms on Ag(111). [117,120,121] This can be understood as a consequence of the smaller lattice constant of the Cu(111) surface compared to Ag(111). Correspondingly there is simply less space for the alloy atoms with larger covalent radii.

6 Photoemission results of the pure surface alloys on Ag(111)

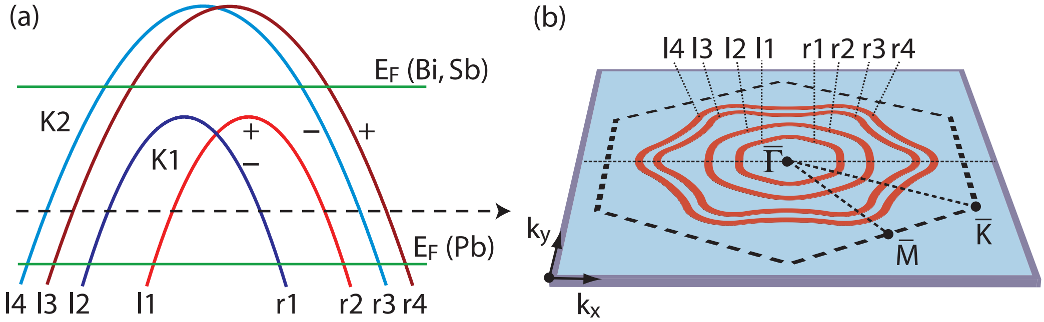

Figure 28: (a) Schematic presentation of the surface bands in the surface alloys on Ag(111), showing two groups of spin-split bands associated with the Kramers pairs $K1$ and $K2$. The Fermi level for Pb/Ag(111) is significantly lower than for Bi and Sb on Ag(111), while for Sb/Ag(111) the spin splitting is much smaller than for the other two surface alloys (not shown). (b) Constant energy surface at an energy below the crossing point of the lower Kramers pair $K1$ showing the four contours related to the Kramers pairs.

The focus of this chapter lies on the characterization of the band and spin structure of the three pure surface alloys Bi/Ag(111), Pb/Ag(111) and Sb/Ag(111) by SARPES and the subsequent explanation of the observations via the concepts introduced in the sections 4.1 and 4.2. It should be noted that all measurements of the surface alloys on Ag(111) presented in this thesis were performed at room temperature.

While there are distinct differences between the surface state band structures, such as the size of the spin splitting and the position of the Fermi level, there are also strong similarities. Fig. 28 gives a schematic view of the surface state band structure for the surface alloys on Ag(111), which consists of two Kramers pairs. The Kramers pair $K1$ is located at higher binding energies, and is entirely below the Fermi level for Bi/Ag(111) and Sb/Ag(111), while it is only partially filled for Pb/Ag(111). Whereas the band symmetry of $K1$ is mainly of sp_z type, there is also an admixture of p_xp_y symmetry, which depends on the corrugation of the surface. [87, 102] The bands belonging to $K1$ are labelled with $l2 - r2$ as illustrated in Fig. 28. Below $E_{\bar{\Gamma}}(K1)$ $l2, r2$ correspond to the $+$ branch and $l1, r1$ to the $-$ branch. Above $E_{\bar{\Gamma}}$ all labels correspond to the $+$ branch. The Kramers pair $K2$ is only partially filled for all the surface alloys on Ag(111) and has mainly p_xp_y character. The bands which belong to $K2$ are labelled with $l4, l3$ and $r3, r4$, where $l4, r4$ correspond to the $+$ branch and $l3, r3$ to the $-$ branch. In contrast to the Shockley states on clean (111) surfaces, e.g. the surface state of Au(111), where the constant energy contours are circular, the constant energy contours of K1 and K2 are hexagonal as shown in Fig. 28 (b). This is a consequence of the in-plane inversion asymmetry of the surface, which causes an anisotropic dispersion, as discussed in section 4.2. [108,119] The deviation from circular shape is stronger for larger $\boldsymbol{k}_{||}$ values, where the coupling to the lattice potential is larger. The in-plane inversion asymmetry also exerts a profound influence on both the size of the spin splitting as well as on the spin polarization (see Fig. 24 in section 4.2). [102, 108]

6.1 Spin-resolved band structure of Bi/Ag(111)

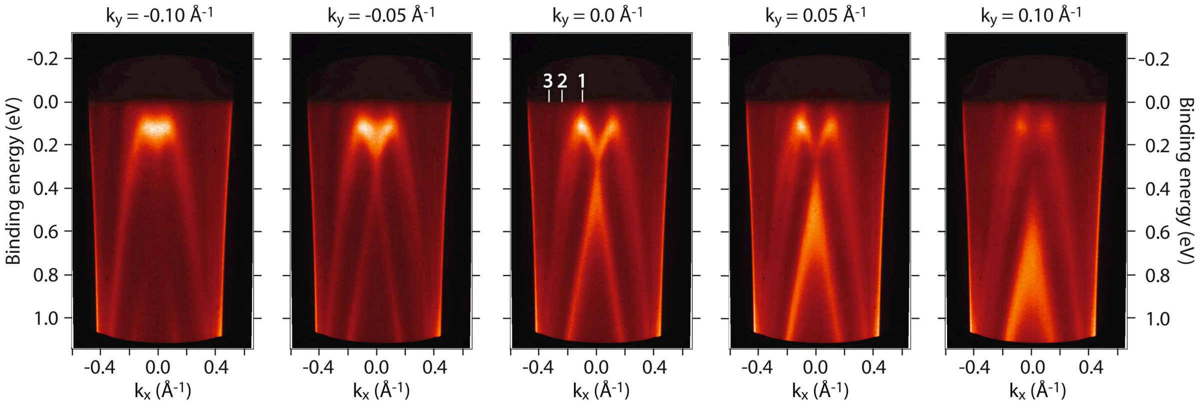

Figure 29: Surface state band dispersion of Bi/Ag(111) parallel to the $\bar{\Gamma}\bar{M}$ direction for different distances k_y in direction $\bar{\Gamma}\bar{K}$ from the SBZ center.

Out of the three pure surface alloys on Ag(111), Bi/Ag(111) shows the largest spin splitting. The giant Rashba-type spin splitting in Bi/Ag(111) was discovered in 2007 and has stimulated both theory and experiment. [102]

In Fig. 29 the surface state band structure of Bi/Ag(111) is shown around the $\bar{\Gamma}$ point measured with ARPES at a photon energy of 22 eV. k_x is along the $\bar{\Gamma}\bar{M}$ direction and k_y along $\bar{\Gamma}\bar{K}$. The photoemission intensity is symmetric along k_x with respect to $k_x = 0$ due to the experimental setup.[1] In contrast, the intensity distribution is highly asymmetric along the k_y direction due to strong differences in the transition matrix elements for different geometries (for details see section 6.5). The Kramers pair $K1$ is entirely below the Fermi level with the energy $E_0(K1) \approx 0.1$ eV and $E_{\bar{\Gamma}}(K1) \approx$ 0.3 eV. The two bands belonging to $K2$ cross the Fermi level at $k_x = 0.1$ Å^{-1} and $k_x = 0.23$ Å^{-1} as indicated

---

[1] The data shown in Figs. 29 and 30 have not been measured at COPHEE but at the SGM-3 beamline of the storage ring ASTRID. [122]

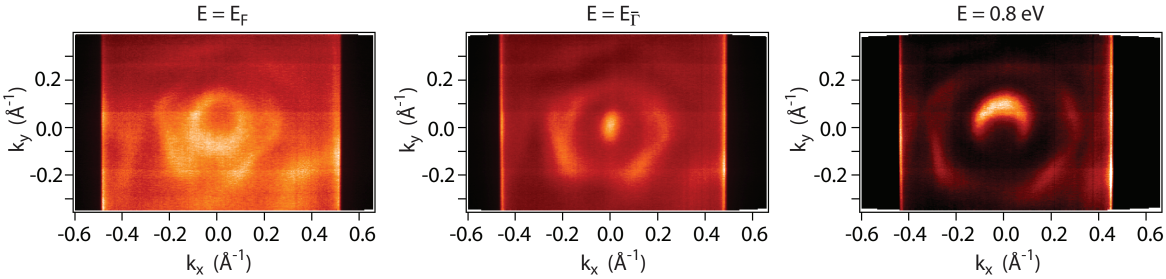

Figure 30: Constant energy surfaces at $E = E_F$ (left). $E = E_{\bar{\Gamma}}$ (middle) and $E = 0.8$ eV. For larger $\boldsymbol{k}_{||}$ values the constant energy contours of the $p_x p_y$ derived bands become hexagonal, while the sp_z derived bands have a more circular shape. k_x is approximately along $\bar{\Gamma}\bar{M}$ and k_y along $\bar{\Gamma}\bar{K}$.

by the labels 1 and 2. The label 3 corresponds to an Ag(111) bulk umklapp band. In the vicinity of $E_b = 0.1$ eV and $|\boldsymbol{k}_{||}| \approx 0.2$ Å^{-1} the $+$ branch of $K1$ and the $-$ branch of $K2$ hybridize. While from ARPES it seems that the bands actually cross, SARPES is in favor of an avoided crossing as will be shown later on. The Rashba momentum measured for $K1$ is $k_R = 0.13$ Å^{-1} and the Rashba energy is $E_R = 200$ meV. [102] The effective mass is given by $m^* = -0.35\ m_e$, where m_e is the free electron mass. For $K2$, the Rashba energy and the effective mass are not accessible in a standard ARPES measurement. An estimation for the Rashba momentum of $K2$ from the splitting along $\bar{\Gamma}\bar{M}$ at the Fermi level yields $k_R(K2) = 0.065$ Å^{-1}.

Fig. 30 shows the constant energy surfaces of Bi/Ag(111) for the three different energies $E = E_F$, $E = E_{\bar{\Gamma}} = 0.3$ eV and $E = 0.8$ eV. The intensity distribution is symmetric with respect to the $k_x = 0$ line, but highly asymmetric along k_y. At the Fermi energy E_F, the two contours correspond to the two bands of the Kramers pair $K2$. The $+$ branch of $K2$ has a pronounced hexagonal shape already at the Fermi level due to the interaction with the lattice, while the $-$ branch located at smaller $\boldsymbol{k}_{||}$ values, where the influence of the lattice is weaker, is more circular. It might be interesting to note that the hexagonal shape of $K2$ is rotated by 30° with respect to the SBZ. At $E_{\bar{\Gamma}} = 0.3$ eV, three bands are visible. The bright spot in the middle of the constant energy surface is the crossing point of the Kramers pair $K1$. In the $\bar{\Gamma}\bar{M}$ direction at $|\boldsymbol{k}_{||}| \approx 0.2$ Å^{-1} the $+$ branch of $K1$ and the $-$ branch of $K2$ can be resolved due to the more hexagonal shape of $K2$. At $E = 0.8$ eV, the outer two bands are the same as at $E_{\bar{\Gamma}}$, and the circular inner band, which shows a highly asymmetric intensity distribution, is the $-$ branch of $K1$.

When going from the Fermi level towards higher binding energies (from left to right in Fig. 30), the most notable change is the more hexagonal shape of the inner band ($-$ branch) of $K2$ due to the increased interaction with the lattice. [108] Another remark-

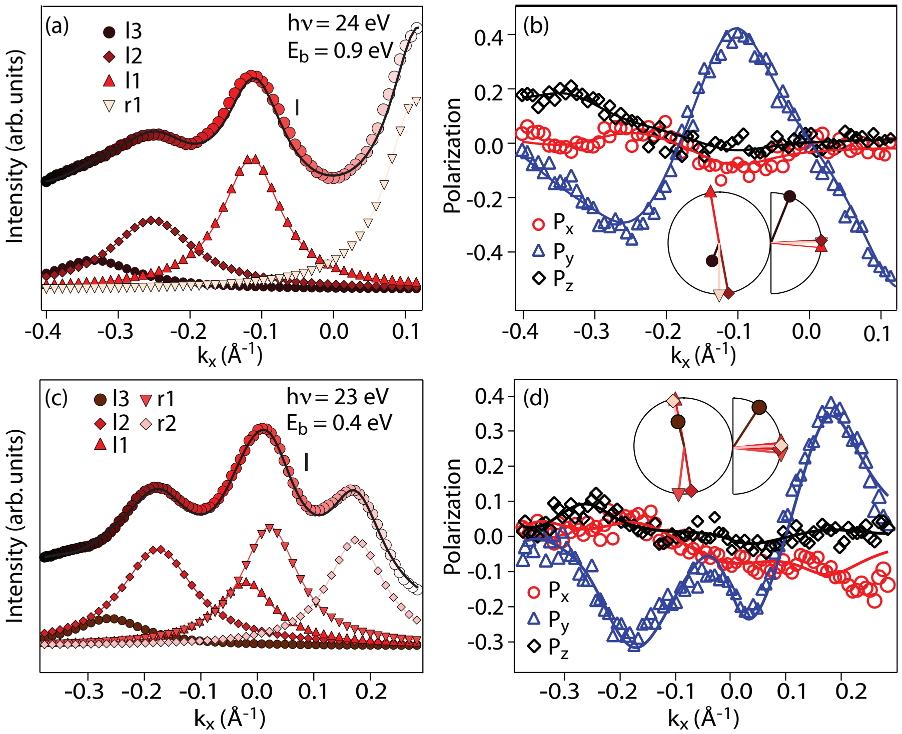

Figure 31: Spin-resolved momentum distribution curves measured at $E_b = 0.9$ eV with $h\nu = 24$ eV (top panels) and at $E_b = 0.4$ eV with $h\nu = 23$ eV (bottom panels) along the $\bar{\Gamma}\bar{M}$ direction. (a) and (c) show the spin-integrated intensities and the Lorentzian peaks of the fit. The solid line is the total intensity fit. (b) and (d) show the measured (symbols) and fitted (solid lines) spin polarization curves from the MDC. The statistical errors are smaller than the symbol size. The insets of (b) and (d) visualize the in-plane and out-of-plane spin polarization components obtained from the polarization fit, where the symbols refer to those in (a) and (c), respectively.

able point is the finding that the Kramers pair $K2$ which has mainly p_xp_y symmetry shows a much more pronounced hexagonal shape. This behavior can be understood as a consequence of stronger sensitivity to the in-plane potential of the p_xp_y-like bands in comparison with the sp_z derived bands. This sensitivity to the in-plane potential and its gradients also has a strong influence on the spin structure of these bands as will be shown in the following by means of SARPES.

Fig. 31 shows SARPES measurements for the surface alloy Bi/Ag(111). Fig. 31 (a) shows the spin-integrated intensity and the individual bands contributing to a MDC taken at the binding energy $E_b = 0.9$ eV along the direction $\bar{\Gamma}\bar{M}$. In Fig. 31 (b) the corresponding spin polarization data are shown. The lines correspond to the fits of the two-step fitting routine, which is described in detail in subsection 2.3.1. The inspection of Fig. 31 (a) from negative to positive $\boldsymbol{k}_{||}$ values shows that the MDC first cuts the

Bi/Ag(111)					
$E_b = 0.4$ eV, $\bar{\Gamma}\bar{M}$					
$k_{\parallel}$ (Å^{-1})	-0.26	-0.18	-0.02	0.02	0.18
ϕ (°)	104 ±10	-81 ±2	101 ±4	-97 ±2	104 ±1
θ (°)	57 ±7	-1 ±2	6 ±5	-6 ±2	3 ±1
	$l3$	$l2$	$l1$	$r1$	$r2$
$E_b = 0.9$ eV, $\bar{\Gamma}\bar{M}$					
$k_{\parallel}$ (Å^{-1})	-0.34	-0.25	-0.11	0.12	
ϕ (°)	-111 ±17	-80 ±2	99 ±1	-90 ±1	
θ (°)	68 ±5	3 ±2	-5 ±1	1 ±1	

Table 3: Band positions and directions (given by θ and ϕ) of the spin polarization vectors of the surface state bands $l3 - r2$ for the Bi/Ag(111) surface alloy at $E_b = 0.4$ eV and $E_b = 0.9$ eV. The angular errors are estimates resulting from the fitting procedure to the spin polarization spectra.

band labelled with $l3$ (the labels are in accordance with those given in Fig. 28). From the spin polarization data it can be concluded that this band belongs to the $-$ branch of $K2$ as explained below. The next three bands $l2$, $l1$ and $r1$ belong to the Kramers pair $K1$. The momentum splitting between $l1$ and $l2$ is $\Delta k = 0.14$ Å^{-1} at $E_b = 0.9$ eV. Note that this value is smaller than $2k_R(K1) = 0.26$ Å^{-1} found in Ref. [102]. This is a consequence of the non-parabolic dispersion which causes a smaller difference Δk for the bands of $K1$ at larger binding energies (see Fig. 29).

The application of the two-step fitting routine to the data reveals that the bands of $K1$ have spin polarization vectors which are mainly in-plane (out-of plane angle $\theta < 7°$) and approximately pointing in the $\pm y$ direction (roughly tangential to the constant energy contours), in agreement with time reversal symmetry. The in-plane part of the spin polarization vector of the $+$ branch of $K1$ shows a counterclockwise rotation while for the $-$ branches of $K1$ and $K2$ the rotation is clockwise. Hence both $K1$ and $K2$ have a positive chirality, which due to the hole-like character of the bands implies $\alpha_R < 0$. The in-plane deviations of the spin polarization vectors from pure P_y (the direction perpendicular to the momentum) are smaller than 15°. We assume that this deviation from pure P_y spin polarization is a consequence of both the non-circular constant energy contours and a slight tilt in the sample mounting. In contrast to the sp_z derived bands of $K1$, the p_xp_y derived band $l3$ shows a notable out-of plane spin polarization. For the MDC shown in Fig. 31 (a) we found $\theta_{l3} = 68° \pm 5°$, i.e. a rotation of 68° out of the surface plane. While the P_z component is larger than predicted by theory, where $P_z \approx 10\%$ was predicted, [102] the observation of the out-of-plane component confirms the assignment

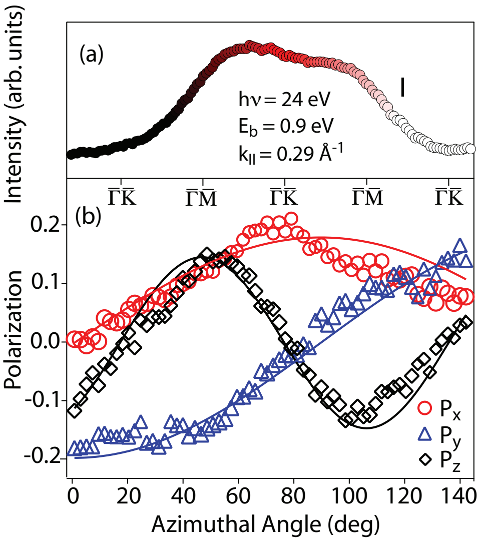

Figure 32: (color online) Azimuthal scan of intensity (a) and spin polarization (b) at $E_b = 0.9$ eV and $k_{||} = 0.29$ Å^{-1} ($hv = 24$ eV). The sine curves (solid lines) are not fits but solely a guide to the eye. The z component of the spin polarization vector shows approximately a sine like behavior with $2\pi/3$ periodicity and extrema in the $\bar{\Gamma}\bar{M}$ direction. The statistical errors are smaller than the symbol size.

of the bands.

The spin polarization vectors obtained with the two-step fitting routine are shown in the insets of Fig. 31 (b), where the symbols refer to those in Fig. 31 (a), and the corresponding values are summarized in Table 3. All bands are found to be fully spin polarized. The full circle corresponds to the in-plane part, where the horizontal and vertical axis is given by P_x and P_y, respectively. The half circle shows the out-of-plane rotation, where the horizontal axis is set along the direction of the in-plane spin polarization for each band.

Fig. 31 (c) and (d) show SARPES data obtained at a binding energy of 0.4 eV in direction $\bar{\Gamma}\bar{M}$. The cut is slightly below the energy $E_{\bar{\Gamma}}$ of the crossing point of K1. This means that the measurement passes through a region with significant overlap of two bands with different spin polarization and from the spin-integrated data only three peaks are clearly visible. In such a case a vectorial spin analysis such as the two-step fitting routine is needed in order to resolve the polarization of the individual bands. Using the two-step fitting routine we find again that the bands $l2-r2$ of $K1$ are polarized within the surface plane approximately tangential to the constant energy contour, while the band $l3$ shows an out-of-plane spin polarization component ($\theta_{l3} = 57°$). The exact values for the spin polarization vectors of the individual bands are summarized in Table 3 and shown in the insets of Fig. 31 (d).

In Fig. 32 the azimuthal dependency of the spin polarization vector of $l3$ for $E_b = 0.9$

eV and $|\boldsymbol{k}_{||}| = 0.29$ Å^{-1} is shown. In agreement with the threefold rotational symmetry, the out-of-plane spin polarization component P_z shows an alternating behavior with a $2\pi/3$ periodicity. The out-of-plane spin polarization has extrema in the $\bar{\Gamma}\bar{M}$ direction and is zero along $\bar{\Gamma}\bar{K}$. This is in agreement with $\bar{\Gamma}\bar{M}$ being a structural mirror plane. P_x and P_y on the other hand are 2π periodic, as expected from the previous finding that the in-plane spin polarization component is essentially perpendicular to the momentum $\boldsymbol{k}_{||}$. As will be shown later on for the case of Pb/Ag(111), the spin polarization vector rotates in and out of the surface plane as a function of the azimuthal direction, while it length $|\boldsymbol{P}|$ is conserved.

6.2 Spin-resolved band structure of Pb/Ag(111)

For the Pb/Ag(111) surface alloy, the spin splitting found in the experiment is considerably smaller than for the Bi/Ag(111) system, i.e. $k_R = 0.03$ Å^{-1}. [109, 123] This is surprising at first since the atomic number of Pb ($Z = 82$) is similar to the one of Bi ($Z = 83$) and correspondingly a spin splitting of similar size could in principle be expected. The surface state band structure of Pb/Ag(111) also consists of two Kramers pairs, with band symmetries similar to Bi/Ag(111). [87] Apart from the size of the spin splitting, the main difference is that, because Pb has one valence electron less than Bi, the band crossing of the spin-split surface states is above the Fermi level in the Pb/Ag(111) surface alloy, which complicates the experimental classification of the different bands.

The band structure as measured by ARPES is displayed in Fig. 33 (a), which shows a spin-integrated cut through the SBZ along the $\bar{\Gamma}\bar{K}$ direction. Three features marked by arrows are visible. The white arrows point at the bands $l1$ and $l2$ from $K1$, while the bands $l3$, $l4$ of $K2$ and the bulk umklapp band are in the region of the red arrow. They can only be separated with the additional spin information as shown below. Note that the assignment of the bands is not a priori clear from the spin-integrated data given in Fig. 33 (a). In fact, it has been argued that the inner two bands could originate from different surface states and are thus not spin-split counterparts. [23, 87] However, this interpretation is in contrast to more recent experimental results, [109,110,124,125] partly presented in this thesis, and will not be discussed further.

Figs. 33 (b)-(e) give an overview of the SARPES data on the Pb/Ag(111) surface alloy. The data are all obtained with the photon energy $h\nu = 24$ eV at the binding energy $E_b = 0.15$ eV, with the results obtained from the vectorial spin analysis summarized in Table 4. Fig. 33 (b) shows the spin-integrated intensity of a MDC along $\bar{\Gamma}\bar{M}$. From the fit to the momentum distribution curve the positions, widths and intensities of the different surface state bands of the Pb/Ag(111) surface alloy are extracted. This yields a momentum splitting of $\Delta k = 0.05$ Å^{-1} for the bands of both $K1$ and $K2$. From the

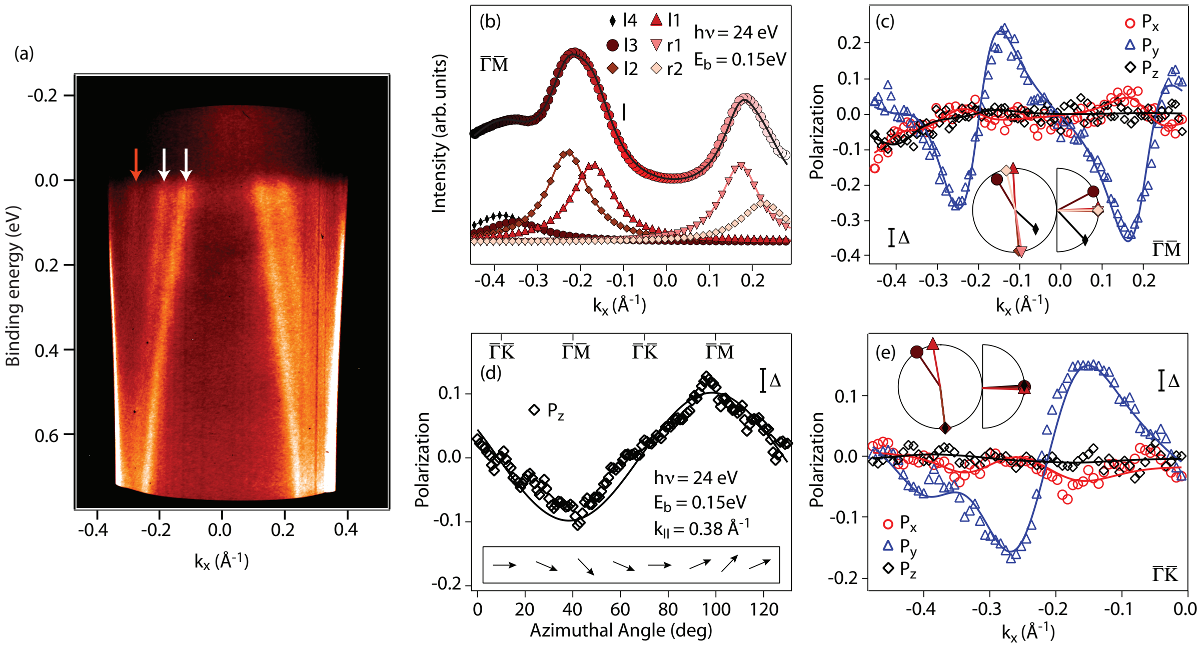

Figure 33: (a) Surface state band dispersion of Pb/Ag(111) in the direction $\bar{\Gamma}\bar{K}$. The two white arrows mark the bands $l1$ and $l2$ of $K1$. The bands of $K2$ and the bulk umklapp band can not be resolved and are in the region of the red arrow. (b-e)SARPES data obtained with $hv = 24$ eV at $E_b = 0.15$ eV. (b) Measured MDC in the $\bar{\Gamma}\bar{M}$ direction, showing also the fitted peaks contributing to the intensity. The solid line is the intensity fit. (c) Measured (symbols) and fitted (solid lines) spin polarization data corresponding to (b). (d) The measured z component of the spin polarization vector (symbols) obtained from an azimuthal scan at $k_{||} = 0.38$ Å^{-1}, where band $l4$ is located, shows approximately a sine like behavior with $2\pi/3$ periodicity (solid line) and extrema in the $\bar{\Gamma}\bar{M}$ direction. The inset visualizes the out of plane rotation as a function of the azimuthal angle. (e) Spin polarization resulting from a MDC (not shown) in the $\bar{\Gamma}\bar{K}$ direction. The four peaks $l4 - l1$ contribute to the spin polarization spectrum. Note the different $k_{||}$ scale between (c) and (e). The insets in (c) and (e) show the corresponding spin polarization components. The symbols refer to those defined in (b). The largest statistical errors of the spin polarization spectra are given by Δ.

fit to the spin polarization data shown in Fig. 33 (c), the spin polarization vectors of the individual bands are extracted. All surface state bands are found to be fully spin polarized. Similar to Bi/Ag(111), the bands of $K1$, which have primarily sp_z character, are spin polarized in the surface plane along the y axis and have a positive chirality. The p_xp_y derived bands of $K2$ on the other hand show a notable out-of-plane spin polarization component. The out-of-plane rotation of $l4$ is larger than that of $l3$, but

Pb/Ag(111)						
$E_b = 0.15$ eV, $\bar{\Gamma}\bar{M}$						
$k_{\|\|}$ (Å^{-1})	-0.38	-0.35	-0.23	-0.18	0.18	0.23
ϕ (°)	-42 ±32	120 ±21	-85 ±2	93 ±2	-81 ±2	102 ±3
θ (°)	-47 ±8	28 ±11	-1 ±2	3 ±2	0 ±2	1 ±3
	$l4$	$l3$	$l2$	$l1$	$r1$	$r2$
$E_b = 0.15$ eV, $\bar{\Gamma}\bar{K}$						
$k_{\|\|}$ (Å^{-1})	-0.40	-0.36	-0.27	-0.18		
ϕ (°)	-83 ±10	124 ±7	-83 ±2	100 ±2		
θ (°)	4 ±11	2 ±8	-1 ±2	-2 ±2		

Table 4: Band positions and directions (given by θ and ϕ) of the spin polarization vectors of the surface state bands $l4 - r2$ for the Pb/Ag(111) surface alloy at $E_b = 0.15$ eV. The angular errors result from the fitting procedure to the spin polarization spectra.

reduced compared to Bi/Ag(111), i.e. 46° and 29° for $l4$ and $l3$, respectively. Due to the threefold rotational symmetry of the structure, adjacent $\bar{\Gamma}\bar{M}$ directions are not equivalent, as reflected in the spin polarization component P_z. The dependence of the out-of-plane spin polarization component of band $l4$ at $k_{||} = 0.38$ Å^{-1} on the azimuthal angle is shown in Fig. 33 (d). It shows an approximate sine like behavior with a $2\pi/3$ periodicity comparable to Fig. 32 (b).

The analysis of the MDC spin polarization spectra shown in Fig. 33 (e), to which the bands $l4 - l1$ contribute, indicates that the polarization vectors of the bands $l4$ and $l3$ lie in the surface plane for k_x along $\bar{\Gamma}\bar{K}$, while the bands are still fully spin polarized: the vanishing spin polarization in the P_z component is compensated by the appearance of spin polarization in the y component. Combining the information from Figs. 33 (c), (d) and (e) leads us to the conclusion that the spin polarization vector of band $l4$ rotates out of and into the surface plane as a function of the azimuthal angle, while the in-plane part of the spin polarization vector remains approximately tangential to the constant energy surface. The out-of-plane rotation is schematically indicated by the vectors in Fig. 33 (d).

Again it should be noted that, due to the time reversal symmetry the surface remains non-magnetic, which means that the vector sum of all spin polarization vectors throughout the SBZ is zero. For P_z, this is exemplified by the change of sign for adjacent $\bar{\Gamma}\bar{M}$ directions. Furthermore, from the peak positions of $l2$ and $l1$ (see Table 4 for values), we find that the Rashba splitting of the inner two bands is larger for the $\bar{\Gamma}\bar{K}$ direction than for $\bar{\Gamma}\bar{M}$, which is a ramification of the non circular constant energy surface.

6.3 Spin-resolved band structure of Sb/Ag(111)

The surface state band structure of Sb/Ag(111) features the two Kramers pairs $K1$ and $K2$ as shown in Fig. 34 (a). The energy of the crossing point of $K1$ is $E_{\bar{\Gamma}} = 0.27$ eV, which is 0.03 eV closer to E_F as compared to Bi/Ag(111). In contrast to Bi/Ag(111) and Pb/Ag(111), the spin splitting is so small that it is not resolved in Fig. 34 (a). Similar to Bi/Ag(111), the $p_x p_y$ derived states of $K2$ have a strongly hexagonal shape while the sp_z like states of $K1$ are more circular. The hexagonal shape of the bands becomes more pronounced for larger $\boldsymbol{k}_{||}$ as shown in the different constant energy contours in Fig. 34 (b)-(e). At $E_b = 2.1$ eV (see Fig. 34 (e)) also $K1$ shows a perceivably hexagonal shape. Again it should be noted that this deviation from the circular contour of a 2D free electron gas is due to the influence of the crystal lattice. In this respect it is of interest to note again that the hexagonal shape of $K2$ is rotated by 30° with respect to

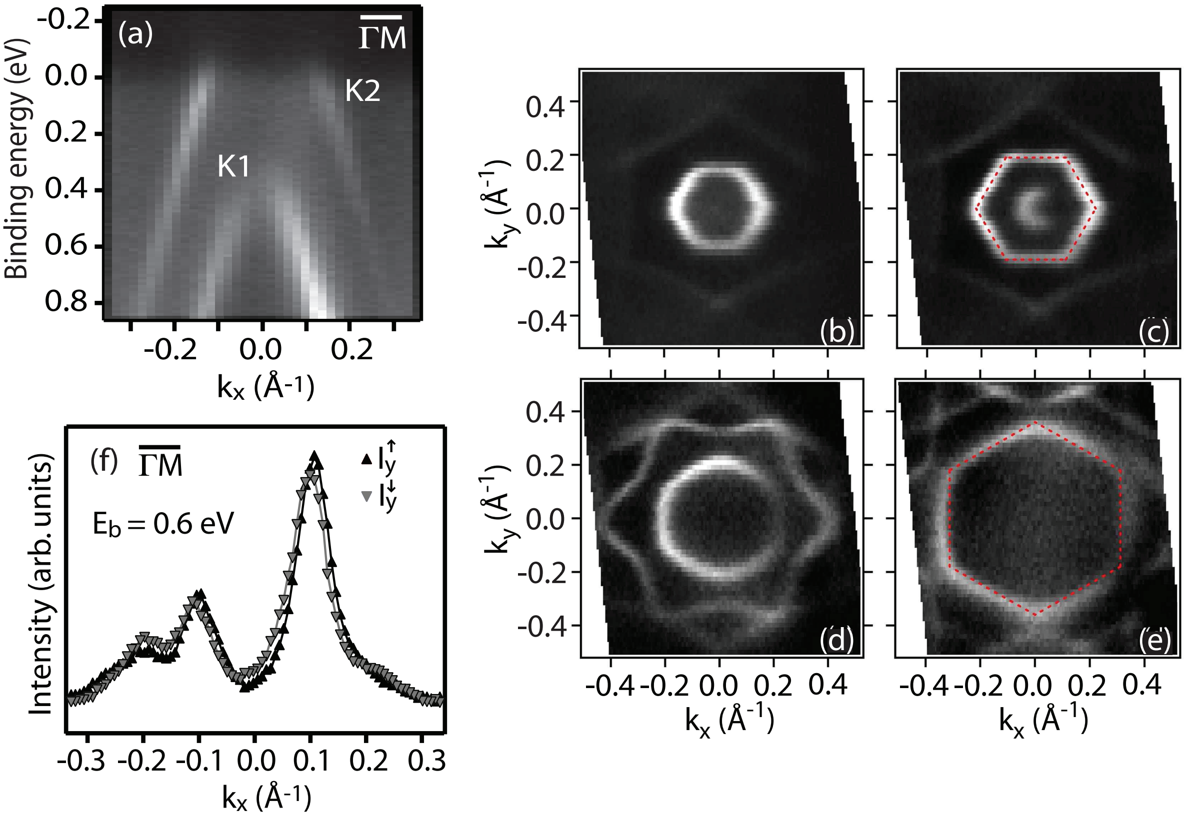

Figure 34: (a) Surface state band dispersion of Sb/Ag(111) in the direction $\bar{\Gamma}\bar{M}$. Constant energy contours obtained at (b) the Fermi level, (c) 0.4 eV, (d) 1,3 eV and (e) 2.1 eV binding energy (adapted from Ref. [119]). (f) Spin-resolved intensities $I_y^{\uparrow}$ and $I_y^{\downarrow}$ for a MDC along $\bar{\Gamma}\bar{M}$ at $E_b = 0.6$ eV.

the SBZ, while $K1$ is congruent with the hexagon of the SBZ.

In Fig. 34 (f) the spin-resolved intensities $I_y^\uparrow$ and $I_y^\downarrow$ are presented for a MDC along $\bar{\Gamma}\bar{M}$ at a binding energy of 0.6 eV. The spin-resolved MDC shows a clear signature of a Rashba-type spin-orbit splitting with a momentum shift $\Delta k = 2k_R = 0.01$ Å^{-1} between each set of bands. This spin splitting is comparable to the intrinsic linewidth of the surface state bands, which has profound consequences on the spin polarization measured in a SARPES experiment as will be shown in chapter 8. For small binding energies $E_b \lesssim 1$ eV the dispersion of $K1$ can be assumed to be parabolic from Figs. 34 (b)-(d). This allows to deduce the Rashba energy $E_R = 0.87$ meV and the Rashba constant $\alpha_R = -0.36$ eV Å from the measured Rashba momentum k_R using $m^* = -0.10\ m_e$.

6.4 Interpretation of the similarities and differences of the pure surface alloys

The SARPES experiments on Bi/Ag(111), Pb/Ag(111) and Sb/Ag(111) presented in the previous sections clearly proof the Rashba-type nature of the surface states. The individual surface state bands are found to be fully spin polarized and show, depending on the direction and the orbital symmetry, a sizable out-of-plane rotation of the spin polarization vector. Similar to the surface state of Au(111), both Kramers pairs $K1$ and $K2$ have a positive chirality. However, due to the hole-like character of the bands $K1$ and $K2$ this implies that $\alpha_R < 0$ for the surface alloys on Ag(111) in contrast to Au(111). This is because due to the surface corrugation the main weight of the surface state wave function lies below the alloy atoms, i.e. between the alloy atoms and the Ag atoms of the first layer of the substrate, whereas for Au(111) the wave function is shifted towards the vacuum side. An overview of the parameters α_R, k_R and E_R obtained from the experiments for the respective sp_z derived surface states $K1$ of the three pure surface alloys on Ag(111) is given in Table 5. We now discuss the observed differences of the size of the Rashba effect.

	α_R	k_R	E_R	m^*	Δz	**Ref.**
Bi/Ag(111)	-3.05 eVÅ	0.13 Å^{-1}	200 meV	-0.35 m_e	0.65 Å	[102]
Pb/Ag(111)	-1.42 eVÅ	0.03 Å^{-1}	21 meV	-0.15 m_e	0.46 Å	[123]
Sb/Ag(111)	-0.36 eVÅ	0.005 Å^{-1}	0.87 meV	-0.10 m_e	0.10 Å	

Table 5: Characteristic parameters for the sp_z surface state of the different surface alloys on Ag(111). Note that due to the lack of spin resolution Refs. [102, 123] only give the absolute value of the Rashba constant.

We start by noting that the size of the spin splitting for Bi/Ag(111) is much larger than for e.g. Au(111) and Bi(111) as reflected in the magnitude of the Rashba parameters $|\alpha_R(\text{Au}(111))| = 0.33$ eV Å, [6] $|\alpha_R(\text{Bi}(111))| = 0.56$ eV Å [12] and $|\alpha_R(\text{Bi/Ag}(111))| = 3.05$ eV Å. [102] The dramatic increase in the size of the spin splitting for Bi/Ag(111) is a consequence of the combination of several aspects. First of all, there is the heavy element Bi with large atomic spin-orbit coupling. But since only 1/3 of the atoms in the unit cell are Bi atoms and 2/3 are Ag atoms, this can not explain the size of the Rashba effect in Bi/Ag(111), in particular in comparison with Bi(111). Hence the reason has to be the structure of the surface alloy. As shown in section 5, Bi/Ag(111) is in-plane inversion asymmetric and the surface is highly corrugated ($\Delta z = 0.65 \pm 0.10$ Å [110]). The in-plane inversion asymmetry and the corresponding in-plane potential gradients are particularly strong in the sense that there are heavy atoms (Bi) surrounding light atoms (Ag), which causes a large in-plane asymmetry of the wave function with respect to the individual nuclei and strongly enhances the spin splitting. [108] Apart from the increased spin splitting, the in-plane inversion asymmetry manifests itself in the noncircular constant energy contours and the finite out-of-plane spin polarization component P_z. In addition, most of the weight of the surface state wave function lies in the surface layer, where the envelope function is highly asymmetric in the z direction.

Pb/Ag(111) shows a significantly smaller spin splitting than Bi/Ag(111)(see Table 5 for values). Although the nuclear number of Pb ($Z = 82$) is smaller than that of Bi ($Z = 83$) and the atomic spin-orbit coupling is smaller in Pb, this effect is too small to explain the origin of the differences between Pb/Ag(111) and Bi/Ag(111). [87]

The spin splitting found in Sb/Ag(111) is very small as compared to both Bi/Ag(111) and Pb/Ag(111). However, the fact that Sb(111) features a large spin splitting as shown in section 4.2 indicates that the atomic number of Sb can not be the sole reason for the small spin splitting.

While the in-plane lattice constants are the same for the different surface alloys on Ag(111), the surface corrugation Δz notably differs as shown in chapter 5 and summarized in Table 5. The influence of the size of the Rashba-type spin splitting on the surface corrugation is shown in Fig. 35 (a) for Pb/Ag(111) and two different relaxations of the Pb atoms, $\Delta z = 0.67$ Å (filled circles) and $\Delta z = 0.97$ Å. For $\Delta z = 0.67$ Å, which is close to the experimentally determined surface corrugation, the calculations found a spin splitting of $k_R \approx 0.04$ Å^{-1} similar to the value determined in experiments. For the surface corrugation $\Delta z = 0.97$ Å a Rashba momentum $k_R = 0.11$ Å^{-1} was found, a value similar to the one found for Bi/Ag(111). This sizable difference clearly demonstrates the influence of the surface corrugation.

The dependency of the size of the spin splitting on the surface corrugation can be un-

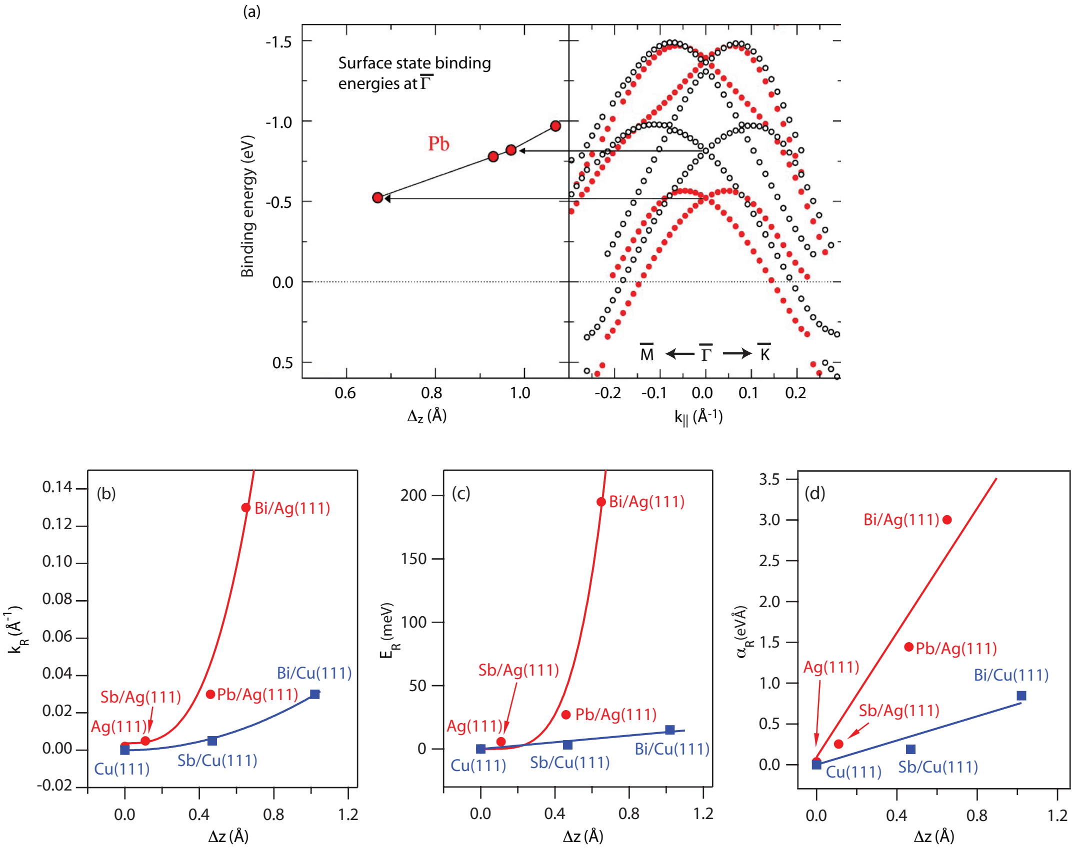

Figure 35: (a) First principles calculations of the surface state band structure for two different relaxations $\Delta z = 0.67$ Å (filled circles) and $\Delta z = 0.97$ Å (open circles) of the Pb atoms (adapted from Ref. [87]). A larger surface corrugation yields a larger spin splitting. (b)-(d) Characteristic experimental parameters (b) k_R, (c) E_R and (d) α_R as a function of the outward relaxation Δz for Ag(111), Cu(111) and the surface alloys on Ag(111) and Cu(111). The lines are drawn as a guide to the eye.

derstood in terms of the asymmetry of the wave function as explained in Ref. [87]. As argued in section 4.1, the size of the spin splitting is essentially determined by the asymmetry of the wave function in the vicinity of the nuclei, as represented by the mixture of different orbitals. For a (hypothetical) flat Bi/Ag(111) surface alloy, the s:p_z ratio of $K1$ is 4:1 and the corresponding Rashba momentum is $k_R \approx 0.05$ Å^{-1}. A small outward relaxation of the Bi atoms to $\Delta z = 0.1$ Å changes this ratio to 2:1 and correspondingly increases the Rashba momentum to approximately 0.07 Å^{-1}. When the surface corrugation is further increased ($\Delta z = 0.87$ Å), the in-plane orbitals $p_x p_y$ and the sp_z-type orbitals mix and the spin splitting is given by $k_R = 0.13$ Å^{-1}. These large differences clearly indicate that the main reason for the different sizes of the spin splitting found in the surface alloys on Ag(111) is the surface corrugation rather than the atomic number of the alloy atoms.

Figs. 35 (b)-(d) show the parameters k_R, E_R and α_R characteristic for a Rashba system versus the surface corrugation Δz for the surface alloys on Ag(111) (red points) and Cu(111) (blue squares) as well as the corresponding clean surfaces. Indeed, for both the surface alloys on Ag(111) and on Cu(111), the parameters increase as a function of the surface corrugation. However, while the same alloy atoms X show a larger outward relaxation on Cu(111) as compared to Ag(111), the spin splitting is smaller for X/Cu(111) than for X/Ag(111), which can again be understood in terms of the symmetry of the surface states wave function. [24] In that respect, the spin splitting reaches a maximum for a certain amount of outward relaxation of the alloy atoms.

6.5 Photoemission transition matrix elements in Bi/Ag(111) and Sb/Ag(111)

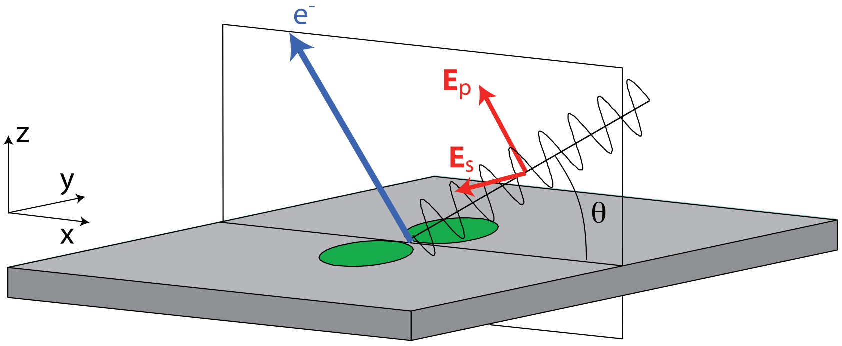

Figure 36: Schematic picture used to illustrate the coupling of the electric field of the incoming light to the orbitals of the electronic states.

The measured spectral weight of an ensemble of states depends strongly on several parameters such as measurement geometry, symmetry of the initial state and final state wavefunction, photon beam polarization and excitation energy. These effects are described by the matrix element in correspondence to the transition matrix in Fermis golden rule. In the one-electron approximation, the measured photoemission intensity from an initial state i to a final state f is proportional to the transition probabilities

$$I_{fi} \propto \omega_{fi} = |\langle f\, | \boldsymbol{A} \cdot \boldsymbol{\nabla} |\, i \rangle|^2 \, \delta(E_f - E_i - h\nu) = |t_{fi}|^2 \, \delta(E_f - E_i - h\nu). \qquad (39)$$

The matrix element $t_{fi} = \langle f\, | \boldsymbol{A} \cdot \boldsymbol{\nabla} |\, i \rangle$ is related to the efficiency of the specific photoemission process. The electric field $\boldsymbol{E}$ of the incoming light can be described by the superposition $\boldsymbol{E} = \boldsymbol{E}_s + e^{i\phi}\boldsymbol{E}_p$, where $\boldsymbol{E}_p$ and $\boldsymbol{E}_s$ corresponds to p (horizontal) and

s (vertical) polarized light as illustrated in Fig. 36. The term $|\boldsymbol{A} \cdot \boldsymbol{\nabla}|\, i\rangle$ of the matrix element describes the coupling of the light to the (momentum of the) initial states i and is here considered in the dipole approximation. For electronic states with pure s orbital symmetry, the coupling does neither depend on the light polarization nor on the angle θ between the pointing vector of the light and the sample surface. For states with orbital symmetry p_α however, the term $|\boldsymbol{A} \cdot \boldsymbol{\nabla}|\, i\rangle$ can strongly depend on the light polarization and the angle θ. For example, in the geometry of Fig. 36, p_y orbitals can only be excited by $\boldsymbol{E}_s$ where the coupling is independent of θ, and p_x orbitals are only excited by $\boldsymbol{E}_p$, where the coupling is proportional to $\sin\theta$. However, for a full description of the photoemission intensity, the final states f have to be considered.

In the first subsection of this section it will be shown that for the surface alloys the matrix element ω_{fi} dramatically depends on the photon energy. Moreover, dependent on the photon energy there is a strong left-right asymmetry with respect to the $\bar{\Gamma}$ point. In the second subsection the influence of circularly polarized light on the photoemission intensity distribution will be discussed and compared to the magnetic circular dichroism known from photoemission from core levels and resonance lines.

6.5.1 Photon energy dependence

Fig. 37 (a) shows schematically the surface state band structure of Bi/Ag(111), and Figs. 37 (b)-(i) show spin-integrated ARPES data from the Bi/Ag(111) surface alloy for different photon energies. The data shown in Fig. 37 (b) are measured with linear vertical polarized light and those shown in Fig. 37 (c)-(i) with linear horizontal polarized light. Surface states show no dispersion as a function of the $\boldsymbol{k}$-vector component normal to the surface, here k_z. Therefore, the dispersions of the Kramers pairs $K1$ and $K2$ remain unaffected by changing the photon energy.

For linear vertical polarized light (Fig. 37 (b)) the spectral weight is symmetric with respect to the $k_{||} = 0$ Å^{-1} line as a consequence of the measurement geometry, because a change of the angle θ does not change $\boldsymbol{E}_s$ (see Fig. 36). In contrast, the data of Fig. 37 (c) which were measured with linear horizontal polarized light are asymmetric with respect to the $k_{||} = 0$ Å^{-1} line. Apart from the left-right asymmetry, which will be discussed in more detail below, dramatic changes as a function of photon energy are observed in the relative intensities of the subbands, marking very strong final state effects in this system. For instance, changing the photon energy by only 2 eV from 23 to 25 eV shifts most of the spectral weight from the state $r1$ to the state $l1$ (both associated with K1), even close to the $\bar{\Gamma}$ point.

Fig. 38 (a) shows MDCs at $E_b = 0.9$ eV extracted from the data shown in Fig. 37, where the quantitative differences become even more obvious. Considering $r1$, the intensity

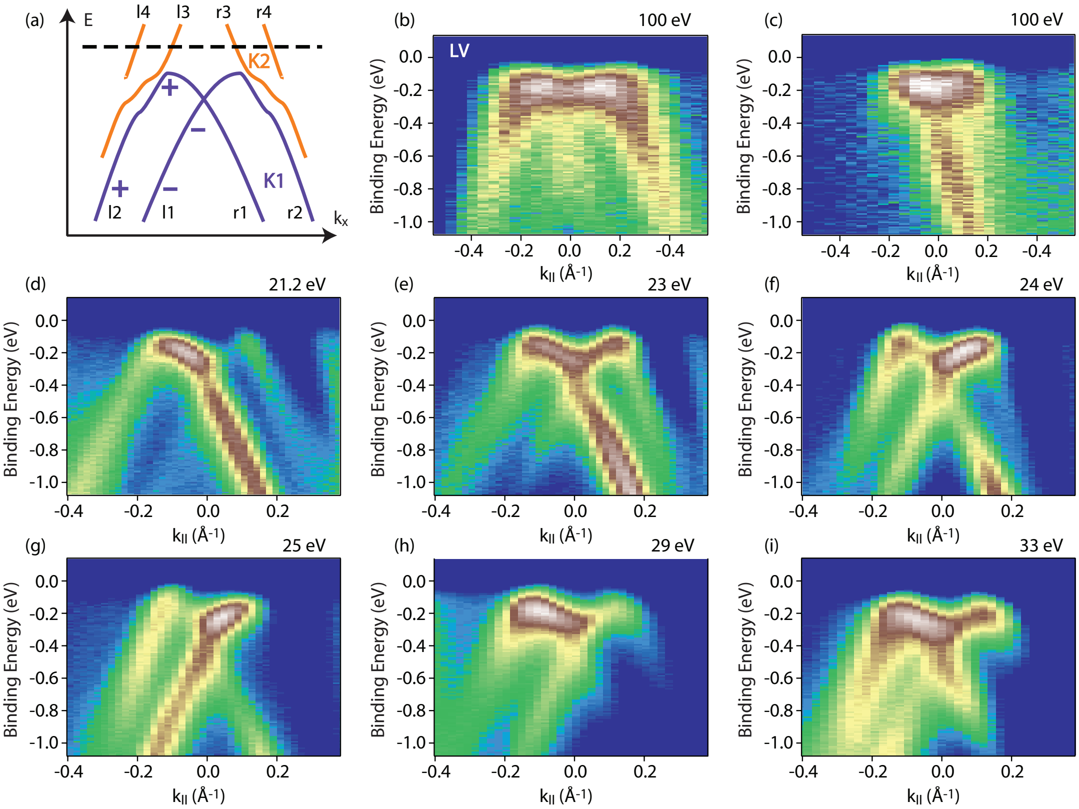

Figure 37: (a) Schematic dispersion of the Bi/Ag(111) surface states (adapted from Ref. [87]), showing the two Kramers pairs $K1$ and $K2$ and the band labeling convention. (b) Cut through the SBZ for Bi/Ag(111) with $h\nu = 100$ eV and linear vertical polarized light. (c)-(i) Photon energy dependency of the intensity distribution for the surface states of Bi/Ag(111), measured with linear horizontal polarized light. The cuts are measured along $\bar{\Gamma}\bar{M}$ and the photon energy is indicated above each panel.

decreases from a photon energy of 21.2 eV until the band almost vanishes at 29 eV and then the intensity increases again. The band $l1$ on the other hand is very weak for 21.2 eV and shows a large intensity for 29 eV. $l1$ and $r1$ show approximately an inverse behavior, i.e. the intensity of one band increases as the intensity of the other band decreases. The changes observed for $l3$ and $r3$ however are qualitatively different. First we note that the intensity of $r3$ is too weak to allow a separation from the background intensity for all photon energies in the measured range. Band $l3$ on the other hand shows a notable intensity for several photon energies. Its intensity is particularly large for 21.2 eV, then decreases up to 25 eV and is large again for 29 eV. It should be noted that the left-right asymmetries are too large to be explained by the coupling of the light to the electrons, i.e. by the term $|\boldsymbol{A} \cdot \boldsymbol{\nabla}|\, i\rangle$, and indicate a strong influence of the final states.

Asymmetric intensities in the photocurrent between one side of normal emission and

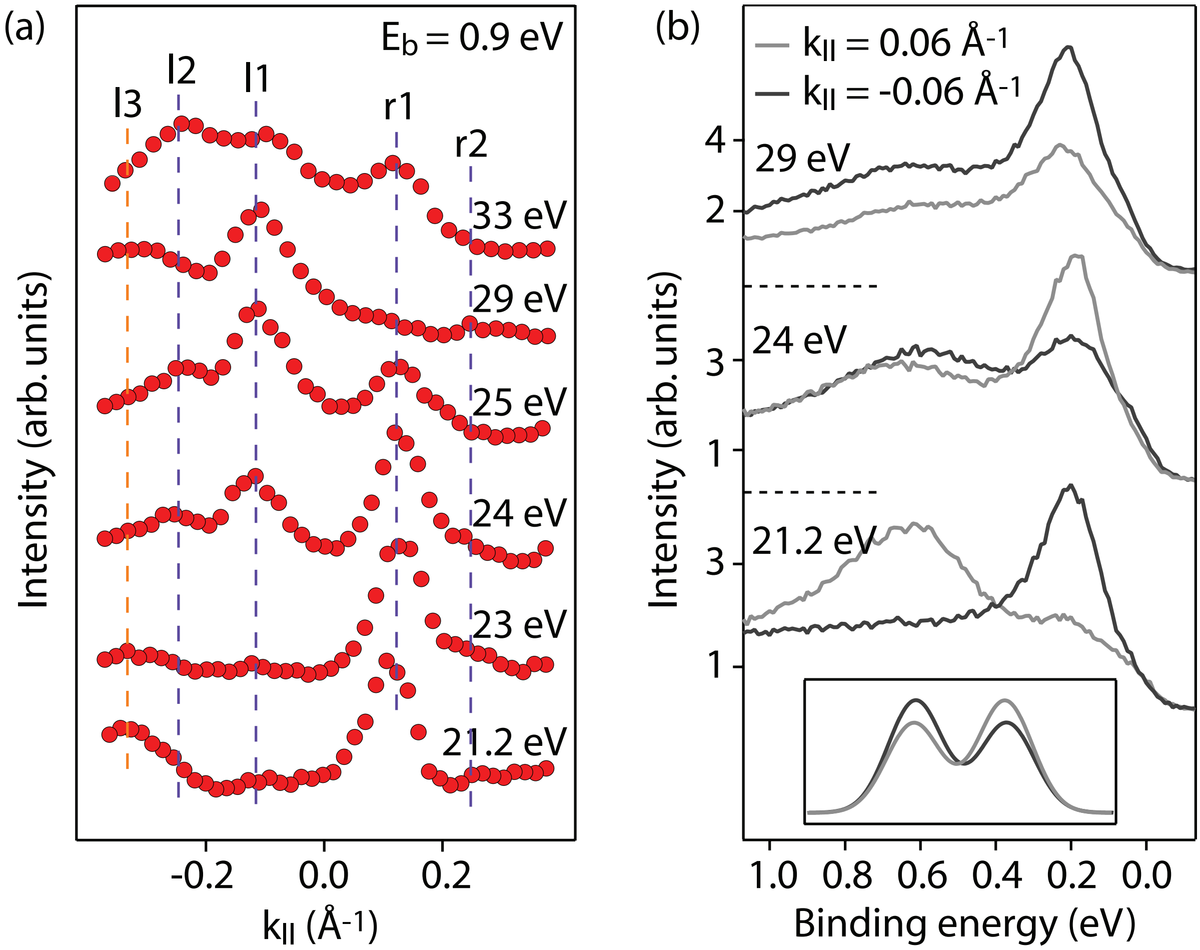

Figure 38: (a) Spin-integrated MDCs at $E_b = 0.9$ eV for different photon energies, extracted from the data of Fig. 37. The dotted lines indicate the positions of the different bands. (b) Spin-integrated EDCs extracted from the same data (Fig. 37) for $\boldsymbol{k}_{||} = \pm 0.06$ Å^{-1}. (Inset) Schematic EDCs at $\pm\boldsymbol{k}_{||}$ in the case of magnetic linear dichroism.

the other side of normal emission are also observed for e.g. the Rashba-type spin-split Au(111) surface state. [80] According to the argumentation in Ref. [80] the asymmetry can be assigned to the symmetry properties of the initial state wave function. The calculations yield an intensity distribution of the form

$$I_{\pm}(\boldsymbol{k}_{||}) = \bar{I}(\boldsymbol{k}_{||}) \pm \Delta I(\boldsymbol{k}_{||}), \tag{40}$$

where the ± corresponds to the ± branch, respectively, $\bar{I}(\boldsymbol{k}_{||}) = \bar{I}(-\boldsymbol{k}_{||})$ and $\Delta I(\boldsymbol{k}_{||}) = -\Delta I(-\boldsymbol{k}_{||})$. Eq. 40 yields energy distribution curves (EDCs) as shown schematically in the inset of Fig. 38 (b). The structure of the intensity $I_{\pm}(\boldsymbol{k}_{||})$ given in Eq. 40 is similar to the one used to describe linear magnetic dichroism, [126] and accurately describes the intensity variations observed for the Au(111) surface state at the photon energy

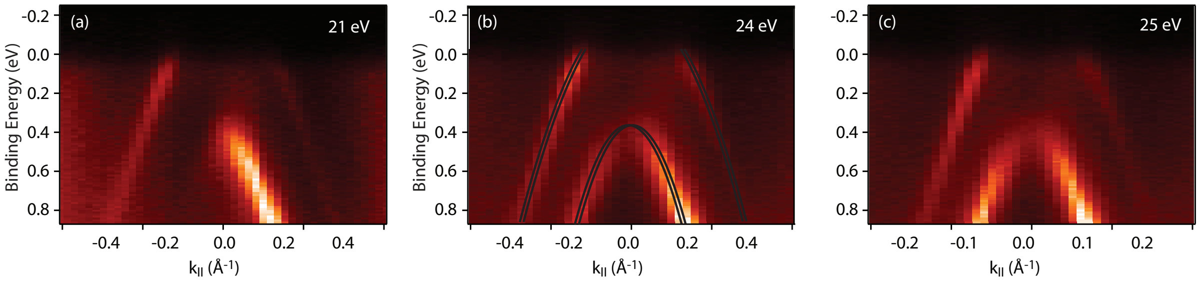

Figure 39: Photon energy dependency of the intensity distribution for the surface states of Sb/Ag(111). The cuts are measured along $\bar{\Gamma}\bar{M}$ and the photon energy is indicated in each panel. The solid lines in (b) are guides to the eye and illustrate the small Rashba-type spin splitting.

$h\nu = 21.2$ eV. However, in the simple form presented in Ref. [126], it can not explain the intensity variations observed for Bi/Ag(111) as explained below. This is a clear indication that the formalism used to describe magnetic linear dichroism can in general not be translated to Rashba systems, although the spin-polarized nature of the band structure of a Rashba system shows similarities to a magnetic system.

Fig. 38 (b) shows spin-integrated energy distribution curves for $\boldsymbol{k}_{||} = \pm 0.06$ Å^{-1} for the photon energies $h\nu = 21.2$ eV, 24 eV, and 29 eV. The EDCs cut through the $+$ and the $-$ branch of the Kramers pair $K1$. At 21.2 eV and $\boldsymbol{k}_{||} = 0.06$ Å^{-1}, the only notable peak is due to the $-$ branch of $K1$, while at $\boldsymbol{k}_{||} = -0.06$ Å^{-1} only the $+$ branch of $K1$ is visible. This finding is in agreement with the model from Ref. [80] discussed above. However, at $h\nu = 29$ eV both bands of the Kramers pair $K1$ are more intense at $\boldsymbol{k}_{||} = -0.06$ Å^{-1}, which is in contrast to the above model. This contrast, the strong photon energy dependency of the intensity distribution and the large asymmetries even close to the $\bar{\Gamma}$ point are a proof of a highly complicated final state band structure of Bi/Ag(111), most likely due to strong spin-orbit coupling.

Fig. 39 shows cuts through the SBZ of Sb/Ag(111) for the three different photon energies (a) 21 eV, (b) 24 eV and (c) 25 eV along the $\bar{\Gamma}\bar{M}$ direction measured with linear horizontal polarized light. As shown in subsection 6.3 and schematically indicated by the solid lines in Fig. 39 (b), the spin splitting is not resolved in the spin-integrated photoemission data. This implies that the intensity contributions from the two bands of each Kramers pair strongly overlap and can not easily be separated in the spin-integrated data, which would result in a symmetric intensity distribution if Eq. 40 would hold. However, for $h\nu = 21$ eV mainly the left side (negative $\boldsymbol{k}_{||}$ values) of $K2$ and the right side (positive $\boldsymbol{k}_{||}$ values) of $K1$ have a large spectral weight. This yields a partially similar scenario as observed for Bi/Ag(111) at $h\nu = 21.2$ eV (see Fig. 37), where the intensity is large on $l3$ (left side of $K2$) and $r1$ (right side of $K1$). In Fig. 39 (b) ($h\nu = 24$ eV) the asymmetries are less strong than in Fig. 39 (a) but remain qualitatively similar. For 25 eV (Fig. 39 (c)) the intensity distribution becomes almost symmetric for $K1$, but remains asymmetric for $K2$. Comparing the intensity distribution of $K1$ at 25 eV of Sb/Ag(111) (Fig. 39 (c)) with the one of Bi/Ag(111) (Fig. 37 (g)) shows remarkable differences. For Sb/Ag(111) there is slightly more spectral weight at positive $\boldsymbol{k}_{||}$ values, while for Bi/Ag(111) the sum over the two bands of $K1$ yields more spectral weight at negative $\boldsymbol{k}_{||}$ values. This finding is remarkable since the band symmetries of Sb/Ag(111) and Bi/Ag(111) are rather similar and indicate again the strong influence of the final states.

6.5.2 Light polarization effects

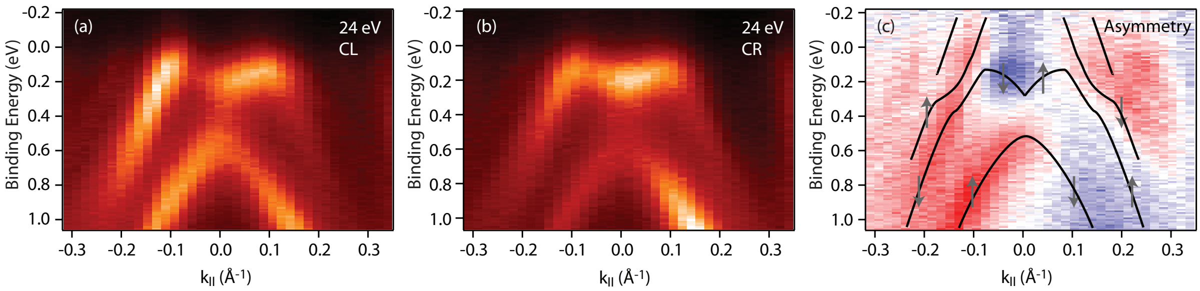

Figure 40: (a) and (b) Intensity distribution for the surface states of Bi/Ag(111) measured along $\bar{\Gamma}\bar{M}$ with (a) circular left and (b) circular right polarized light at a photon energy of 24 eV. (c) Asymmetry obtained from the intensity data given in (a) and (b). The solid lines are guides to the eye and the arrows represent spin up and spin down with respect to the y axis.

Magnetic circular dichroism (MCD) is a well established technique for the study of the magnetic properties of atoms and solids. [127] In MCD a difference spectrum is formed out of two spectra, one taken with circular left polarized light and the other with circular right polarized light. Magnetic circular dichroism relies on the idea that electrons with a certain spin, e.g. spin up, are more likely to be excited with one type of circular polarization, e.g. circular right polarized light, while the electrons with the opposite spin are more likely excited with the opposite light polarization. Correspondingly, the difference spectrum reflects the magnetic properties and is directly proportional to the degree of magnetization. While MCD is a reliable technique for the study of core levels and resonance lines, we will show here that it can not be translated to states in the valence band.

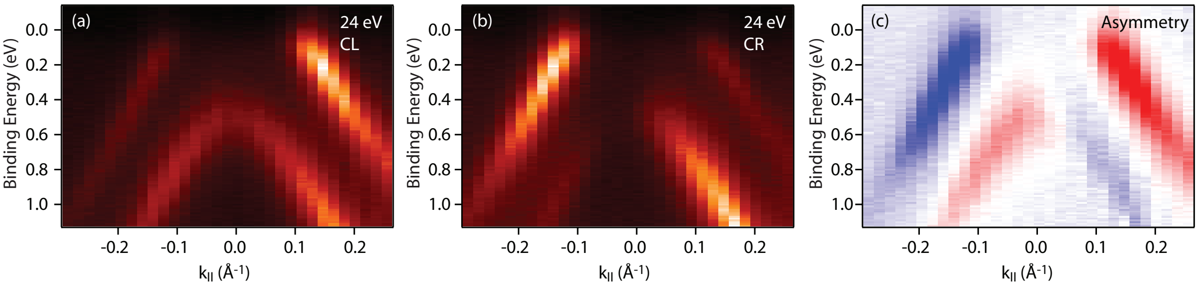

Figure 41: (a) and (b) Intensity distribution for the surface states of Sb/Ag(111) measured along $\bar{\Gamma}\bar{M}$ with (a) circular left and (b) circular right polarized light at a photon energy of 24 eV. (c) Asymmetry obtained from the intensity data given in (a) and (b).

In Fig. 40 we show cuts through the SBZ along $\bar{\Gamma}\bar{M}$ for circular left and circular right polarized light and the asymmetry $(I_{CL} - I_{CR})/(I_{CL} + I_{CR})$, where red corresponds to positive values and blue to negative values. The solid lines in Fig. 40 (b) indicate the schematic band structure and the arrows represent the direction of the spin polarization vector of the bands with respect to the y axis as measured with SARPES. The y axis is approximately the spin quantization axis for the Kramers pair $K1$, while $K2$ also features a large out-of-plane component as discussed in section 6.1. There is a small gap at $\boldsymbol{k}_{||} = 0$ Å^{-1} because the cut does not precisely go through $\bar{\Gamma}$ due to a small sample tilt. If the same ideas exploited in the MCD would apply for photoemission from valence bands (and correspondingly surface states), the colors and the spin polarization vectors of the bands would match, i.e. one could assign a color to spin-up electrons and a color to spin-down electrons. An inspection of Fig. 40 (c) shows that this is not the case. In particular, both bands of $K1$ have the same color for binding energies $E_b \gtrsim 0.5$ eV (red for negative and blue for positive $\boldsymbol{k}_{||}$ values), which is in contrast to their opposite spin polarization vectors.

That the principles of MCD can not be applied to photoemission from surface states becomes even more clear when investigating the spectral weight measured from Sb/Ag(111). The spin-integrated intensity of a cut through the SBZ is shown in Fig. 41 (a) for circular left polarized light and in Fig. 41 (b) for circular right polarized light. Since the spin splitting of the bands is so small that the bands are not separated in the spin-integrated measurements, the asymmetry shown in Fig. 41 (c) should essentially yield zero if circular left polarized light would preferentially excite one spin direction and circular right polarized light the other spin direction. However, there is a clear left right asymmetry and the colors on both sides of the $\bar{\Gamma}$ point are opposite.

Concluding this subsection it was shown that the principles of MCD can not be applied to Rashba-type spin-split surface states by comparing the spin structure as measured with SARPES with the asymmetries obtained between circular left and circular right polarized light.

7 A fully tunable Rashba system: $\mathrm{Bi}_x\mathrm{Pb}_y\mathrm{Sb}_{1-x-y}$/Ag(111)

In perspective of possible applications making use of the Rashba effect, such as e.g. the spin field-effect transistor (see section 3.3 for details), a large Rashba-type spin splitting is desirable. Whereas in semiconductor heterostructures the size of the splitting can be tuned by an external gate voltage, in this chapter the ternary surface alloy $\mathrm{Bi}_x\mathrm{Pb}_y\mathrm{Sb}_{1-x-y}$/Ag(111) is presented, in which both the size of the spin splitting and the position of the Fermi level can be independently tuned by variation of material parameters. Although the Ag(111) substrate hampers the observation of spin currents at the surface, the ternary surface alloy is an exquisite model system to study the fundamentals of many intriguing effects related to Rashba-type spin-orbit coupling, such as a renormalization of the Fermi liquid parameters, [93] changes in the electron-phonon coupling parameter, [37] and an enhancement of the superconductivity transition temperature. [94]

In this chapter the band and spin structure of the two mixed surface alloys $\mathrm{Bi}_x\mathrm{Pb}_{1-x}$/Ag(111) and $\mathrm{Bi}_x\mathrm{Sb}_{1-x}$/Ag(111) will be introduced and the formation of the ternary surface alloy $\mathrm{Bi}_x\mathrm{Pb}_y\mathrm{Sb}_{1-x-y}$/Ag(111) will be shown as a proof of principle. In these mixed surface alloys the region where $E_{\bar{\Gamma}} < E_F < E_0$ becomes accessible, and it will be shown that in this region unconventional Fermi surface spin textures can be observed. Moreover, the implications of the topological transition of the Fermi surface occurring when $E_F = E_{\bar{\Gamma}}$ for the transport of spin will be discussed. For the sake of clarity, only the inner Kramers pair $K1$ will be considered throughout this chapter.

7.1 Tuning the Fermi level: $\mathrm{Bi}_x\mathrm{Pb}_{1-x}$/Ag(111)

In subsection 6.1 it was shown that the Rashba effect is dramatically enhanced in the Bi/Ag(111) and Pb/Ag(111) surface alloys. The size of the spin splitting is achieved through a combination of three ingredients, namely the presence of heavy atoms, the in-plane inversion asymmetry and the surface corrugation. Considering the surface state band structures of the Bi/Ag(111) and Pb/Ag(111), the main difference is the position of the Fermi level and the size of the spin splitting (see chapter 6 Figs. 28, 29 and 33 for the surface state band structures and Table 5 for the Rashba parameters). The difference in E_F is primarily a consequence of the different number of valence electrons. The smaller spin splitting in Pb/Ag(111) as compared to Bi/Ag(111) was argued to be mainly a consequence of the smaller surface corrugation.

In this section it will be shown that the surface state band structure of the $\mathrm{Bi}_x\mathrm{Pb}_{1-x}$/Ag(111) surface alloys can be continuously tuned by varying the stoichiometric

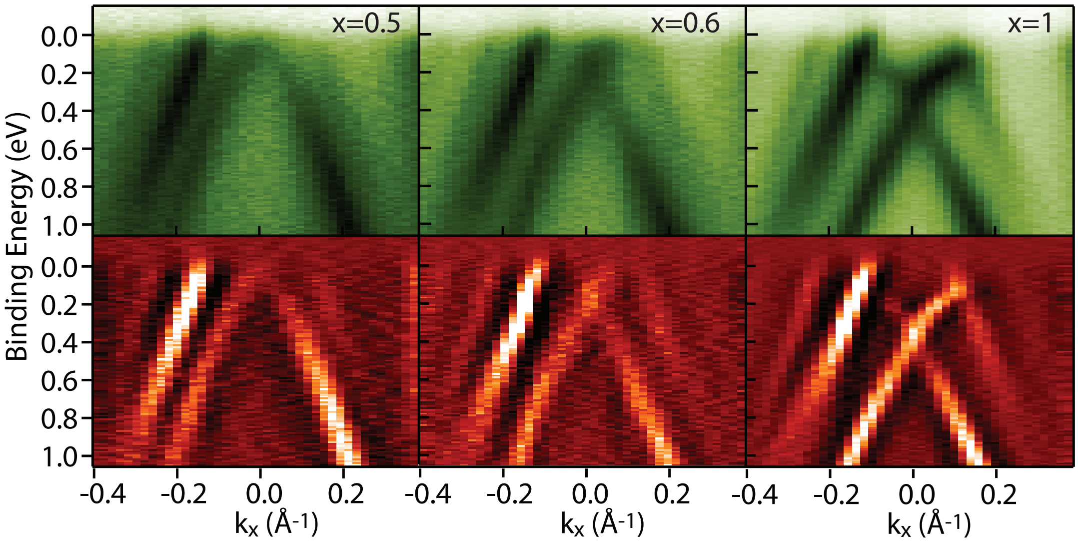

Figure 42: Upper graphs: Experimental band structure of $\mathrm{Bi}_x\mathrm{Pb}_{1-x}/\mathrm{Ag}(111)$ for $x = (0.5), (0.6)$ and (1) (from left to right) along the $\bar{\Gamma}\bar{K}$ direction, where dark corresponds to a higher photoemission intensity. Lower graphs: Second derivative data to enhance the contrast.

parameter x, as already pointed out in Ref. [109].

The experimental surface state band structure of $\mathrm{Bi}_x\mathrm{Pb}_{1-x}/\mathrm{Ag}(111)$ is shown in Fig. 42 along $\bar{\Gamma}\bar{K}$ for the stoichiometric parameters $x = (0.5), (0.6)$ and (1) measured with (spin-integrated) ARPES. Second derivative data are also shown to enhance the contrast. The Kramers pair $K1$ is fully occupied for $x = 1$ and, as x is decreased, the Fermi level shifts down with respect to the bands so that $K1$ gets depopulated, and the spin-splitting decreases. For $x = 0.6$, the Fermi level E_F lies between the band apex and the crossing point ($E_0 > E_F > E_{\bar{\Gamma}}$). In this regime the Fermi surface topology is changed (see chapter 3 Fig. 14) and unconventional Fermi surface spin textures are expected according to the Rashba model (see chapter 3 Eq. 31 and Fig. 13). At $x = 0.5$, the Fermi level lies approximately at the crossing point of $K1$, where the DOS of the inner Fermi contour vanishes. Note that here the calibration of x is slightly different from that given in Ref. [109]. However, this does not affect the conclusions of either work. It should be pointed out that the tunability of the surface state band structure and the absence of a superposition of the band structures of Bi/Ag(111) and Pb/Ag(111) clearly indicate that there is no formation of domains. LEED measurements show apart from the $(\sqrt{3} \times \sqrt{3})R30^\circ$ reconstruction no superstructure. The combination of these two findings indicates that Bi and Pb are randomly distributed.

In Fig. 43 the experimental spin-resolved MDCs for $x = 0.5$ (left column) and $x = 0.6$ (right column) are shown, providing us with the Fermi surface spin textures for $E_{\bar{\Gamma}} > E_F$

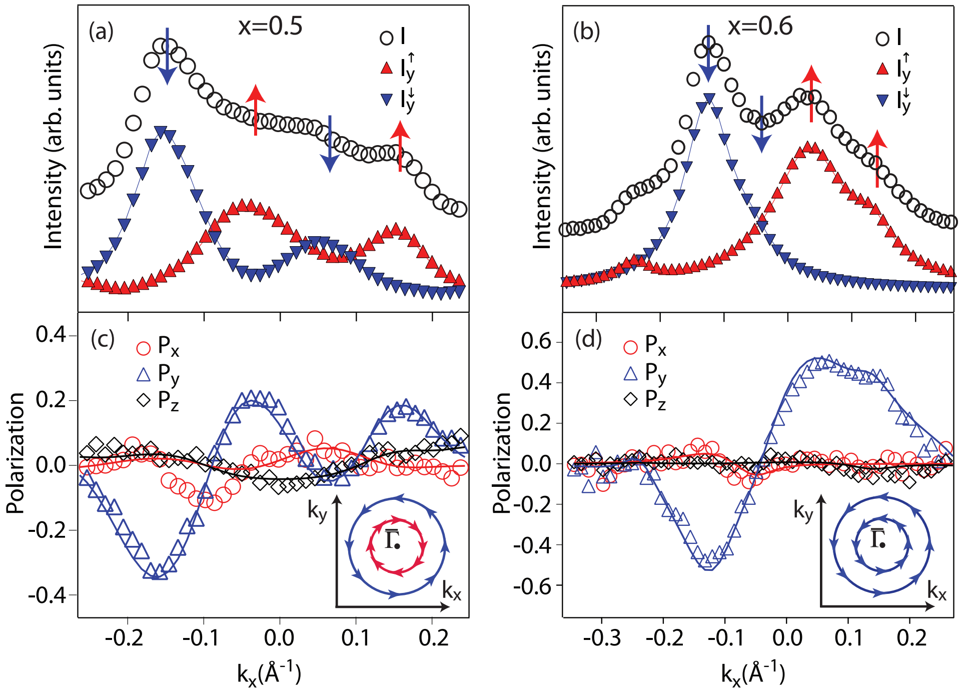

Figure 43: Spin-resolved ARPES data obtained at $E_b = 0.05$ eV of $Bi_xPb_{1-x}/Ag(111)$ for $x = 0.5$ (left) and $x = 0.6$ (right). (a) and (b) Total spin-integrated intensity (circles) and spin-resolved intensity curves projected on the y-axis of a MDC along $\bar{\Gamma}\bar{K}$. (c) and (d) are the corresponding measured (symbols) and fitted (solid lines) spin polarization data. (Insets) Schematically drawn Fermi surface spin textures. For $x = 0.6$, both bands of K1 crossing E_F between $\bar{\Gamma}$ and the SBZ boundary have parallel spin polarization vectors, while for $x = 0.5$, the spin polarization vectors are anti-parallel.

and $E_0 > E_F > E_{\bar{\Gamma}}$, respectively. The extraction of the spin polarization vectors $\boldsymbol{P}$ was done by applying the two-step fitting routine described in subsection 2.3.1 on the data of Fig. 43. For both compositions, it is found that the surface states $K1$ remain fully spin polarized with spin polarization vectors similar to those of the surface states of Bi/Ag(111) or Pb/Ag(111) found in section 6. The spin polarization vectors lie mainly in the surface plane and perpendicular to $\boldsymbol{k}_{||}$, and both the out-of-plane and radial spin polarization components are comparatively small. This finding is corroborated by several similar measurements in different crystallographic directions and at different binding energies. It is thus concluded that the spin polarization of the surface states K1 is robust against the mixing of Bi and Pb.

For $x = 0.5$, the measurement is performed slightly below the crossing point of $K1$. We observe the conventional situation, i.e., a straight cut from $\bar{\Gamma}$ to the surface Brillouin zone (SBZ) boundary crosses two bands with opposite spin polarization vectors. This can be seen in the spin-resolved spectra of Fig. 43 (a), which are obtained from the fits of the corresponding spin polarization data shown in Fig. 43 (c). The spin polarization vectors of the bands are opposite for all adjacent bands. The corresponding qualitative Fermi surface spin textures are drawn in the inset of Fig. 43 (c).

For $x = 0.6$, an unconventional Fermi surface spin texture is observed. Fitting the spin polarization data of Fig. 43 (d) clearly shows that, for positive and negative k_x, both bands crossing the Fermi energy have nearly parallel spin polarization vectors. The corresponding spin-resolved spectra are displayed in Fig. 43 (b). Due to strong transition matrix element effects, the inner band on the left side of normal emission is only visible as a weak shoulder of the $I_y^{\downarrow}$ curve. When $E_0 > E_F > E_{\bar{\Gamma}}$, the Fermi surface spin texture matches qualitatively that shown in the inset of Fig. 43 (d). A cut from $\bar{\Gamma}$ to the SBZ boundary crosses two bands with parallel spin polarization vectors.

To conclude this section, it was established that substitutional alloying does not alter the spin polarization vectors of the mixed Bi$_x$Pb$_{1-x}$/Ag(111) surface alloys. Furthermore, unconventional Fermi surface spin textures were realized through an adequate choice of the composition and were measured.

7.1.1 A Rashba-type spin filter

Intuitively, one could expect a spin-filtering effect due to the unconventional Fermi surface spin texture, since an arbitrary straight line from $\bar{\Gamma}$ towards the SBZ boundary cuts through states with identical spin polarization vectors, e.g. the two states with $k_x > 0$ and $k_y = 0$ have the same spin polarization vectors $\boldsymbol{P} = (0, 1, 0)$. However, it is the group velocity $\boldsymbol{v}^G = \hbar\,(\partial E/\partial \boldsymbol{k})$ which determines electronic transport and this remains the same for anti-parallel spin directions for both $E_F < E_{\bar{\Gamma}}$ and $E_0 > E_F > E_{\bar{\Gamma}}$ as shown by the arrows in Fig. 44 (b). Nevertheless, as will be shown in this section, the electronic transport across an ideal boundary separating a spin-degenerate two-dimensional electron gas from a Rashba system is spin polarized. The degree of spin polarization will be shown to be largest when $E_F = E_{\bar{\Gamma}}$ where the topological transition of the Fermi surface occurs.

In principle, a two-dimensional scattering geometry, as depicted in Fig. 44 (a), could be realized by the deposition of Bi$_x$Pb$_{1-x}$ on Ag(111) through a shadow mask. A spin-degenerate electron gas with an effective mass corresponding to that of Ag(111) surface states meets the states from the $K1$ manifold of Bi$_x$Pb$_{1-x}$/Ag(111) at the ideal one-dimensional boundary $x = 0$. It is imagined that a small current is driven through the boundary by the application of an infinitesimal voltage difference across the interface. The polarity of this applied voltage defines whether the charge current is from the left to the right, i.e., from the Ag(111) to the Rashba side, or from the right to the left, i.e.,

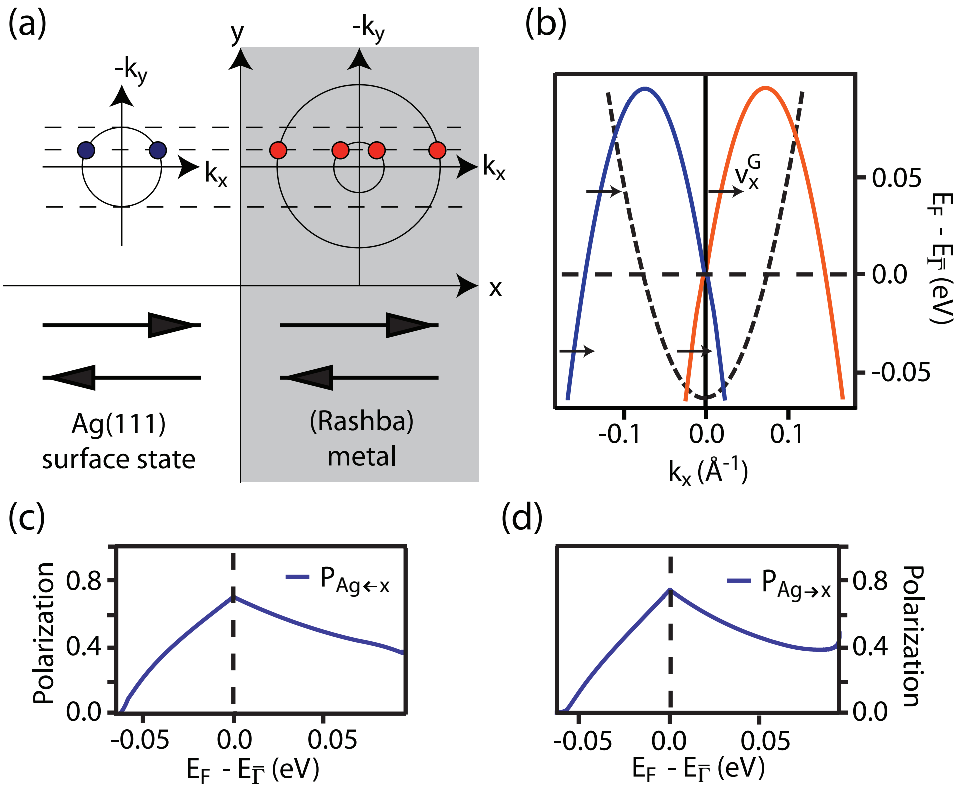

Figure 44: (a) Incoming and outgoing surface plane waves from the interface at $x = 0$ between a spin isotropic ($x < 0$) and a Rashba system ($x > 0$). (b) Dispersions of the Ag(111) and Rashba surface states. The arrows indicate the states with positive group velocities $v_x^G > 0$. (c) $P_{\mathrm{Ag}\leftarrow x}$ as a function of $E_F - E_{\bar{\Gamma}}$ as defined in the text. (d) $P_{\mathrm{Ag}\rightarrow x}$ as a function of $E_{\mathrm{F}} - E_{\bar{\Gamma}}$ as defined in the text.

from the RB to the Ag(111) side. The charge current is calculated from the reflection coefficients R_σ for an incoming surface state of energy E_F with spin quantum number σ along some quantization axis, which is here chosen to be the y-axis (see Ref. [128] for computational details).

The spin current is denoted by $P_{\mathrm{Ag}\rightarrow x}$ when the current is from the Ag(111) to the Rashba side or by $P_{\mathrm{Ag}\leftarrow x}$ otherwise. To quantify the transport of spin across the boundary the spin current, on the Ag(111) side, normal to the boundary (the difference between the spin up and spin down current) is divided by the particle current normal to the boundary, i.e. $P_{\mathrm{Ag}\leftrightarrow x} = (j_\uparrow - j_\downarrow)/j_{tot}$. The parameters $m^*_{\mathrm{Ag}}/m_e = 0.397$, $E_{\bar{\Gamma},\mathrm{Ag}} = -63$ meV are used on the Ag(111) side [7] and $m^*_x/m_e = -0.25$, $E_{0,x} = 94$ meV, $E_{\bar{\Gamma},x} = 0$, on the Rashba side [109]. The dispersions of Ag(111) and the Rashba system are shown in Fig. 44 (b).

The spin polarization curves of the currents $P_{\mathrm{Ag}\leftarrow x}$ and $P_{\mathrm{Ag}\rightarrow x}$ are plotted in Fig. 44 (c) and Fig. 44 (d), respectively, for different band fillings as described by the value of E_F.

In the absence of Rashba coupling, the spin current across the boundary vanishes. The breaking of the spin-rotation symmetry by the Rashba coupling induces a spin current on the Ag(111) side. This induced spin current is strongly enhanced by the onset of an unconventional Fermi surface spin textures due to the vanishing DOS ν_i of the inner constant energy contour. Thus, the Rashba metal acts as a spin injector or a spin acceptor depending on the polarity of the applied voltage difference across the boundary. Finally, even for non-ideal systems, such spin currents might lead to local spin accumulation that could be detected with spin polarized STM.

In correspondence to the above results, systems with strong Rashba type spin-orbit splitting and $E_F \approx E_{\bar{\Gamma}}$ are suggested to function as a spin filter. One could also envisage using materials with similar properties as spin injectors for other Rashba systems. This could reduce the problems encountered at interfaces to ferromagnets.

7.2 Tuning the spin splitting: $\mathrm{Bi}_x\mathrm{Sb}_{1-x}$/Ag(111)

In section 7.1 it was shown that the mixed surface alloys $\mathrm{Bi}_x\mathrm{Pb}_{1-x}$/Ag(111) allow for a coupled tunability of the Fermi level and the spin splitting. In order to get a fully tunable Rashba system, two stoichiometric parameters are needed. The admixture of Sb could in principle allow for a further tuning of the spin splitting, due to its smaller weight and lesser outward relaxation on Ag(111). Another step towards the realization of a ternary surface alloy would correspondingly be the realization of the mixed $\mathrm{Bi}_x\mathrm{Sb}_{1-x}$/Ag(111) surface alloy. However, while Bi and Pb are of similar size, the size difference between Bi and Sb is considerable. Moreover, Sb/Ag(111) can be grown in either *fcc* or *hcp* stacking and the surface corrugation of the *fcc* structure is much smaller for Sb/Ag(111) than for Bi/Ag(111). Due to these differences, it is not a priori clear whether well ordered $\mathrm{Bi}_x\mathrm{Sb}_{1-x}$/Ag(111) surface alloys can be formed. In the following it will be shown by means of IV-LEED as well as (S)ARPES that the binary $\mathrm{Bi}_x\mathrm{Sb}_{1-x}$/Ag(111) surface alloy can be formed with a well defined band structure depending on the stoichiometric parameter x.

In Fig. 45 $I(V)$ curves of an IV-LEED experiment for the mixed surface alloy $\mathrm{Bi}_x\mathrm{Sb}_{1-x}$/Ag(111) are shown for the the $(1,0)$, $(0,1)$ and the $(1/\sqrt{3}, 1/\sqrt{3})$ spots. It can be seen that the $I(V)$ curves evolve continuously as a function of x from the pure Sb/Ag(111) surface alloy ($x = 0$) with *fcc* top layer stacking to the Bi/Ag(111) surface alloy ($x = 1$), which proves the possibility to form this mixed alloy in a controlled way. In the individual LEED pictures, no additional superstructure could be observed, which gives an indication for a random distribution of Bi and Sb atoms, which could be corroborated with ARPES. Substitutional disorder in the mixed surface alloy $\mathrm{Bi}_x\mathrm{Sb}_{1-x}$/Ag(111) is further corroborated by an increase in the linewidth towards $x \approx 0.5$.

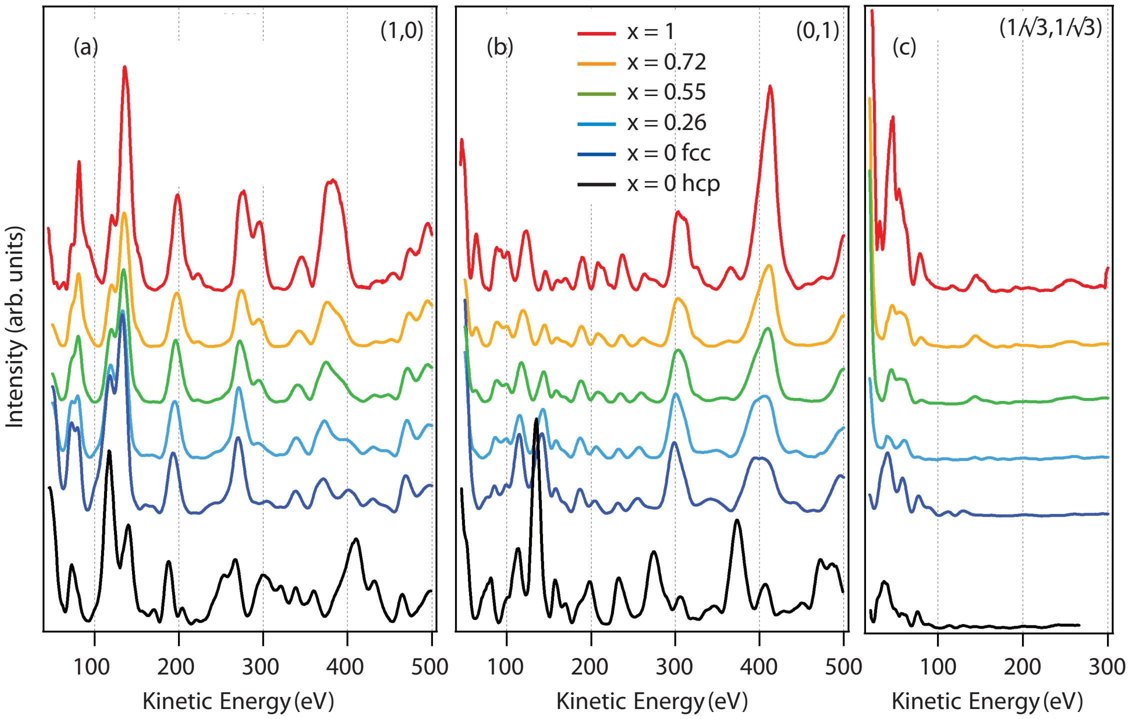

Figure 45: Low-energy electron diffraction from mixed Bi_xSb_{1-x} surface alloys. The $I(V)$ spectra represent the integrated intensities of the $(1,0)$ (a), $(0,1)$ (b) and $(1/\sqrt{3},1/\sqrt{3})$ (c) spots versus electron energy. The spectra evolve continuously between $x = 0$ (Sb/Ag(111) with fcc stacking, blue) and $x = 1$ (Bi/Ag(111), red). To exclude a possible *hcp* top-layer stacking, spectra for *hcp* stacked Sb/Ag(111) are displayed for comparison (black).

Fig. 46 (a) shows the evolution of the surface state band structure for the mixed binary alloy $Bi_xSb_{1-x}/Ag(111)$ as a function of the stoichiometry x measured with ARPES at a photon energy of 24 eV along $\bar{\Gamma}\bar{M}$. Second derivative data are shown in Fig. 46 (b). The spin splitting of the sp_z derived surface states of $K1$ evolves continuously between $x = 0$ and $x = 1$. Although the crossing point of the bands is not visible for most x, it can be concluded from the data that the energy $E_{\bar{\Gamma}}$ of the crossing point remains approximately constant.

For small x, the spin splitting is not resolved with spin-integrated ARPES. In this case, a precise determination of the size of the spin splitting can be done with SARPES. With the additional information of the spin polarization, SARPES is able to resolve very small spin splittings as shown in subsection 2.3.1. Spin-resolved ARPES data for $Bi_xSb_{1-x}/Ag(111)$ are shown in Fig. 47 for different Bi contents x, measured with a photon energy of 24 eV along $\bar{\Gamma}\bar{M}$. Fig. 47 (a) shows the spin-resolved intensities $I_y^{\uparrow}$

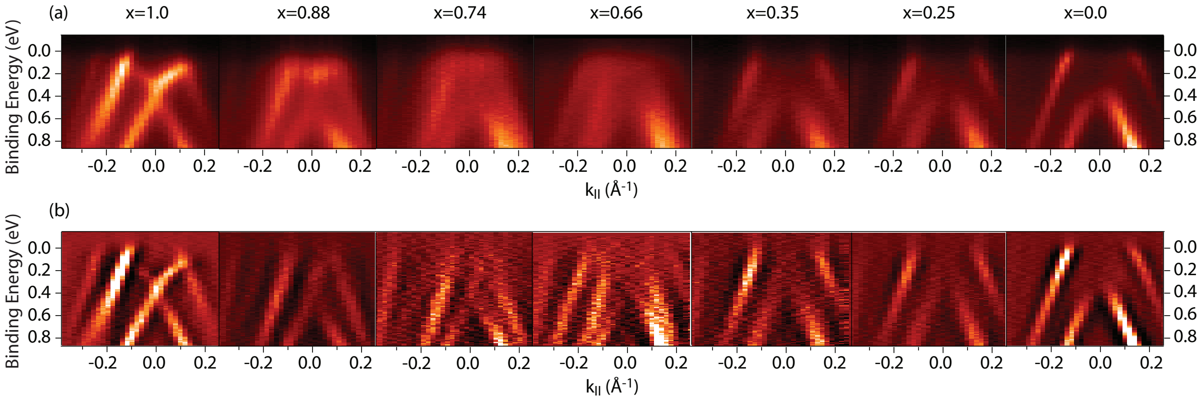

Figure 46: (a) Spin-integrated cuts through the SBZ along $\bar{\Gamma}\bar{M}$ for Bi$_x$Sb$_{1-x}$/Ag(111). (b) Second derivative data.

and $I_y^{\downarrow}$ as projected onto the y axis, which is the spin quantization axis for the states of $K1$. In Fig. 47 (b) the corresponding spin polarization data P_y are shown. As will be discussed in chapter 8, a spin state interference occurs in the photoemission process from Bi$_x$Sb$_{1-x}$/Ag(111) for small x, where the size of the spin splitting is in the order

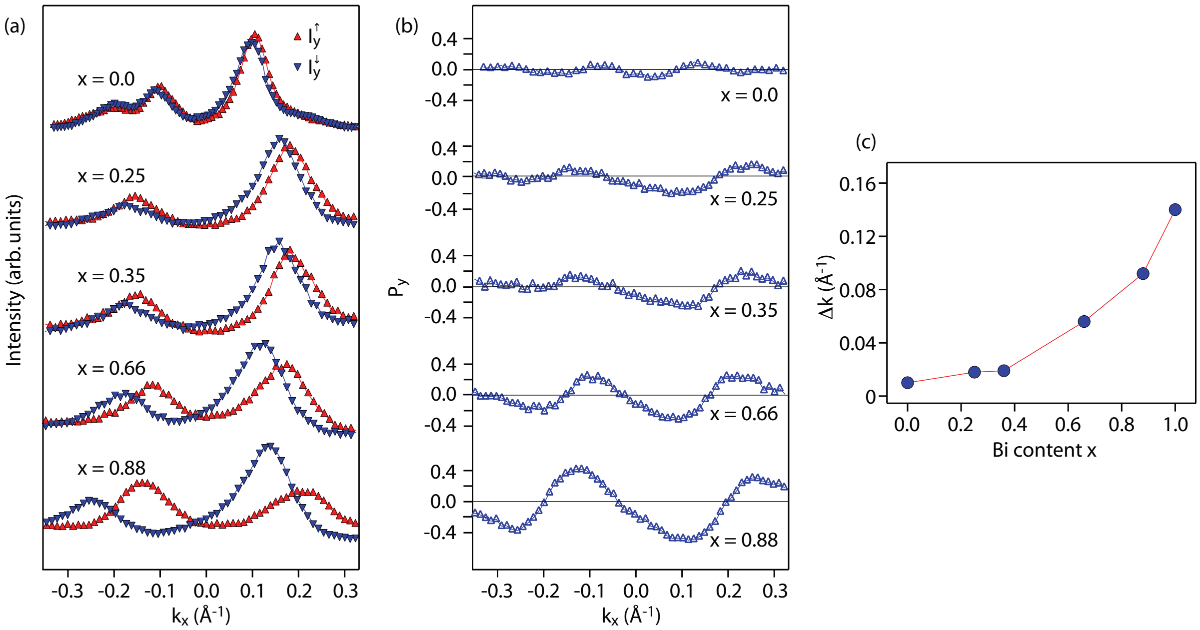

Figure 47: (a) Spin-resolved intensity data $I_y^{\uparrow}$ and $I_y^{\downarrow}$ of MDCs for Bi$_x$Sb$_{1-x}$/Ag(111) at $E_b = 0.6$ eV ($x = (0.0), (0.66)$) and $E_b = 0.9$ eV ($x = (0.25), (0.35)$ and (0.88)). (b) Corresponding spin polarization data P_y. (c) Momentum splitting Δk extracted from the data of (a).

of the intrinsic linewidth. This spin interference effect causes large spin polarization components P_x and P_z and can be well separated from the Rashba signal, which is along the y axis. Hence it does not hinder the determination of the size of the spin splitting Δk, which is plotted as a function of x in Fig. 47 (c). The value of Δk has been determined by fitting the spin-resolved intensities $I_y^{\uparrow}$ and $I_y^{\downarrow}$. Note that for small x the Rashba momentum is given by $k_R = \Delta k/2$, while for $x \gtrsim 0.4$ the dispersion of the surface states of $K1$ is non parabolic, which causes a systematic deviation, i.e. $k_R > \Delta k/2$. However, the SARPES data presented in Fig. 47 clearly proof the Rashba-type nature of the surface states of $Bi_xSb_{1-x}/Ag(111)$ and capture the continuous increase in the size of the Rashba effect as a function of x.

In summary, it was shown that the $Bi_xSb_{1-x}/Ag(111)$ surface alloys can be formed in a *fcc* phase. Moreover, its band structure is well defined and features a tunable spin splitting, while the position of the Fermi level remains approximately constant.

7.3 Proof of principle: $Bi_{0.3}Pb_{0.35}Sb_{0.35}/Ag(111)$

In sections 7.1 and 7.2 the existence of the two binary surface alloys $Bi_xPb_{1-x}/Ag(111)$ and $Bi_xSb_{1-x}/Ag(111)$, which feature a tunable well defined band structure, was established. While in $Bi_xPb_{1-x}/Ag(111)$ the region with $E_{\bar{\Gamma}} < E_F < E_0$ becomes accessible, $Bi_xSb_{1-x}/Ag(111)$ allows to tune the size of the spin splitting. As transport properties are determined by the spin texture of the Fermi surface it is of importance to tune both the position of the Fermi level as well as the size of the spin splitting independently. This could be achieved in a ternary $Bi_xPb_ySb_{1-x-y}/Ag(111)$ surface alloy as follows. In order to increase k_R one has to add heavy elements with a large outward relaxation (i.e. Bi, Pb). For a modification of E_F, $Bi_xSb_{1-x}/Ag(111)$ should be mixed with Pb. In this section we will show the existence of this ternary $Bi_xPb_ySb_{1-x-y}/Ag(111)$ surface alloy for $x = 0.3$ and $y = 0.35$ as a proof of principle.

In Fig. 48 (a) the experimental surface state band structure of $Bi_{0.3}Pb_{0.35}Sb_{0.35}/Ag(111)$ is shown as measured with ARPES. In comparison with the binary surface alloys $Bi_xPb_{1-x}/Ag(111)$ and $Bi_xSb_{1-x}/Ag(111)$, the photoemission intensity is weak and the bands are broad. It is assumed that this is partly caused by the disorder intrinsic to the ternary surface alloy and partly by the non-optimized sample preparation (for details concerning the sample preparation see section 5.1). Due to the large linewidth of the bands, the splitting of the Kramers pair $K1$ visible in Fig. 48 (a) is not resolved.

In order to confirm the spin-split nature of the surface states of $Bi_{0.3}Pb_{0.35}Sb_{0.35}/Ag(111)$ a SAPRES measurement has been carried out. The spin-resolved intensities $I_y^{\uparrow}$ and $I_y^{\downarrow}$ of a MDC recorded at a binding energy of 0.6 eV along $\bar{\Gamma}\bar{M}$ are shown in the upper panel of Fig. 48 (b) and the corresponding spin polarization data P_y are shown in the lower

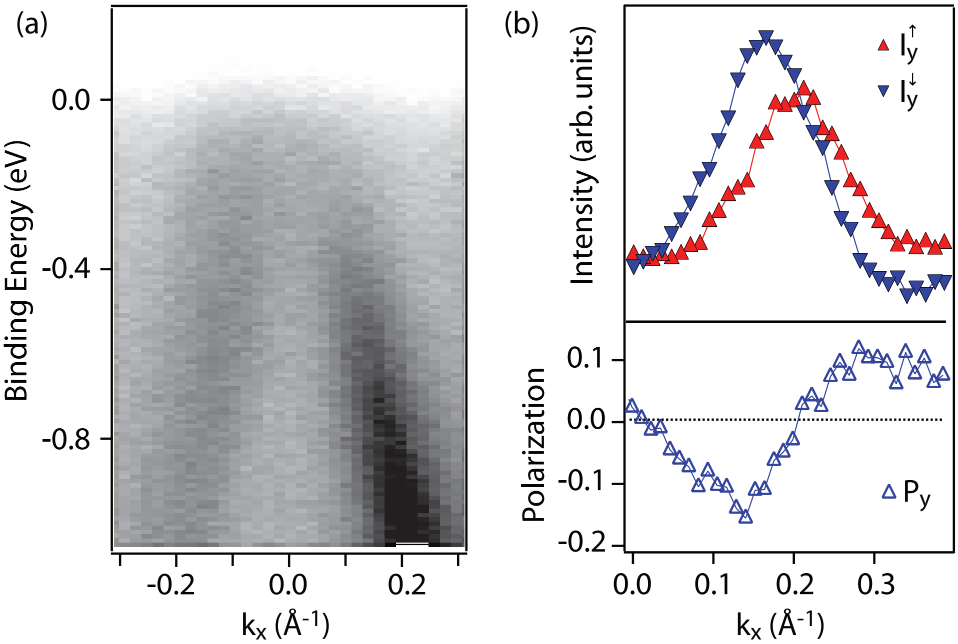

Figure 48: (a) Spin-integrated cut through the SBZ along $\bar{\Gamma}\bar{M}$ for Bi$_{0.3}$Pb$_{0.35}$Sb$_{0.35}$/Ag(111). (b) (top) Spin-resolved intensity data $I_y^\uparrow$ and $I_y^\downarrow$ of a MDC at $E_b = 0.6$ eV and (bottom) corresponding spin polarization data P_y.

panel of Fig. 48 (b). In the spin-resolved intensities two distinct peaks are visible. These peaks belong to the bands $r1$ and $r2$ of $K1$ and the spin polarization component along the y axis is opposite for $r1$ and $r2$, in agreement with a Rashba-type spin splitting. The momentum splitting between $r1$ and $r2$ obtained from fitting the spin-resolved intensity curves is $\Delta k = 0.038$ Å^{-1} and correspondingly $k_R = 0.019$ Å^{-1}. This is about a factor of two smaller than what could be expected by considering the momentum splittings in the individual pure surface alloys and their weighted sum.

Summarizing it was shown that it is possible to form the ternary surface alloy Bi$_x$Pb$_y$Sb$_{1-x-y}$/Ag(111). This finding and the fact that the binary surface alloys Bi$_x$Pb$_{1-x}$/Ag(111) and Bi$_x$Sb$_{1-x}$/Ag(111) can be formed for arbitrary x justifies the assumption that it is possible to form the ternary surface alloy for arbitrary x and y, which yields a fully tunable Rashba system.

The following chapter is a modified version of the manuscript of:
F. Meier, V. Petrov, H. Mirhosseini, L. Patthey, J. Henk, J. Osterwalder, and J. H. Dil, *Interference of spin states in photoemission from Sb/Ag(111) surface alloys* (2010), Journal of Physics: Condensed Matter, **23**, 072207 (2011).

8 Interference of spin states in photoemission from Sb/Ag(111) surface alloys

Using a three-dimensional spin polarimeter we have gathered evidence for the interference of spin states in photoemission from the surface alloy Sb/Ag(111). This system features a small Rashba-type spin splitting of a size comparable to the momentum broadening of the quasiparticles, thus causing an intrinsic overlap between states with orthogonal spinors. Besides a small spin polarization caused by the spin splitting, we observe a large spin polarization component in the plane normal to the quantization axis of the Rashba effect. Strongly suggestive of coherent spin rotation, this effect is largely independent of the photon energy and photon polarization.

An important branch of spintronics research is looking for new systems with naturally existing spin-polarized electrons and ways to manipulate their spins. The broken spatial inversion symmetry at surfaces can induce a spin splitting of electronic states in non-magnetic systems via the spin-orbit interaction. A substantial splitting due to this so-called Rashba effect [91] was observed for the Shockley surface state on Au(111) by angle-resolved photoemission spectroscopy (ARPES) [6]. Later spin-resolved experiments confirmed the high degree of spin polarization of the electrons photoemitted from these states [9], observing helical spin structures tangential to the two spin-split Fermi surfaces. More recently, surface alloys of Bi and Pb on Ag(111) have attracted much attention in the search for even larger spin splittings, exploiting a combination of strong atomic spin-orbit interaction of the heavy metals with structural effects enhancing the local potential gradients at the surface [102, 123].

In this Letter we discuss the structurally related system of Sb on Ag(111) which has a small but finite spin splitting [119]. The splitting is so small that it cannot be resolved by ARPES in most of the surface Brillouin zone. Our spin-polarized ARPES data show nevertheless substantial spin polarization and permit to quantify the spin splitting. More importantly, the measured spin texture is at strong variance with that expected from the Rashba model and suggests that coherent superposition of spin states occur in the photocurrent. We speculate that this effect is also likely to occur in other experimental probes involving electronic excitations, like for example transport measurements.

Spin-state interference is an intriguing property of quantum mechanics. For instance, an electron with its spin along the positive z axis can be represented by two spinors with spins along the y axis, reading $\sqrt{2} \cdot \langle z^{\uparrow}| = (1, 1) = (1, 0) + (0, 1) = \langle y^{\uparrow}| + \langle y^{\downarrow}|$. Similarly, a spin along x can be written as $\sqrt{2} \cdot \langle x^{\uparrow}| = (1, -i) = \langle y^{\uparrow}| + e^{i3\pi/2}\langle y^{\downarrow}|$. A phase difference between $\langle y^{\uparrow}|$ and $\langle y^{\downarrow}|$ causes a rotation of the resulting spin polarization vector in the xz plane. As a consequence, the expectation value of the sum of two spinors can differ from the sum of the individual expectation values. In particular, the addition of a spin-up and a spin-down spinor along some quantization axis does not yield zero polarization, but results in a spinor with an expectation value (henceforth spin polarization) placed within the plane orthogonal to the quantization axis. This is exactly what we observe.

Spin-state interference has previously been observed in resonant photoemission induced by circularly polarized light from magnetized Gd by Müller et al. [81]. In this system, orthogonal spin states can be prepared by the angular momentum transfer from the light and spin-orbit interaction on one hand, and by direct photoemission from magnetized states in the valence band on the other hand. By tuning the photon energy to the 4d resonance, the two spin states can be brought to interfere.

In our case it is the Rashba effect that defines the two orthogonal spin states. Without interactions, but with experimental broadening the polarization curves will resemble those in Fig. 49 (a). However, these states can interfere when their momentum splitting is of the same order as the intrinsic line width of either state such that they overlap, as is illustrated in Fig. 49 (b). The intrinsic line width in photoemission is a consequence of manybody effects of the photohole left behind, which forms, dressed with electron-electron, electron-phonon and electron-defect scattering processes, a quasiparticle [33]. While electron-electron and electron-phonon coupling are inelastic processes, electron-defect scattering is an elastic process and as such preserves the phase relation. In alloy systems, this is expected to be the dominant broadening mechanism. Because the quasiparticles in the overlapping region of the two spin-split bands are indistinguishable in time and space, photoelectrons in this region carry away coherent superpositions in spin space.

Like in the related Bi and Pb surface alloys on Ag(111), the Sb adatoms replace every third Ag atom in the topmost layer to form a $(\sqrt{3} \times \sqrt{3})R30^{\circ}$ superstructure [114, 117], henceforth termed Sb/Ag(111). We also investigated mixed $\mathrm{Sb}_{1-x}\mathrm{Bi}_{x}$/Ag(111) layers, where Sb is randomly substituted by Bi. In such mixed alloys the spin splitting can be tuned [109, 125], and they can therefore serve as a test for our overlap hypothesis. Finally, we performed photoemission experiments with different photon energies and photon polarization in order to probe the dependence of the spin state interference on these parameters.

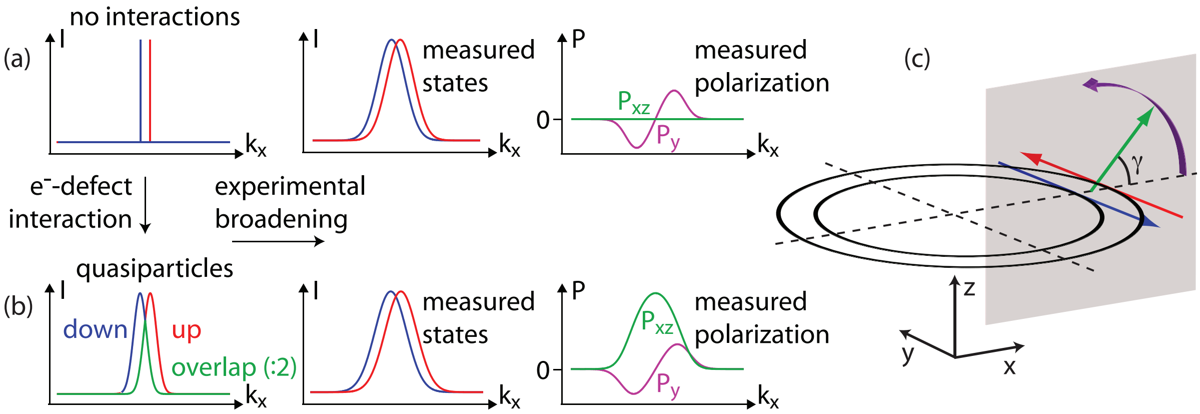

Figure 49: (color online) Schematic illustration of the suggested mechanism leading to spin polarization in the xz-plane by spin-state interference. A small spin-splitting of Rashba-type eigenstates without (a) and with (b) interaction leads with experimental broadening to very similar spin-integrated data. The resulting polarization spectra are different; for both a Rashba-type spin polarization along the y direction (violet/dark gray curve) is expected, and for (b) a coherently rotated spin polarization within the xz-plane (green/light gray curve). (c) Illustration of the associated spin polarization vectors in one region of the spin-split circular Fermi surface.

The spin-polarized ARPES (SARPES) experiments were performed at room temperature at the Swiss Light Source using the COPHEE spectrometer. [59] The energy and angle resolution when measured with the Mott detectors was 80 meV and ± 0.75°, respectively. The photoemission setup is schematically shown in Fig. 50 (a). There is a 45° angle between the incoming photons and the detected electrons. The z axis is given by the sample normal and the sample is rotated around the y axis. In a momentum distribution curve (MDC) this corresponds to a scan along the k_x axis with $k_y = 0$ as shown in Fig. 50 (a) for schematically drawn circular constant energy surfaces.

In Fig. 50 (b) we show the spin-integrated surface state band dispersion of the Sb/Ag(111) surface alloy around the surface Brillouin zone center $\bar{\Gamma}$ measured along the high symmetry direction $\bar{\Gamma}\bar{M}$. Similar to the two related surface alloys Bi/Ag(111) and Pb/Ag(111) [102, 123, 124], two sets of bands are observed. The inner set of bands consists of electrons with mainly sp_z like orbital character while the outer set of bands has primarily p_{xy} orbital character. However, the Rashba-type spin splitting is here much smaller and is not resolved in the data of Fig. 50 (b). The smaller splitting can be understood as a consequence of the smaller atomic number Z of Sb ($Z = 51$) compared to Bi (83) and Pb (82) and a smaller surface corrugation [87, 110, 119].

Bi/Ag(111) and Pb/Ag(111) show Rashba-type spin structures [124], i.e. the spin polar-

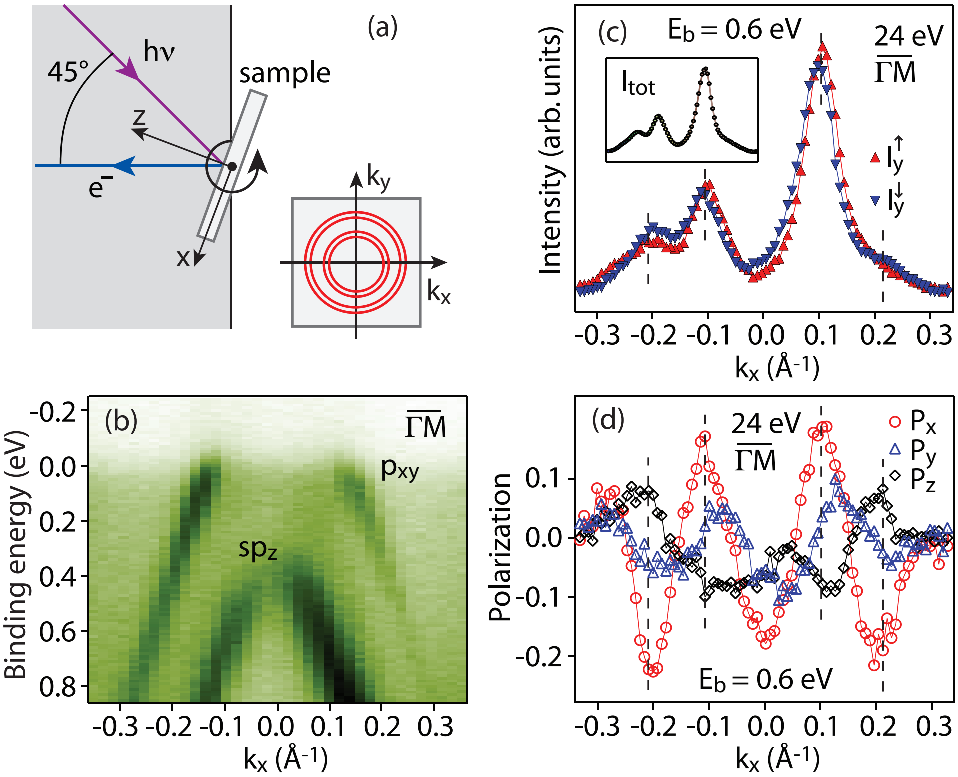

Figure 50: (color online) (a) Schematic experimental setup. (b) Spin-integrated surface state band structure of the Sb/Ag(111) surface alloy around $\bar{\Gamma}$. (c) Spin-resolved and spin-integrated (inset) MDC intensity data for 24 eV photons in the direction $\bar{\Gamma}\bar{M}$ at $E_b = 0.6$ eV. (d) Simultaneously obtained spin polarization curves for all three components. Dotted lines are guides to the eye. The momentum region between 0 and 0.2 Å^{-1} corresponds to Fig. 49.

ization is mainly in plane and orthogonal to the electron momentum (P_y component). In Fig. 50 (d) we present spin polarization data obtained for Sb/Ag(111) at a binding energy $E_b = 0.6$ eV with p-polarized photons of 24 eV (i.e. light polarization in the xz plane). Here, the spin polarization component P_x is dominant, corresponding to the radial direction of the constant energy surfaces. It shows large modulation amplitudes *centered* at the peak positions of the MDCs. This is in sharp contrast to the other systems [105] and represents a major deviation from the Rashba model. P_y and P_z components show modulations with smaller amplitudes, with those in P_z being rather in antiphase with those in P_x. On the other hand, P_y crosses zero at the peak centers, which is typical of Rashba-type behaviour [124]. From this latter curve we can produce the spin-resolved spectra as projected onto the y axis [129], which corresponds to the spin quantization axis in the Rashba model (Fig. 50 (c)). The spin-resolved MDCs $I_y^{\uparrow}$ and $I_y^{\downarrow}$ show a clear signature of a Rashba-type spin-orbit splitting with a momentum shift $\Delta k = 2k_R \cong 0.01$

Å^{-1} between the two bands (as obtained from fitting the two main peaks).

Another remarkable observation in these data is that the measured spin polarization curves violate time reversal symmetry. According to this symmetry, the two spin-split partners of the Kramers pairs should have opposite spin polarization vectors for equivalent binding energies, i.e. $\boldsymbol{P}(\boldsymbol{k}_{\|}) = -\boldsymbol{P}(-\boldsymbol{k}_{\|})$. Yet, the polarization curves P_x and P_z are symmetric with respect to $k_x = 0$. The missing time reversal symmetry is a strong indication of a photoemission related effect, since time reversal symmetry has to hold for the initial-state wave functions. We suggest that the origin of this photoemission effect is the spin-state interference caused by the coherent part of the intrinsic overlap in each Kramers pair associated with the small spin splitting. Hence similar effects can be expected for other systems with small spin splittings.

The model illustrated in Fig. 49 can now directly be applied to the case of Sb/Ag(111). Here, the states are split by $2k_R \cong 0.01$ Å^{-1} and the spinor of each state is well defined due to the Rashba effect, termed up and down on the left of Fig. 49 (b). There is a large *intrinsic* overlap between the two peaks if the momentum broadening is in the order of 0.01 Å^{-1}, which translates to 40 meV energy broadening considering the dispersion. We emphasize again that the phases of the photohole spin states have to be conserved in the many-body interactions, which is the case for momentum broadening due to electron-defect scattering. We were not able to measure the intrinsic line width due to experimental limitations, however for the surface state of the highly perfect Cu(111) surface about 1/3 of the line-width broadening (23 meV) is caused by defects, [7] and for the Al(100) surface state the line-width broadening due to electron-defect scattering is 101 meV. [36] Considering that the Sb/Ag(111) alloy surface has certainly a higher concentration of defects and disorder than the Cu(111) surface due to the nature of the substitutional alloy, [34] it is fair to assume that a significant amount of the broadening is caused by coherent electron-defect scattering. Hence a majority of the photoelectrons in the overlap region represent coherent superpositions of spin up and spin down states.

The peaks can then be divided in regions with purely spin up, purely spin down and an overlap region in order to obtain the scenario shown in Fig. 49 (b). Considering that the coherent addition of two orthogonal spinors has a spin polarization vector in the plane normal to the spin polarization of the initial spinors as shown in Fig. 49 (c), spin polarization curves like the rightmost of Fig. 49 (b) are obtained, provided that the relative phases remain constant across the overlap region. In particular, the spin polarization of the overlap region has components P_{xz} with their maxima at the point of maximum overlap, i.e. centered on the MDC peak. This is exactly what is found in the experiment as shown in Fig. 50 (d). The direction of the spin polarization in the xz plane, described by the angle γ, is defined by the phase difference between the

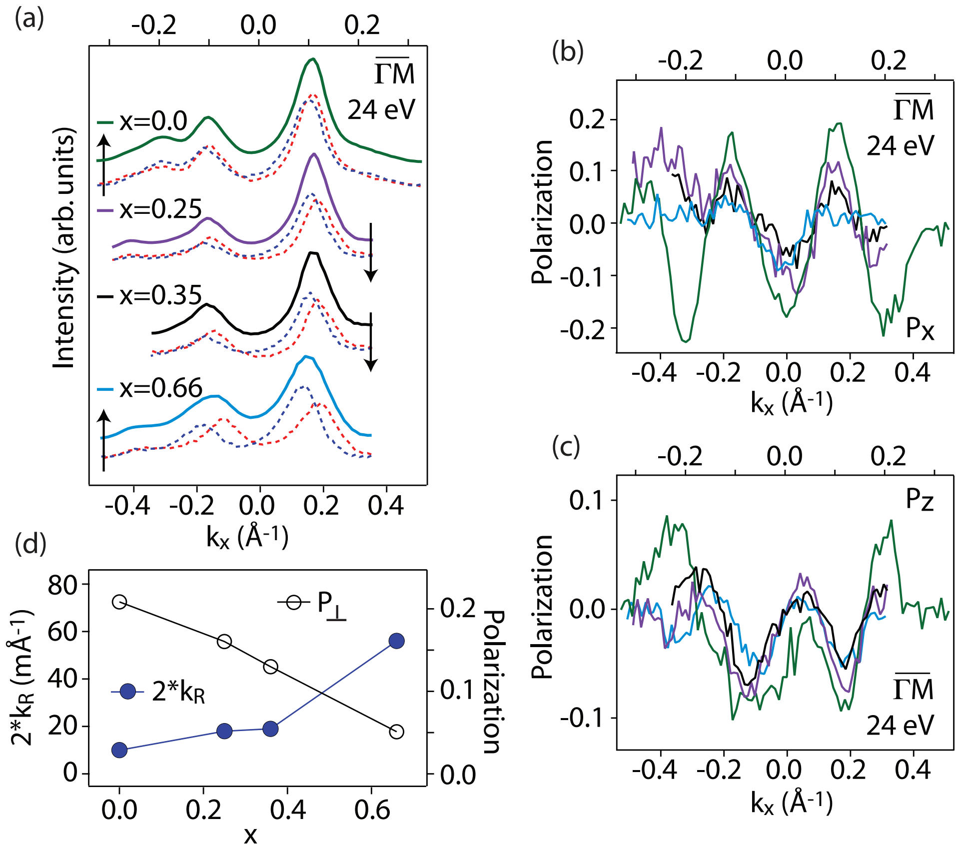

Figure 51: (color online) (a) Spin-integrated MDC data (solid lines) of $\mathrm{Sb}_{1-x}\mathrm{Bi}_x/\mathrm{Ag}(111)$ for $x = 0$, 0.25, 0.35 and 0.66 at $E_b = 0.6$ eV ($x = 0$ and $x = 0.66$) and 0.9 eV ($x = 0.25$ and 0.35). Dashed lines show the corresponding spin resolved intensity data. For better comparison, the k_x scale for the $x = 0$ and $x = 0.66$ samples is given on the upper side of the frame, while the scale for $x = 0.25$ and 0.35 samples is given on the lower side . The arrows refer to the corresponding k_x scale. (b) and (c) Spin polarization data P_x and P_z corresponding to the same samples as in (a). Note again the different $\boldsymbol{k}$-scales. (d) Spin splitting (full circles) and spin polarization $P_\perp$ (open circles) for different intermixing coefficients x.

two orthogonal spin states of the Kramers pair. From the observation that the P_x and P_z curves are symmetric with respect to $k_x = 0$ Å^{-1} (Fig. 50 (d)), we conclude that corresponding states of opposite k_x have equal spin rotation angles. For the sp_z states we measure $\gamma = 22° \pm 9°$, for the p_{xy} states the value is $-25° \pm 10°$. We can only speculate on which parameters define the phase difference between spin-up and spin-down states. Likely candidates are the symmetries of initial and final states, and the geometry of the photoemission experiment, i.e. the angle between light incidence and eletron detection.

In Fig. 51 we show SARPES data for $\mathrm{Sb}_{1-x}\mathrm{Bi}_x$ for $x = 0, 0.25, 0.35$ and 0.66. From fitting

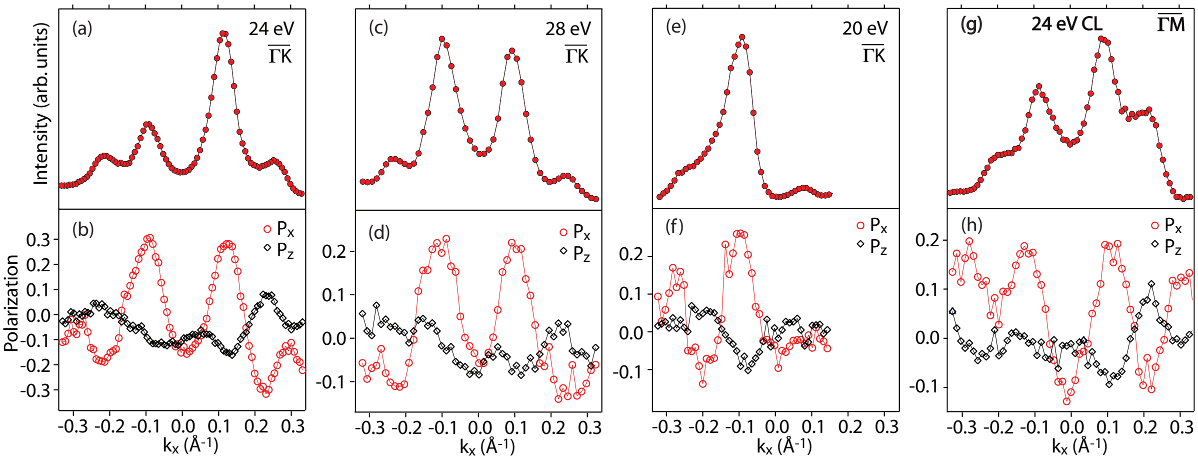

Figure 52: (color online) SARPES data for Sb/Ag(111) at $E_b = 0.6$ eV for different photon energies and light polarization. (a), (c) and (e) MDC intensity data along $\bar{\Gamma}K$ for p-polarized light with photon energies of 24 eV, 28 eV and 20 eV, respectively. (b), (d) and (f) Corresponding spin polarization data. (g) MDC intensity data along $\bar{\Gamma}M$ for circular left polarized light with $h\nu = 24$ eV. (h) Spin polarization data corresponding to (g).

the spin-resolved intensity curves $I_y^{\uparrow}$ and $I_{y,}^{\downarrow}$ (red and blue dashed lines, respectively) shown in Fig. 51 (a) we find that the spin splitting increases from $2k_R = 0.01$ for $x = 0$ to $2k_R = 0.056$ for $x = 0.66$ (Fig. 51 (d)). The amplitudes of the spin polarization curves P_x and P_z (Fig. 51 (b) and (c)) decrease markedly as the spin splitting increases. The spin rotation angle in the xz plane is not strongly affected by the increased spin splitting. Deviations in the rotation angle are within the experimental accuracy. The values $P_\perp = (P_x^2 + p_y^2)^{1/2}$ for the different mixing ratios x taken at the peak positions are shown in Fig. 51 (d). We thus observe a decrease in the measured spin polarization in the plane normal to the spin quantization axis of the quasiparticles as their splitting gets larger and the intrinsic overlap is reduced. This is fully in line with our model.

Spin polarization observed in photoemission data can have various other origins [74–80], but the outcome depends strongly on the symmetry of the solid and of the particular surface, on photon energy as well as on the absolute directions of photon incidence, photon polarization and electron emission. In order to rule out such effects, we have measured SARPES MDC data for Sb/Ag(111) at a binding energy of 0.6 eV for different photon energies and different light polarizations (Fig. 52). With respect to Fig. 50, the sample has been rotated by 90° and the MDCs are thus along $\bar{\Gamma}\bar{K}$ for Fig. 52 (a)-(f), while (g) and (h) show again a scan along $\bar{\Gamma}\bar{M}$. The upper panels show the MDC intensity data, the lower ones the corresponding spin polarization curves. We observe that the effect is quite robust against variations of these experimental parameters. First, the sample rotation of 90° has no significant influence on the spin polarization curves (Fig. 50 (d) vs. Fig. 52 (b)), in contrast to the effects described by Tamura et al. [74] Note that the positions of the outer peaks change slightly due to a hexagonal distortion of their constant energy surface [119]. Second, although the intensity distribution curves change as a function of the photon energy, the spin polarization features are qualitatively not affected. The local extrema for P_x (P_z) are always centered on the peaks, and are positive (negative) for the inner and negative (positive) for the outer ones. The absence of a photon energy dependence (Fig. 52 (b), (d) and (f)) rules out a strong contribution of spin-orbit coupling in the final states to the observed phenomenon. Most striking is the finding that a change from p-polarized to circular left polarized light (Fig. 50 (d) vs. Fig. 52 (h)) has no significant effect on the measured spin polarization curves. Additionally, the spin polarization measured in MDC's is in agreement with the spin polarization measured in energy distribution curves, which excludes changes in the measurement geometry as the cause. This corroborates the hypothesis that the measured P_x and P_z spin polarization is dominated by the spin structure of the initial states.

We performed fully relativistic spin-resolved one-step photoemission calculations for Sb/Ag(111), with p-polarized and circular left polarized light using the experimental geometry. Fig. 53 (a) shows the (spin-integrated) intensities for these two light polarizations. The two strong peaks nearest to $k_x = \pm 0.1$ Å^{-1} represent emission from sp_z states, while the split peaks at $|k_x| > 0.2$ Å^{-1} are due to p_{xy} emission. Fig. 53 (b) shows the spin polarization curves P_x and P_z for p-polarized light. While the curve for P_y is in good agreement with the experimental data (see Fig. 53 (d)), there is neither quantitative nor qualitative agreement for the polarization curves in the xy plane (cf. Fig. 50 (d)). The experimental spin polarization amplitudes are larger and the shapes of the curves are very different. A change of the photon polarization to circular left leads to drastic changes in the predicted spin polarization curves as shown in Fig. 53 (c), which is in contrast to the experiment.

In general such calculations are in good agreement with the experimental data [80]. The dramatic failure in the present case for P_x and P_z indicates that an important ingredient is missing in the theoretical description. Specifically, the calculations do not capture coherent initial state effects as the quasiparticles are described by a non-local spectral density, which is an incoherent superposition of initial states. Hence, the disagreement between the data shown in Fig. 53 (b) and (c) and the curves in Fig. 50 (d) (in chapter 8) also hints at a coherent effect in the initial states.

Our results should not be confused with the findings of Sakamoto et al. for the Rashba

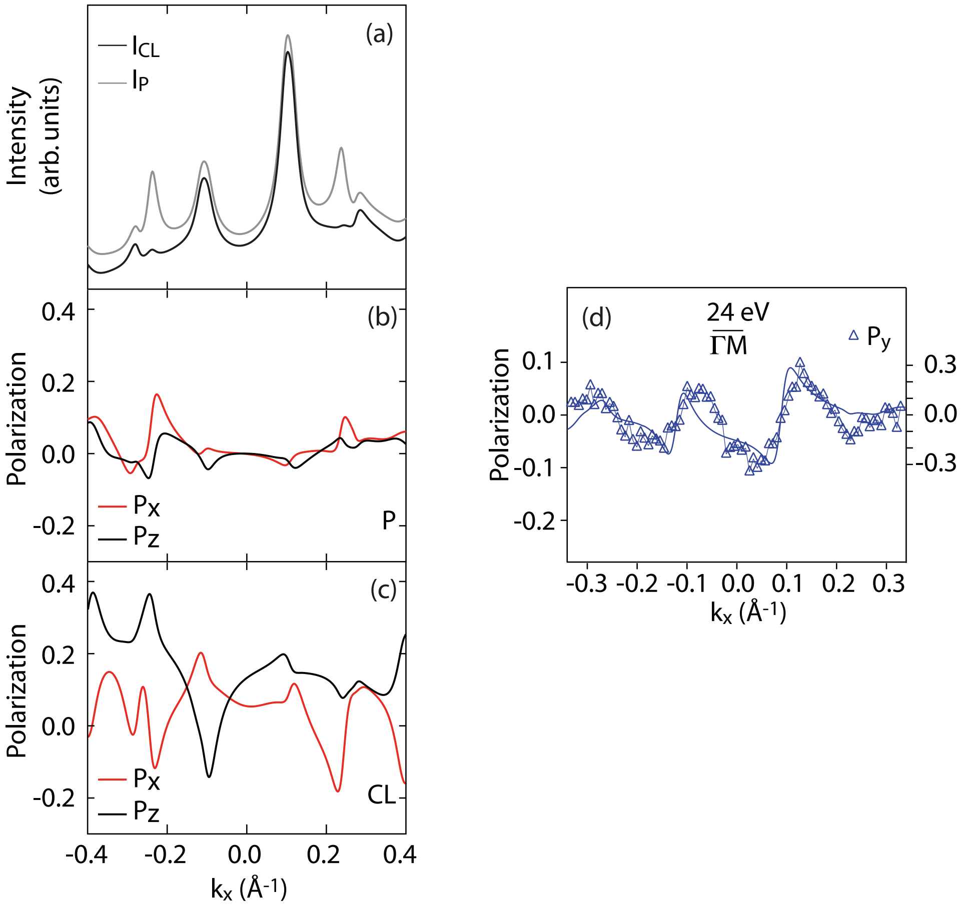

Figure 53: Fully relativistic spin-resolved one-step photoemission calculations for Sb/Ag(111) at $E_b = 0.6$ eV and $hv = 21.2$ eV. (a) The total (spin-integrated) photoemission intensity for p-polarized (I_P) and for circular left polarized light (I_{CL}). Spin polarization curves P_x and P_z for (b) p-polarized and (c) circular left polarized light. (d) Comparison of the experimental and the theoretical spin polarization curves P_y. Apart from the difference in the scale, the curves are in very good agreement.

system Tl/Si(111) [130], where the spin polarization is forced out-of-plane at the $\bar{K}$ points of the surface Brillouin zone due to a frustration effect. Deviations from pure in-plane (P_y) spin polarization can also be caused by local in-plane potential gradients. However, in both cases the states are split and the spins remain paired [102, 124].

Spin-state interference has recently been predicted for photoemission from the π states of graphene [131], where photoelectrons from equivalent atoms within the same unit cell interfere. The authors describe this effect as an interference between spin and pseudospin. In contrast, for Sb/Ag(111), the interference stems from a partly coherent intrinsic overlap in $\boldsymbol{k}$ space.

In summary, we have presented evidence for a coherent superposition of spin states in photoemission from a Rashba system. Interference is assigned to a region in $\boldsymbol{k}$ space where spin-up and spin-down states overlap. Hence the measured spin polarization is defined by the photohole quasiparticles and is not significantly modified by final state effects in the photoelectron channel. In condensed matter physics many experiments involve electronic excitations in systems with spin-split states. Similar to the photoemission process described in our work, electron and hole quasiparticles are formed. Specifically, elastic scattering processes should lead to momentum broadening. If this broadening is comparable to the spin-splitting, the resulting spin polarization might not behave as expected. Spin-state interference may thus be a more general phenomenon.

Fruitful discussions with T. Greber, M. Hengsberger, M. Haverkort, U. Heinzmann, B. Slomski, C. R. Ast and I. Gierz are gratefully acknowledged. We thank C. Hess, F. Dubi, and M. Klöckner for technical support. This work is supported by the Swiss National Foundation.

9 Conclusions and Outlook

The two-step fitting routine allows to access the spin polarization vectors of the individual bands. This is particularly useful in systems with non-collinear spins or small spin splittings. The benefit of this procedure is that it can separate the contributions from the individual states and the inelastic scattered background, as exemplified by the analysis of SARPES data obtained from the surface states of the surface alloys on Ag(111). However, currently the analysis of SARPES data still mainly consists of the study of spin-resolved intensities projected on some axis, often at variance with the quantization axis. Assuming fully spin polarized initial states, which is reasonable for a large variety of systems, the two-step fitting routine can also be applied to data where only two components of the spin polarization are measured, making it useful for many different SARPES setups. It is expected that the two-step fitting routine or similar types of data analysis routines will become standard in the data evaluation process and yield more detailed information on the spin structure.

Considering the surface alloys formed by Bi, Pb and Sb on Ag(111), it was shown with the use of the two-step fitting routine that its surface states are fully spin polarized and that for some states the spin polarization vector is rotated out of the surface plane. Both the size of the spin splitting and the out-of-plane spin polarization component can be understood by considering the surface state wave function, and it is discussed that it is the asymmetry of the wave function in the vicinity of the nuclei which determines the Rashba-type spin splitting. The size of the spin splitting is strongly increased due to the outward relaxation of the alloy atoms, which increases the asymmetry of the surface state wave function in the direction perpendicular to the surface. The spin splitting is further enhanced by the in-plane structural asymmetry, which additionally causes the out-of-plane rotation of the spin polarization vector. The influence of the surface corrugation and the in-plane SIA clearly demonstrate the importance of the crystal structure for the Rashba effect. This provides a basis for future research where the aim is to tailor the band and spin structure of Rashba systems. In fact it was shown that by creating a mixture of the different alloy atoms Bi, Pb and Sb that it is possible to adjust both the position of the Fermi level and the size of the spin splitting. Similar strategies could yield a control of the size of the spin splitting and the spin structure in many other systems.

The surface alloys studied in this thesis consist of comparably heavy alloy atoms on a substrate consisting of lighter atoms. It would be of particular interest to study the inverted scenario, i.e. comparably light alloy atoms on the surface of a crystal consisting of high Z elements. Unfortunately, the surface of a Pb crystal features no surface state, Bi crystallizes in a different structure as compared to Ag and Au(111) seems to hinder a surface reconstruction similar to the one formed by the surface alloys on Ag(111) due to the herringbone reconstruction. Tungsten could be a nice substrate for such an experiment due to its high atomic number, and the lighter weight elements Ca and Sr could be suitable alloy atoms. It can be speculated that if the lighter alloy atoms show a sizable outward relaxation the size of the spin splitting could be even further enhanced due to the larger number of heavy atoms. Moreover, it may be possible that the inverted ordering of the atoms with respect to the atomic number Z leads to a reversed chirality of the spin structure.

The results presented in this thesis can even be translated to the surface states of topological insulators. In Bi_2Te_3 for example, the surface states show similarities to quantum well states in the sense that the wave function is distributed throughout each quintuple layer and decays quintuple layer by quintuple layer. [132] In $PbBi_4Te_7$ the absolute value of the surface state wave function is even larger further away from the surface. [133] The properties indicate that it will be possible to shift the wave function in the direction perpendicular to the surface with suitable alterations to the topmost unit cell. Such changes can of course not influence the topology of the surface states, but it can be assumed that it is possible to modify the dispersion and the direction of the spin polarization vector.

Unfortunately the use of external magnetic fields is not possible in (S)ARPES experiments because of the influence on the electron trajectories. However, the influence of magnetic fields on the surface alloys on Ag(111) or Rashba systems in general would be of great interest, because severe modifications of both the band and the spin structure can be expected. The presence of magnetic fields could lift the forced degeneracy at e.g. the $\bar{\Gamma}$ point. Results obtained for topologically trivial Rashba systems could in principle be translated to topologically non-trivial systems. Possible experiments could involve magnetic alloy atoms on non-magnetic substrates or magnetic impurities on (non-magnetic) Rashba systems. During this thesis it was tried to make a first step towards this direction by studying magnetic Co impurities on the surface alloys on Ag(111). However, due to the limited amount of time, this project was terminated without any conclusive results. It seems that Co forms clusters of atoms on the surface alloys on Ag(111) rather than single impurities, which is not desirable for first experiments. In combination with the structural information obtained by STM similar projects could be very promising.

Vicinal surfaces allow for the confinement of the surface state wave function in the direction perpendicular to the steps. [134, 135] In that respect it might be possible to alloy the surface of a vicinal Ag crystal and to study the effects of the confinement inhibition on the spin structure. The large spin splitting observed in the surface alloys on Ag(111) would then allow for a precise determination of these effects.

In Sb/Ag(111), the spin-state interference is assigned to a region in $\boldsymbol{k}$ space where quasiparticles with opposite spin polarization overlap due to the momentum broadening caused by electron-defect scattering. However, several questions remain unanswered, among them: (*i*) What does exactly determine the phase relation? (*ii*) Is this type of spin interference common to a large variety of systems with small spin splittings, including magnetic systems? (*iii*) Does it also occur when electron and hole quasiparticles are formed by other types of excitations? It is speculated that the phase relation between electrons with opposite spinors is determined by the symmetry of the initial and final states as well as by the experimental geometry. Therefore a SARPES measurements performed in a different setup could clarify the influence of the experimental geometry. Experiments on different types of systems with small spin splittings on the other hand could reveal the influence of the symmetry of the initial and final states.

A Density of states of a Rashba gas

The density of states $\nu(E)$ for a 2D Rashba gas can be defined by the following integral over the two branches $E_\pm(\boldsymbol{k}_{||})$ of the dispersion relation at E,

$$\begin{aligned} \nu(E) &:= \int \frac{d^2\boldsymbol{k}_{||}}{(2\pi)^2} \sum_{\pm} \delta\big(E_\pm(\boldsymbol{k}_{||}) - E\big) \\ &= \frac{1}{2\pi} \int\limits_0^\infty dk\, k \sum_{\pm} \delta\big(E_\pm(k) - E\big) \\ &= \frac{1}{2\pi} \int\limits_0^\infty dk\, k \sum_{r=i,o} J^{(r)}\, \delta\left(k - k^{(r)}\right) \end{aligned} \tag{41}$$

where $k = |\boldsymbol{k}_{||}|$ is the radial part of the momentum vector. In Eqs. 41 the rotation symmetry of the dispersion relation has been used. There are here two positive roots $k^{(i)}$ and $k^{(o)}$ of

$$\begin{aligned} E_\pm(k) = E \iff -\frac{\hbar^2 k^2}{2m^*} \pm \alpha_R k + E_{\bar{\Gamma}} - E \ &= 0 \\ \iff k^{(i/o)} = &\begin{cases} \frac{m^*}{\hbar^2}\left(\Delta_{R,\bar{\Gamma}} \mp \alpha_R\right), \text{ if } E_{\bar{\Gamma}} - E \ > 0, \\ \\ \frac{m^*}{\hbar^2}\left(\alpha_R \mp \Delta_{R,\bar{\Gamma}}\right), \text{ if } E_{\bar{\Gamma}} - E \ < 0, \end{cases} \end{aligned} \tag{42a}$$

where

$$\Delta_{R,\bar{\Gamma}} := \left| \sqrt{\alpha_R^2 + \frac{2\hbar^2}{m^*}\left(E_{\bar{\Gamma}} - E\ \right)} \right|. \tag{42b}$$

The root $k^{(i)}$ $\left(k^{(o)}\right)$ belongs to the Fermi surface from the lower (upper) dispersive branch $E_-(\boldsymbol{k}_{||})$ $\left(E_+(\boldsymbol{k}_{||})\right)$ with the inner (outer) radius when $\Delta_{R,\bar{\Gamma}}^2 \geq \alpha_R^2$, while the positive root $k^{(i)}$ $\left(k^{(o)}\right)$ belongs to the Fermi surfaces from the upper dispersive branch $E_+(\boldsymbol{k}_{||})$ with the inner (outer) radius when $\Delta_{R,\bar{\Gamma}}^2 < \alpha_R^2$. Furthermore, $J^{(r)}$ in Eq. 41 is defined as

$$J^{(i)} := \begin{cases} \left|\left(\frac{dE_-}{dk}\right)\left(k^{(i)}\right)\right|^{-1}, \text{ if } E_{\bar{\Gamma}} - E \ > 0, \\ \\ \left|\left(\frac{dE_+}{dk}\right)\left(k^{(i)}\right)\right|^{-1}, \text{ if } E_{\bar{\Gamma}} - E \ < 0, \end{cases} \tag{43a}$$

and

$$J^{(o)} := \begin{cases} \left|\left(\frac{dE_-}{dk}\right)\left(k^{(o)}\right)\right|^{-1}, \text{ if } E_{\bar{\Gamma}} - E \ > 0, \\ \\ \left|\left(\frac{dE_+}{dk}\right)\left(k^{(o)}\right)\right|^{-1}, \text{ if } E_{\bar{\Gamma}} - E \ < 0. \end{cases} \tag{43b}$$

The density of states can correspondingly be decomposed into two contributions

$$\nu(E) = \sum_{r=i,o} \nu^{(r)}(E) \tag{44a}$$

where

$$\nu^{(r)}(E) := \frac{1}{2\pi} k^{(r)}\, J^{(r)}. \tag{44b}$$

To proceed, it is useful to express the inner and outer momenta solely in terms of the energy scales E_0, $E_{\bar\Gamma}$ and $E\ $. Using

$$\alpha_r^2 = \frac{2\hbar^2}{m^*}\left(E_0 - E_{\bar\Gamma}\right), \qquad k_r = \frac{\sqrt{2m^*}}{\hbar}\sqrt{E_0 - E_{\bar\Gamma}}, \tag{45a}$$

the discriminant $\Delta_{R,\bar\Gamma}$ can be rewritten as

$$\Delta_{R,\bar\Gamma} = \left|\sqrt{\frac{2\hbar^2}{m^*}\left(E_0 - E\ \right)}\right|. \tag{45b}$$

Whenever $E_0 - E\ \geq 0$, then

$$\begin{aligned} k^{(i)} &= \frac{\sqrt{2m^*}}{\hbar}\left|\sqrt{E_0 - E\ } - \sqrt{E_0 - E_{\bar\Gamma}}\right|, \\ k^{(o)} &= \frac{\sqrt{2m^*}}{\hbar}\left|\sqrt{E_0 - E\ } + \sqrt{E_0 - E_{\bar\Gamma}}\right|. \end{aligned} \tag{46}$$

With the help of

$$\frac{dE_\pm}{dk} = -\frac{\hbar^2}{m^*}k \pm \alpha_R = -\frac{\hbar^2}{m^*}\left(k \mp k_r\right) \tag{47}$$

a direct calculation shows that

$$J^{(i)} = J^{(0)} = \left(\hbar\sqrt{\frac{2}{m^*}}\sqrt{E_0 - E\ }\right)^{-1}. \tag{48}$$

Inserting Eqs. (48) and (46) into the partial density of states (44), we get

$$\begin{aligned} \nu^{(i)}(E\ ) &= \frac{m^*}{2\pi\hbar}\left|1 - \frac{\sqrt{E_0 - E_{\bar\Gamma}}}{\sqrt{E_0 - E\ }}\right|, \\ \nu^{(o)}(E\ ) &= \frac{m^*}{2\pi\hbar}\left|1 + \frac{\sqrt{E_0 - E_{\bar\Gamma}}}{\sqrt{E_0 - E\ }}\right|, \end{aligned} \tag{49}$$

for the inner and outer bands, respectively. The sum $\nu^{(i)}(E\ ) + \nu^{(o)}(E\ )$ reduces to the constant DOS $2\nu_{2D} = |m^*|/(\pi\hbar^2)$ of a spin degenerate 2D electron (hole) gas with parabolic dispersion when $E_{\bar\Gamma} > E\ $, has a singular derivative when $E\ = E_{\bar\Gamma}$, while it displays the 1D Van Hove-type singularity $\nu(E\ ) \sim (E_0 - E\ )^{-1/2}$ in the limit $E\ \to E_0$. Integration of the DOS from $E_{\bar\Gamma}$ to E_0 yields

$$\int_{E_{\bar\Gamma}}^{E_0} dE\ \nu(E) = \frac{|m^*|}{\pi\hbar^2}\sqrt{E_0 - E_{\bar\Gamma}}\int_{E_{\bar\Gamma}}^{E_0} dE(E_0 - E)^{-1/2} = 2\frac{|m^*|}{\pi\hbar^2}(E_0 - E_{\bar\Gamma}) = 4\nu_{2D}(E_0 - E_{\bar\Gamma}). \tag{50}$$

References

[1] S. A. Wolf, D. D. Awschalom, R. A. Buhrman, J. M. Daughton, S. von Molnar, M. L. Roukes, A. Y. Chtchelkanova, and D. M. Treger, *Spintronics: A Spin-Based Electronics Vision for the Future*, Science **294**, 1488 (2001).

[2] I. Žutić, J. Fabian, and S. Das Sarma, *Spintronics: Fundamentals and applications*, Rev. Mod. Phys. **76**, 323 (2004).

[3] Y. Bychkov and E. Rashba, *Oscillatory effects and the magnetic susceptibility of carriers in inversion layers*, JETP Lett. **39**, 78 (1984).

[4] I. Tamm, *A possible kind of electron binding on crystal surfaces*, Physik. Zeits. der Sowjetunion **1**, 733 (1932).

[5] W. Shockley, *On the Surface States Associated with a Periodic Potential*, Phys. Rev. **56**, 317 (1939).

[6] S. LaShell, B. A. McDougall, and E. Jensen, *Spin Splitting of an Au(111) Surface State Band Observed with Angle Resolved Photoelectron Spectroscopy*, Phys. Rev. Lett. **77**, 3419 (1996).

[7] F. Reinert, G. Nicolay, S. Schmidt, D. Ehm, and S. Hüfner, *Direct measurements of the L-gap surface states on the (111) face of noble metals by photoelectron spectroscopy*, Phys. Rev. B **63**, 115415 (2001).

[8] M. Hochstrasser, J. G. Tobin, E. Rotenberg, and S. D. Kevan, *Spin-Resolved Photoemission of Surface States of* $W(110)-(1\times 1)H$, Phys. Rev. Lett. **89**, 216802 (2002).

[9] M. Hoesch, M. Muntwiler, V. N. Petrov, M. Hengsberger, L. Patthey, M. Shi, M. Falub, T. Greber, and J. Osterwalder, *Spin structure of the Shockley surface state on* $Au(111)$, Phys. Rev. B **69**, 241401 (2004).

[10] S. Agergaard, C. Sondergaard, H. Li, M. B. Nielsen, S. V. Hoffmann, Z. Li, and P. Hofmann, *The effect of reduced dimensionality on a semimetal: the electronic structure of the Bi(110) surface*, New Journal of Physics **3**, 15 (2001).

[11] C. R. Ast and H. Höchst, *Fermi Surface of Bi(111) Measured by Photoemission Spectroscopy*, Phys. Rev. Lett. **87**, 177602 (2001).

[12] Y. M. Koroteev, G. Bihlmayer, J. E. Gayone, E. V. Chulkov, S. Blügel, P. M. Echenique, and P. Hofmann, *Strong Spin-Orbit Splitting on Bi Surfaces*, Phys. Rev. Lett. **93**, 046403 (2004).

[13] P. Hofmann, J. E. Gayone, G. Bihlmayer, Y. M. Koroteev, and E. V. Chulkov, *Electronic structure and Fermi surface of Bi(100)*, Phys. Rev. B **71**, 195413 (2005).

[14] P. Hofmann, *The surfaces of bismuth: Structural and electronic properties*, Progress in Surface Science **81**, 191 (2006).

[15] J. W. Wells, J. H. Dil, F. Meier, J. Lobo-Checa, V. N. Petrov, J. Osterwalder, M. M. Ugeda, I. Fernandez-Torrente, J. I. Pascual, E. D. L. Rienks, M. F. Jensen, and P. Hofmann, *Nondegenerate Metallic States on Bi(114): A One-Dimensional Topological Metal*, Physical Review Letters **102**, 096802 (2009).

[16] C. L. Kane and E. J. Mele, *Z2 Topological Order and the Quantum Spin Hall Effect*, Phys. Rev. Lett. **95**, 146802 (2005).

[17] L. Fu and C. L. Kane, *Topological insulators with inversion symmetry*, Physical Review B **76**, 045302 (2007).

[18] S.-C. Zhang, *Topological states of quantum matter*, Physics **1**, 6 (2008).

[19] H. Zhang, C.-X. Liu, X.-L. Qi, X. Dai, Z. Fang, and S.-C. Zhang, *Topological insulators in Bi2Se3, Bi2Te3 and Sb2Te3 with a single Dirac cone on the surface*, Nature Physics **5**, 438 (2009).

[20] D. Hsieh et al., *A tunable topological insulator in the spin helical Dirac transport regime*, Nature **460**, 1101 (2009).

[21] D. Hsieh, Y. Xia, L. Wray, D. Qian, A. Pal, J. H. Dil, J. Osterwalder, F. Meier, G. Bihlmayer, C. L. Kane, Y. S. Hor, R. J. Cava, and M. Z. Hasan, *Observation of Unconventional Quantum Spin Textures in Topological Insulators*, Science **323**, 919 (2009).

[22] E. Frantzeskakis, S. Pons, H. Mirhosseini, J. Henk, C. R. Ast, and M. Grioni, *Tunable Spin Gaps in a Quantum-Confined Geometry*, Phys. Rev. Lett. **101**, 196805 (2008).

[23] T. Hirahara, T. Komorida, A. Sato, G. Bihlmayer, E. V. Chulkov, K. He, I. Matsuda, and S. Hasegawa, *Manipulating quantum-well states by surface alloying: Pb on ultrathin Ag films*, Phys. Rev. B **78**, 035408 (2008).

[24] H. Bentmann, F. Forster, G. Bihlmayer, E. V. Chulkov, L. Moreschini, M. Grioni, and F. Reinert, *Origin and manipulation of the Rashba splitting in surface alloys*, Europhys. Lett. **87**, 37003 (2009).

[25] E. Frantzeskakis, S. Pons, and M. Grioni, *Band structure scenario for the giant spin-orbit splitting observed at the Bi/Si(111) interface*, Phys. Rev. B **82**, 085440 (2010).

[26] K. Yaji, Y. Ohtsubo, S. Hatta, H. Okuyama, K. Miyamoto, T. Okuda, A. Kimura, H. Namatame, M. Taniguchi, and T. Aruga, *Large Rashba spin splitting of a metallic surface-state band on a semiconductor surface*, Nat Commun **1**, 1 (2010).

[27] S. Hüfner, *Photoelectron Spectroscopy: Principles and Applications, 3rd edn*, Springer, Berlin Heidelberg New York, 2003.

[28] A. Einstein, Annalen der Physik **17**, 132 (1905).

[29] R. Matzdorf, *Investigation of line shapes and line intensities by high-resolution UV-photoemission spectroscopy – Some case studies on noble-metal surfaces*, Surface Science Reports **30**, 153 (1998).

[30] E. O. Kane, *Implications of Crystal Momentum Conservation in Photoelectric Emission for Band-Structure Measurements*, Phys. Rev. Lett. **12**, 97 (1964).

[31] L. D. Landau, *Theory of Fermi-liquids*, JETP **3**, 920 (1957).

[32] E. V. Chulkov, A. G. Borisov, J. P. Gauyacq, D. Sanchez-Portal, V. M. Silkin, V. P. Zhukov, and P. M. Echenique, *Electronic Excitations in Metals and at Metal Surfaces*, Chemical Reviews **106**, 4160 (2006).

[33] P. Hofmann, I. Y. Sklyadneva, E. D. L. Rienks, and E. V. Chulkov, *Electron–phonon coupling at surfaces and interfaces*, New Journal of Physics **11**, 125005 (2009).

[34] C. R. Ast, G. Wittich, P. Wahl, R. Vogelgesang, D. Pacilé, M. C. Falub, L. Moreschini, M. Papagno, M. Grioni, and K. Kern, *Local detection of spin-orbit splitting by scanning tunneling spectroscopy*, Physical Review B (Condensed Matter and Materials Physics) **75**, 201401 (2007).

[35] J. Kliewer, R. Berndt, E. V. Chulkov, V. M. Silkin, P. M. Echenique, and S. Crampin, *Dimensionality Effects in the Lifetime of Surface States*, Science **288**, 1399 (2000).

[36] M. F. Jensen, T. K. Kim, S. Bengió, I. Y. Sklyadneva, A. Leonardo, S. V. Eremeev, E. V. Chulkov, and P. Hofmann, *Thermally induced defects and the lifetime of electronic surface states*, Phys. Rev. B **75**, 153404 (2007).

[37] E. Cappelluti, C. Grimaldi, and F. Marsiglio, *Electron-phonon effects on spin-orbit split bands of two-dimensional systems*, Physical Review B (Condensed Matter and Materials Physics) **76**, 085334 (2007).

[38] I. A. Nechaev, M. F. Jensen, E. D. L. Rienks, V. M. Silkin, P. M. Echenique, E. V. Chulkov, and P. Hofmann, *Hole dynamics in a two-dimensional spin-orbit coupled electron system: Theoretical and experimental study of the Au(111) surface state*, Physical Review B **80**, 113402 (2009).

[39] J. I. Pascual, G. Bihlmayer, Y. M. Koroteev, H.-P. Rust, G. Ceballos, M. Hansmann, K. Horn, E. V. Chulkov, S. Blügel, P. M. Echenique, and P. Hofmann, *Role of Spin in Quasiparticle Interference*, Phys. Rev. Lett. **93**, 196802 (2004).

[40] P. Roushan, J. Seo, C. V. Parker, Y. S. Hor, D. Hsieh, D. Qian, A. Richardella, M. Z. Hasan, R. J. Cava, and A. Yazdani, *Topological surface states protected from backscattering by chiral spin texture*, Nature **460**, 1106 (2009).

[41] J. Seo, P. Roushan, H. Beidenkopf, Y. S. Hor, R. J. Cava, and A. Yazdani, *Transmission of topological surface states through surface barriers*, Nature **466**, 343 (2010).

[42] N. F. Mott, *The Scattering of Fast Electrons by Atomic Nuclei*, Proceedings of the Royal Society of London. Series A **124**, 425 (1929).

[43] W. Pauli, *Handbuch der Physik*, Springer Berlin **1** (1958).

[44] H. Dehmelt, *Experiments on the Structure of an Individual Elementary Particle*, Science **247**, 539 (1990).

[45] H. Batelaan, T. J. Gay, and J. J. Schwendiman, *Stern-Gerlach Effect for Electron Beams*, Phys. Rev. Lett. **79**, 4517 (1997).

[46] B. M. Garraway and S. Stenholm, *Observing the spin of a free electron*, Phys. Rev. A **60**, 63 (1999).

[47] J. Kessler, *Polarized Electrons, 2nd edn.*, Springer, Berlin Heidelberg, 1985.

[48] T. J. Gay and F. B. Dunning, *Mott electron polarimetry*, Review of Scientific Instruments **63**, 1635 (1992).

[49] F. Dunning, *Mott electron polarimetry*, Nuclear Instruments and Methods in Physics Research Section A: Accelerators, Spectrometers, Detectors and Associated Equipment **347**, 152 (1994).

[50] J. Kirschner and R. Feder, *Spin Polarization in Double Diffraction of Low-Energy Electrons from W(001): Experiment and Theory*, Phys. Rev. Lett. **42**, 1008 (1979).

[51] R. T. D. Tillmann and E. Kisker, *Very-low-energy spin-polarized electron diffraction from Fe(001)*, Zeitschrift für Physik B Condensed Matter **77**, 1 (1989).

[52] T. Okuda, Y. Takeichi, Y. Maeda, A. Harasawa, I. Matsuda, T. Kinoshita, and A. Kakizaki, *A new spin-polarized photoemission spectrometer with very high efficiency and energy resolution*, Review of Scientific Instruments **79**, 123117 (2008).

[53] C. Jozwiak, J. Graf, G. Lebedev, N. Andresen, A. K. Schmid, A. V. Fedorov, F. E. Gabaly, W. Wan, A. Lanzara, and Z. Hussain, *A high-efficiency spin-resolved photoemission spectrometer combining time-of-flight spectroscopy with exchange-scattering polarimetry*, Review of Scientific Instruments **81**, 053904 (2010).

[54] N. Sherman, *Coulomb Scattering of Relativistic Electrons by Point Nuclei*, Phys. Rev. **103**, 1601 (1956).

[55] V. N. Petrov, V. V. Grebenshikov, B. D. Grachev, and A. S. Kamochkin, *New compact classical 40 kV Mott polarimeter*, Review of Scientific Instruments **74**, 1278 (2003).

[56] V. N. Petrov, V. V. Grebenshikov, A. N. Andronov, P. G. Gabdullin, and A. V. Maslevtcov, *Ultrafast compact classical Mott polarimeter*, Review of Scientific Instruments **78**, 025102 (2007).

[57] L. G. Gray, M. W. Hart, F. B. Dunning, and G. K. Walters, *Simple, compact, medium-energy Mott polarization analyzer*, Review of Scientific Instruments **55**, 88 (1984).

[58] S. Souma, A. Takayama, K. Sugawara, T. Sato, and T. Takahashi, *Ultrahigh-resolution spin-resolved photoemission spectrometer with a mini Mott detector*, Review of Scientific Instruments **81**, 095101 (2010).

[59] M. Hoesch, T. Greber, V. N. Petrov, M. Muntwiler, M. Hengsberger, W. Auwaerter, and J. Osterwalder, *Spin-polarized Fermi surface mapping*, Journal of Electron Spectroscopy and Related Phenomena **124**, 263 (2002).

[60] T. Greber, O. Raetzo, T. J. Kreutz, P. Schwaller, W. Deichmann, E. Wetli, and J. Osterwalder, *A photoelectron spectrometer for k-space mapping above the Fermi level*, Review of Scientific Instruments **68**, 4549 (1997).

[61] J. Osterwalder, *Spin-Polarized Photoemission*, In: Magnetism: A Synchrotron Radiation Approach, Lecture Notes in Physics **697**, 95 (2006).

[62] A. Kimura, E. E. Krasovskii, R. Nishimura, K. Miyamoto, T. Kadono, K. Kanomaru, E. V. Chulkov, G. Bihlmayer, K. Shimada, H. Namatame, and M. Taniguchi, *Strong Rashba-Type Spin Polarization of the Photocurrent from Bulk Continuum States: Experiment and Theory for Bi(111)*, Phys. Rev. Lett. **105**, 076804 (2010).

[63] H. P. Oepen, K. Hünlich, and J. Kirschner, *Spin-dependent photoemission intensities from solids*, Phys. Rev. Lett. **56**, 496 (1986).

[64] H. Siegmann, *Recent results of crossfertilization between electron spectroscopy and magnetism*, Journal of Electron Spectroscopy and Related Phenomena **68**, 505 (1994).

[65] D. Oberli, R. Burgermeister, S. Riesen, W. Weber, and H. C. Siegmann, *Total Scattering Cross Section and Spin Motion of Low Energy Electrons Passing through a Ferromagnet*, Phys. Rev. Lett. **81**, 4228 (1998).

[66] M. Getzlaff, J. Bansmann, J. Braun, and G. Schnhense, *Spin resolved photoemission study of Co(0001) films*, Journal of Magnetism and Magnetic Materials **161**, 70 (1996).

[67] U. Fano, *Spin Orientation of Photoelectrons Ejected by Circularly Polarized Light*, Phys. Rev. **178**, 131 (1969).

[68] U. Heinzmann, J. Kessler, and B. Ohnemus, *Polarized Electrons by Photoemission from Solid Alkalis*, Phys. Rev. Lett. **27**, 1696 (1971).

[69] D. T. Pierce and F. Meier, *Photoemission of spin-polarized electrons from GaAs*, Phys. Rev. B **13**, 5484 (1976).

[70] B. Schmiedeskamp, B. Kessler, N. Mueller, G. Schoenhense, and U. Heinzmann, *Spin-resolved photoemission from Pd(111)*, Solid State Communications **65**, 665 (1988).

[71] G. S. U. Heinzmann, *Spin-Resolved Photoemission from Nonmag- netic Metals and Adsorbates*, In: Polarized Electrons in Surface Physics **697**, 467 (1985).

[72] D. T. Pierce, R. J. Celotta, G.-C. Wang, W. N. Unertl, A. Galejs, C. E. Kuyatt, and S. R. Mielczarek, *The GaAs spin polarized electron source*, Review of Scientific Instruments **51**, 478 (1980).

[73] U. Heinzmann, J. Kessler, and J. Lorenz, *Wavelength Dependence of the Fano Effect*, Phys. Rev. Lett. **25**, 1325 (1970).

[74] E. Tamura, W. Piepke, and R. Feder, *New spin-polarization effect in photoemission from nonmagnetic surfaces*, Phys. Rev. Lett. **59**, 934 (1987).

[75] B. Schmiedeskamp, B. Vogt, and U. Heinzmann, *Experimental verification of a new spin-polarization effect in photoemission: Polarized photoelectrons from Pt(111) with linearly polarized radiation in normal incidence and normal emission*, Phys. Rev. Lett. **60**, 651 (1988).

[76] N. Irmer, R. David, B. Schmiedeskamp, and U. Heinzmann, *Experimental verification of a spin effect in photoemission: Polarized electrons due to phase-shift differences in the normal emission from Pt(100) by unpolarized radiation*, Phys. Rev. B **45**, 3849 (1992).

[77] E. Tamura and R. Feder, *Spin Polarization in Normal Photoemission by Linearly Polarized Light from Nonmagnetic (001) Surfaces*, EPL (Europhysics Letters) **16**, 695 (1991).

[78] J. Henk and R. Feder, *Spin Polarization in Normal Photoemission by Linearly Polarized Light from Non-Magnetic (110) Surfaces*, EPL (Europhysics Letters) **28**, 609 (1994).

[79] N. Irmer, F. Frentzen, S. W. Yu, B. Schmiedeskamp, and U. Heinzmann, *A new effect in spin-resolved photoemission from Pt(110) in normal emission by linearly polarized VUV-radiation*, Journal of Electron Spectroscopy and Related Phenomena **78**, 321 (1996).

[80] J. Henk, M. Hoesch, J. Osterwalder, A. Ernst, and P. Bruno, *Spin-orbit coupling in the L-gap surface states of Au(111): spin-resolved photoemission experiments and first-principles calculations*, Journal of Physics: Condensed Matter **16**, 7581 (2004).

[81] N. Müller, T. Khalil, M. Pohl, T. Uphues, M. Polcik, O. Rader, F. Heigl, K. Starke, S. Fritzsche, N. M. Kabachnik, and U. Heinzmann, *Interference of spin states in resonant photoemission induced by circularly polarized light from magnetized Gd*, Physical Review B **74**, 161401 (2006).

[82] M. Hoesch, *Spin-resolved Fermi surface mapping*, PhD thesis, Universität Zürich, 2002.

[83] J. H. Dil, F. Meier, J. Lobo-Checa, L. Patthey, G. Bihlmayer, and J. Osterwalder, *Rashba-Type Spin-Orbit Splitting of Quantum Well States in Ultrathin Pb Films*, Physical Review Letters **101**, 266802 (2008).

[84] A. Gellrich and J. Kessler, *Precision measurement of the Sherman asymmetry function for electron scattering from gold*, Phys. Rev. A **43**, 204 (1991).

[85] V. N. Petrov, M. S. Galaktionov, and A. S. Kamochkin, *Comparative tests of conventional and retarding-potential Mott polarimeters*, Review of Scientific Instruments **72**, 3728 (2001).

[86] B. H. Armstrong, *Spectrum line profiles: The Voigt unction*, Journal of Quantitative Spectroscopy and Radiative Transfer **7**, 61 (1967).

[87] G. Bihlmayer, S. Blügel, and E. V. Chulkov, *Enhanced Rashba spin-orbit splitting in Bi/Ag(111) and Pb/Ag(111) surface alloys from first principles*, Physical Review B (Condensed Matter and Materials Physics) **75**, 195414 (2007).

[88] C. M. Cacho, S. Vlaic, M. Malvestuto, B. Ressel, E. A. Seddon, and F. Parmigiani, *Absolute spin calibration of an electron spin polarimeter by spin-resolved photoemission from the Au(111) surface states*, Review of Scientific Instruments **80**, 043904 (2009).

[89] R. Winkler, *Spin-Orbit Coupling Effects in Two-Dimensional Electron and Hole Systems*, Springer Tracts in Modern Physics, Springer, Berlin, 2003.

[90] J. Nitta, T. Akazaki, H. Takayanagi, and T. Enoki, *Gate Control of Spin-Orbit Interaction in an Inverted* $In0.53Ga0.47As/In0.52Al0.48As$ *Heterostructure*, Phys. Rev. Lett. **78**, 1335 (1997).

[91] Y. A. Bychkov and E. I. Rashba, *Oscillatory effects and the magnetic susceptibility of carriers in inversion layers*, Journal of Physics C: Solid State Physics **17**, 6039 (1984).

[92] G. Dresselhaus, *Spin-Orbit Coupling Effects in Zinc Blende Structures*, Phys. Rev. **100**, 580 (1955).

[93] D. S. Saraga and D. Loss, *Fermi liquid parameters in two dimensions with spin-orbit interaction*, Phys. Rev. B **72**, 195319 (2005).

[94] E. Cappelluti, C. Grimaldi, and F. Marsiglio, *Topological Change of the Fermi Surface in Low-Density Rashba Gases: Application to Superconductivity*, Physical Review Letters **98**, 167002 (2007).

[95] J. Lobo-Checa, F. Meier, J. H. Dil, T. Okuda, M. Corso, V. N. Petrov, M. Hengsberger, L. Patthey, and J. Osterwalder, *Robust Spin Polarization and Spin Textures on Stepped Au(111) Surfaces*, Phys. Rev. Lett. **104**, 187602 (2010).

[96] S. Datta and B. Das, *Electronic analog of the electro-optic modulator*, Applied Physics Letters **56**, 665 (1990).

[97] B. Das, D. C. Miller, S. Datta, R. Reifenberger, W. P. Hong, P. K. Bhattacharya, J. Singh, and M. Jaffe, *Evidence for spin splitting in* $In_xGa_{1-x}As/In_{0.52}Al_{0.48}As$ *heterostructures as* $B \to 0$, Phys. Rev. B **39**, 1411 (1989).

[98] M. Studer, G. Salis, K. Ensslin, D. C. Driscoll, and A. C. Gossard, *Gate-Controlled Spin-Orbit Interaction in a Parabolic GaAs/AlGaAs Quantum Well*, Phys. Rev. Lett. **103**, 027201 (2009).

[99] J. P. Eisenstein, H. L. Störmer, V. Narayanamurti, A. C. Gossard, and W. Wiegmann, *Effect of Inversion Symmetry on the Band Structure of Semiconductor Heterostructures*, Phys. Rev. Lett. **53**, 2579 (1984).

[100] L. Petersen and P. Hedegrd, *A simple tight-binding model of spin-orbit splitting of sp-derived surface states*, Surface Science **459**, 49 (2000).

[101] G. Bihlmayer, Y. Koroteev, P. Echenique, E. Chulkov, and S. Bluegel, *The Rashba-effect at metallic surfaces*, Surface Science **600**, 3888 (2006), Berlin, Germany: 4-9 September 2005, Proceedings of the 23th European Conference on Surface Science.

[102] C. R. Ast, J. Henk, A. Ernst, L. Moreschini, M. C. Falub, D. Pacilé, P. Bruno, K. Kern, and M. Grioni, *Giant Spin Splitting through Surface Alloying*, Physical Review Letters **98**, 186807 (2007).

[103] D. Popović, F. Reinert, S. Hüfner, V. G. Grigoryan, M. Springborg, H. Cercellier, Y. Fagot-Revurat, B. Kierren, and D. Malterre, *High-resolution photoemission on* $Ag/Au(111)$ *: Spin-orbit splitting and electronic localization of the surface state*, Phys. Rev. B **72**, 045419 (2005).

[104] H. Cercellier, C. Didiot, Y. Fagot-Revurat, B. Kierren, L. Moreau, D. Malterre, and F. Reinert, *Interplay between structural, chemical, and spectroscopic properties of* $Ag/Au(111)$ *epitaxial ultrathin films: A way to tune the Rashba coupling*, Phys. Rev. B **73**, 195413 (2006).

[105] J. H. Dil, *Spin and angle resolved photoemission on non-magnetic low-dimensional systems*, Journal of Physics: Condensed Matter **21**, 403001 (22pp) (2009).

[106] G. Nicolay, F. Reinert, S. Hüfner, and P. Blaha, *Spin-orbit splitting of the L-gap surface state on Au(111) and Ag(111)*, Phys. Rev. B **65**, 033407 (2001).

[107] G. Bihlmayer, Y. M. Koroteev, E. V. Chulkov, and S. Blügel, *Surface- and edge-states in ultrathin BiSb films*, New Journal of Physics **12**, 065006 (2010).

[108] J. Premper, M. Trautmann, J. Henk, and P. Bruno, *Spin-orbit splitting in an anisotropic two-dimensional electron gas*, Physical Review B (Condensed Matter and Materials Physics) **76**, 073310 (2007).

[109] C. R. Ast, D. Pacilé, L. Moreschini, M. C. Falub, M. Papagno, K. Kern, M. Grioni, J. Henk, A. Ernst, S. Ostanin, and P. Bruno, *Spin-orbit split two-dimensional electron gas with tunable Rashba and Fermi energy*, Physical Review B (Condensed Matter and Materials Physics) **77**, 081407 (2008).

[110] I. Gierz, B. Stadtmüller, J. Vuorinen, M. Lindroos, F. Meier, J. H. Dil, K. Kern, and C. R. Ast, *Structural influence on the Rashba-type spin splitting in surface alloys*, Phys. Rev. B **81**, 245430 (2010).

[111] L. Fu, C. L. Kane, and E. J. Mele, *Topological Insulators in Three Dimensions*, Physical Review Letters **98**, 106803 (2007).

[112] M. A. V. Hove, *Surface Crystallography with Low-Energy Electron Diffraction*, Proceedings: Mathematical and Physical Sciences **442**, pp. 61 (1993).

[113] J. B. Pendry, *Reliability factors for LEED calculations*, J. Phys. C: Solid St. Phys. **13**, 937 (1980).

[114] D. P. Woodruff and J. Robinson, *Sb-induced surface stacking faults at Ag(111) and Cu(111) surfaces: density-functional theory results*, Journal of Physics: Condensed Matter **12**, 7699 (2000).

[115] P. D. Quinn, D. Brown, D. P. Woodruff, P. Bailey, and T. C. Q. Noakes, *Structural study of the adsorption of Sb on Ag(111) using medium energy ion scattering*, Surface Science **511**, 43 (2002).

[116] J. Dalmas, H. Oughaddou, C. Léandri, J.-M. Gay, G. Le Lay, G. Tréglia, B. Aufray, O. Bunk, and R. L. Johnson, *Ordered surface alloy formation of immiscible metals: The case of Pb deposited on Ag(111)*, Phys. Rev. B **72**, 155424 (2005).

[117] S. de Vries, W. Huisman, P. Goedtkindt, M. Zwanenburg, S. Bennett, I. Robinson, and E. Vlieg, *Surface atomic structure of the reconstructions of Ag(111) and Cu(111)*, Surface Science **414**, 159 (1998).

[118] E. A. Soares, C. Bittencourt, V. B. Nascimento, V. E. de Carvalho, C. M. C. de Castilho, C. F. McConville, A. V. de Carvalho, and D. P. Woodruff, *Structure determination of* $Ag(111)(3\times3)R30^\circ - Sb$ *by low-energy electron diffraction*, Phys. Rev. B **61**, 13983 (2000).

[119] L. Moreschini, A. Bendounan, I. Gierz, C. R. Ast, H. Mirhosseini, H. Höchst, K. Kern, J. Henk, A. Ernst, S. Ostanin, F. Reinert, and M. Grioni, *Assessing the atomic contribution to the Rashba spin-orbit splitting in surface alloys: Sb/Ag(111)*, Physical Review B (Condensed Matter and Materials Physics) **79**, 075424 (2009).

[120] D. Kaminski, P. Poodt, E. Aret, N. Radenovic, and E. Vlieg, *Surface alloys, overlayer and incommensurate structures of Bi on Cu(111)*, Surface Science **575**, 233 (2005).

[121] P. Bailey, T. C. Q. Noakes, and D. P. Woodruff, *A medium energy ion scattering study of the structure of Sb overlayers on Cu(111)*, Surface Science **426**, 358 (1999).

[122] S. V. Hoffmann, C. Sndergaard, C. Schultz, Z. Li, and P. Hofmann, *An undulator-based spherical grating monochromator beamline for angle-resolved photoemission spectroscopy*, Nuclear Instruments and Methods in Physics Research Section A: Accelerators, Spectrometers, Detectors and Associated Equipment **523**, 441 (2004).

[123] D. Pacilé, C. R. Ast, M. Papagno, C. D. Silva, L. Moreschini, M. Falub, A. P. Seitsonen, and M. Grioni, *Electronic structure of an ordered Pb/Ag(111) surface alloy: Theory and experiment*, Physical Review B (Condensed Matter and Materials Physics) **73**, 245429 (2006).

[124] F. Meier, H. Dil, J. Lobo-Checa, L. Patthey, and J. Osterwalder, *Quantitative vectorial spin analysis in angle-resolved photoemission: Bi/Ag(111) and Pb/Ag(111)*, Physical Review B (Condensed Matter and Materials Physics) **77**, 165431 (2008).

[125] F. Meier, V. Petrov, S. Guerrero, C. Mudry, L. Patthey, J. Osterwalder, and J. H. Dil, *Unconventional Fermi surface spin textures in the Bi[sub x]Pb[sub 1 - x]/Ag(111) surface alloy*, Physical Review B (Condensed Matter and Materials Physics) **79**, 241408 (2009).

[126] J. Henk, T. Scheunemann, S. V. Halilov, and R. Feder, *Magnetic dichroism and electron spin polarization in photoemission: analytical results*, Journal of Physics: Condensed Matter **8**, 47 (1996).

[127] F. Baudelet, *X-ray magnetic circular dichroism*, Neutron and X-Ray Spectroscopy, Springer , 013 (2006).

[128] B. Srisongmuang, P. Pairor, and M. Berciu, *Tunneling conductance of a two-dimensional electron gas with Rashba spin-orbit coupling*, Phys. Rev. B **78**, 155317 (2008).

[129] F. Meier, J. H. Dil, and J. Osterwalder, *Measuring spin polarization vectors in angle-resolved photoemission spectroscopy,* New Journal of Physics **11**, 125008 (21pp) (2009).

[130] K. Sakamoto, T. Oda, A. Kimura, K. Miyamoto, M. Tsujikawa, A. Imai, N. Ueno, H. Namatame, M. Taniguchi, P. E. J. Eriksson, and R. I. G. Uhrberg, *Abrupt Rotation of the Rashba Spin to the Direction Perpendicular to the Surface*, Physical Review Letters **102**, 096805 (2009).

[131] F. Kuemmeth and E. I. Rashba, *Giant spin rotation under quasiparticle-photoelectron conversion: Joint effect of sublattice interference and spin-orbit coupling*, Phys. Rev. B **80**, 241409 (2009).

[132] S. Eremeev, Y. Koroteev, and E. Chulkov, *Effect of the atomic composition of the surface on the electron surface states in topological insulators A2(V) B3(VI)*, JETP Letters **91**, 387 (2010-04-01).

[133] S. Eremeev, Y. Koroteev, and E. Chulkov, *On possible deep subsurface states in topological insulators: The PbBi₄Te₇ system*, JETP Letters **92**, 161 (2010-10-01).

[134] A. Mugarza, A. Mascaraque, V. Pérez-Dieste, V. Repain, S. Rousset, F. J. García de Abajo, and J. E. Ortega, *Electron Confinement in Surface States on a Stepped Gold Surface Revealed by Angle-Resolved Photoemission,* Phys. Rev. Lett. **87**, 107601 (2001).

[135] A. Mugarza, A. Mascaraque, V. Repain, S. Rousset, K. N. Altmann, F. J. Himpsel, Y. M. Koroteev, E. V. Chulkov, F. J. García de Abajo, and J. E. Ortega, *Lateral quantum wells at vicinal Au(111) studied with angle-resolved photoemission*, Phys. Rev. B **66**, 245419 (2002).

Curriculum Vitae

Name	Fabian Meier
Birth	27.06.1981 in Zurich (ZH), Switzerland
Nationality	Swiss

Education

2001	Matur, Kantonsschule Hohe Promenade, Zurich, Switzerland
2001 - 2006	Studies of physics, Swiss Federal Institute of Technology Zurich, Switzerland
Nov 2006 - Mar 2007	Diploma thesis in physics ’The Effect of Oxygen Exposure on the Performance of Pentacene Thin-Film Transistors’ at the Institute of Solid State Physics, Swiss Federal Institute of Technology, Zurich, Switzerland
since June 2007	PhD studies of ’Rashba-Type Spin-Orbit Coupling in the Surface Alloys on Ag(111) Probed by Spin- and Angle-Resolved Photoemission Spectroscopy’ at the Physik-Institut, Universizy of Zurich, Switzerland in the group of Prof. J. Osterwalder
...	

Teaching Experience

since June 2007	Teaching assistant, Physik-Institut, University of Zurich basic courses in mechanics, thermodynamics, optics, electricity and magnetism; lab-courses for biology students; solid state physics

Publications

1. W. L. Kalb, **F. Meier**, K. Mattenberger, and B. Batlogg,
   “Defect healing at room temperature in pentacene thin films and improved transistor performance”,
   Phys. Rev. B, **76**, 184112 (2007)

2. **F. Meier**, H. Dil, J. Lobo-Checa, L. Patthey and J. Osterwalder,
   “Quantitative vectorial spin analysis in angle-resolved photoemission: Bi/Ag(111)

and Pb/Ag(111)",
Phys. Rev. B, **77**, 165431 (2008)

3. J. H. Dil, **F. Meier** J. Lobo-Checa, L. Patthey, G. Bihlmayer and J. Osterwalder,
   "Rashba-Type Spin-Orbit Splitting of Quantum Well States in Ultrathin Pb Films",
   Phys. Rev. Lett, **101**, 266802 (2008)

4. D. Hsieh, Y. Xia, L. Wray, D. Qian, A. Pal, J. H. Dil, J. Osterwalder, **F. Meier**, G. Bihlmayer, C. L. Kane, Y. S. Hor, R. J. Cava, and M. Z. Hasan
   "Observation of Unconventional Quantum Spin Textures in Topological Insulators",
   Science, **323**, 5916 (2009)

5. J. W. Wells, J. H. Dil, **F. Meier**, J. Lobo-Checa, V. N. Petrov, J. Osterwalder, M. M. Ugeda, I. Fernandez-Torrente, J. I. Pascual, E. D. L. Rienks, M. F. Jensen, and Ph. Hofmann
   "Nondegenerate Metallic States on Bi(114): A One-Dimensional Topological Metal",
   Phys. Rev. Lett, **102**, 096802 (2009)

6. **F. Meier**, V. Petrov, S. Guerrero, C. Mudry, L. Patthey, J. Osterwalder and J. H. Dil,
   "Unconventional Fermi surface spin textures in the Bi_xPb_{1-x}*/Ag(111) surface alloy"*,
   Phys. Rev. B, **79**, 241408 (2009)

7. J. Lobo-Checa, M. Matena. K. Müller, J. H. Dil, **F. Meier**, L. H. Gade, T. A. Jung and M. Stöhr
   "Electronic confinement imposed by a nanoporous network: Band formation from coupled quantum dots",
   Science, **325**, 300 (2009)

8. D. Hsieh, Y. Xia and D. Qian, L. Wray, J. H. Dil, **F. Meier**, J. Osterwalder, L. Patthey, J. G. Checkelsky, N. P. Ong, A. V. Fedorov, H. Lin, A. Bansil, D. Grauer, Y. S. Hor, R. J. Cava, and M. Z. Hasan
   "A tunable topological insulator in the spin helical Dirac transport regime",
   Nature, **460**, 1101 (2009)

9. D. Hsieh, Y. Xia, D. Qian, L. Wray, **F. Meier**, J. H. Dil, J. Osterwalder, L. Patthey, A. V. Fedorov, H. Lin, A. Bansil, D. Grauer, Y. S. Hor, R. J. Cava, and M. Z. Hasan
   "Observation of Time-Reversal-Protected Single-Dirac-Cone Topological-Insulator

states in Bi_2Te_3 *and* Sb_2Te_3*"*,
Phys. Rev. Lett, **103**, 146401 (2009)

10. **F. Meier**, J. H. Dil, and J. Osterwalder
    "Measuring spin polarization vectors in angle-resolved photoemission spectroscopy",
    New Journal of Physics, **11**, 125008 (2009)

11. J. Lobo-Checa, **F. Meier**, J. H. Dil, T. Okuda, M. Corso, V. Petrov, M. Hengsberger, L. Patthey, and J. Osterwalder
    "Robust Spin Polarization and Spin Textures on Stepped Au(111) Surfaces",
    Phys. Rev. Lett, **104**, 187602 (2010)

12. I. Gierz, B. Stadtmüller, J. Vuorinen, M. Lindroos, **F. Meier**, J. H. Dil, K. Kern, and C. R. Ast
    "Structural influence on the Rashba-type spin splitting in surface alloys",
    Phys. Rev. B, **81**, 245430 (2010)

13. **F. Meier**, V. Petrov, H. Mirhosseini, L. Patthey, J. Henk, J. Osterwalder, and J. H. Dil,
    "Interference of spin states in photoemission from Sb/Ag(111) surface alloys"
    Journal of Physics: Condensed Matter, **23**, 072207 (2011)

14. B. Slomski, **F. Meier**, J. Osterwalder, and J.H. Dil,
    "Controlling the effective mass of quantum well states in Pb/Si(111) by interface engineering"
    Phys. Rev. B, **83**, 035409 (2011)

Languages

Swiss German	Mother tongue
German	Fluent spoken and written
English	Fluent spoken and written
French	Discrete spoken and written

Acknowledgements

It's time to thank all those people who contributed to this work or helped along the way. Considering the large amount of names that I would have to mention, I'm entirely sure that one has to read between the lines to find them all.

First of all I would like to thank Jürg Osterwalder for being a guide in several aspects and for being a perfect boss. I have tried to learn from his way to look at things and tackle problems. A big thank you goes to my direct supervisor Hugo Dil. Without his help and expertise, this work would never have been possible. I'm very grateful for many fruitful discussions with him, be it on physics or even more important topics like skiing or the weather. I however want to apologize for being a continuous source of distraction, in particular in the first two years when we shared the same office. In that respect, I also want to thank my office mates Bartosz Slomski and Dominik Leuenberger, as well as Gabriel Landolt. From the University of Zürich, I further would like to thank Thomas Brugger, Martin Morscher, Martin Klöckner, Thomas Greber and Matthias Hengsberger. I have profited a lot from various discussions and am very grateful for help regarding experiments and administrative issues. For making the life of an experimental physicist easier, I would like to thank our secretaries and the physics workshop at the University of Zürich. For valuable inputs as well as for reading my thesis I want to thank my co-examiner Gustav Bihlmayer.

I would like to thank Moritz Hösch for building the wonderful COPHEE setup. Vladimir Petrov also contributed a lot to the COPHEE setup and I am grateful for his help in both technical and experimental issues. I very much enjoyed working with Jorge Lobo-Checa from Spain. I think that it is of importance to note at this point that Switzerland did beat Spain in the World Cup 2010.

During my thesis, I had the pleasure to carry out various experiments with people from all over the world and I would like to thank them all. From PSI, I very much appreciated the help of Luc Patthey, Milan Radovic, Ming Shi, Christoph Hess, Fritz Dubi and Markus Kropf, and theoretical support from Sebastian Guerrero and Christopher Mudry. From Stuttgart, I would like to thank Isabella Gierz and Christian Ast. Together we had to see once more that physics can sometimes be very difficult. It was a pleasure to meet David Hsieh, Andrew Wray, Matthew Xia and SuYang Xu from Princeton. I am proud of the work we did together in the field of topological insulators. From Aarhus, I would like to thank Philip Hofmann, Emile Rienks and Edward Perkins. I also want to thank Norbert Müller, Ullrich Heinzmann, Hossein Mirhosseini, Jürgen Henk, Johannes Vuorinen and Matti Lindroos.

Besides the people I had the pleasure to meet during my thesis, I owe thanks to the people I call friends since a long time and I appreciate their weird way of support. In particular, I want to thank Gregor Kiowski, Petra Kiowski, Till Bay, Oliver Tubic and Claudio Sedivy for wonderful skiing trips as well as several evenings where we drank potables. I'm glad that I'm still alive. Thanks also go to former fellow students Mark Fischer, Thomas Bisig, Alexander Thomann, Joshua Herbst, Andreas Ahlm and Paul Fichtner. Because apart from friends also sport is important for staying productive, I want to thank my bicycles and the people from YSZ.

Finally I would like to express my gratitude to my parents who always supported me, not only financially, but in any other possible way. Without them, my life would not be the same. I am also very grateful to my grandparents who try to help whenever possible. Last but not least I would like to thank Sibel Özcan for the time we have spent together in the past few years.